ENABLING TECHNOLOGIES FOR IMAGE-GUIDED INTERVENTIONS WITH MINIMALLY INVASIVE SURGICAL ROBOTS

By

Edward Bryn Joseph Pitt

Dissertation

Submitted to the Faculty of the

Graduate School of Vanderbilt University

in partial fulfillment of the requirements

for the degree of

DOCTOR OF PHILOSOPHY

in

Mechanical Engineering

May 31, 2021

Nashville, Tennessee

Approved:

Eric J. Barth, Ph.D.

Robert J. Webster III, Ph.D.

Thomas J. Withrow, Ph.D.

Michael I. Miga, Ph.D.

Nicholas L. Kavoussi, M.D.

TABLE OF CONTENTS

LIST OF TABLES

LIST OF FIGURES

CHAPTER I

Introduction

I.1 Motivation

By minimizing intracorporeal access, minimally invasive surgery sacrifices surgeons' dexterity and situational awareness in the surgical environment in favor of reducing bodily trauma to patients. The desire to marry surgical robotics with surgical image guidance can therefore be seen as a natural response to the limitations imposed by minimally invasive surgery. Compared to the human hand, surgical robots can offer reduced size, increased precision, increased flexibility, increased dexterity, and increased strength. Meanwhile, surgical image guidance provides tools to enable anatomical visualization and spatial context beyond what a surgeon can achieve by direct visualization. This dissertation explores several novel technologies at the intersection of these two fields, with the overall goal of developing and validating novel approaches to image-guided interventions that are specifically enabled by the use of surgical robotics.

This dissertation will address two distinct clinical applications: (i) an envisioned neurosurgical procedure for incisionless, transforamenal hippocampotomy to treat temporal lobe epilepsy; and (ii) robot-assisted partial nephrectomy to treat renal cell carcinomas. While seemingly far apart in the clinical realm, neurological surgery and urologic surgery have historically been among the most technophilic clinical disciplines, making these two applications prime candidates for exploring new technology. More importantly, however, these are areas of large clinical significance.

Epilepsy is a debilitating, potentially fatal, seizure-causing neurological disorder that will affect approximately 1% of people worldwide in their lifetimes [1]. Up to 40% of the patient population is refractory to medical treatment [1, 2], putting them at risk of sudden, unexplained death in epilepsy (SUDEP) at a rate of 1% per patient, per year [3]. While

surgical removal of the hippocampus (commonly the origin of epileptic seizures) successfully and permanently cures epileptic seizures in about 70% of cases [4], 50-90% of eligible patients forgo surgery due to perceived risks associated with highly-invasive brain surgery [4, 5, 6].

Renal cell carcinoma exhibits the highest mortality rate among all genitourinary cancers, being fatal in roughly 33% of patients [7]. Alarmingly, both the incidence and mortality of renal cell carcinoma are on the rise: from 1971 to 2008, the incidence increased by an estimated 400% and mortality increased by an estimated 100% [8]. With early detection, however, surgical intervention can successfully treat the disease with low chance of recurrence. Some cases require radical nephrectomy, in which the entire kidney is removed; however, for patients with clinically localized tumors, the American Urological Association and the European Association of Urology recommend nephron-sparing partial nephrectomy, in which only part of the kidney is removed, as the standard treatment [9, 10]. Compared to radical nephrectomy, partial nephrectomy leads to improved long-term patient outcome by allowing the patient to retain some kidney function and reducing the risk of chronic kidney disease [11, 12]. Robot-assisted partial nephrectomy (RAPN) using the da Vinci Surgical System (Intuitive Surgical, Inc., Sunnyvale, CA, USA) has become the second most commonly performed robotic surgery [13]; however, the procedure is still considered underutilized, likely due to the extreme technical challenges associated with the procedure, especially when performed minimally invasively [14, 15].

By contributing to new technologies that enable image-guided interventions using minimally invasive surgical robots, the work in this dissertation represents a small step toward increasing the accessibility of life-saving medical treatments to both patients and clinicians.

I.2 Background

This section provides the broad, historical context for placing this dissertation relative to the interests and objectives of the related clinical fields. More specific context for placing this work within the scientific literature is provided in the introductory sections of subsequent

chapters.

I.2.1 Surgical Image Guidance

The basic premise of surgical image guidance is to relay to surgeons visual and spatial information that provides enhanced anatomical context of the surgical environment, i.e. the location of surgical tools relative to critical, frequently subsurface, anatomical features. Fundamental to this objective is determining the registration—the best estimated mapping—between a tomographic image space and the physical anatomy of a patient. Image registration can be understood more generally as matching multiple views of the same object or feature in order to transfer information apparent in one view (e.g. the location of a subsurface tumor in a tomographic volume) to the other view (e.g. the endoscopic video during surgery). The mathematical means for determining the registration can vary widely depending on the information used to determine the match, *e.g.* corresponding anatomical features, extrinsic fiducials, extracted surfaces, tomographic image intensities, among others. Reference [16] provides a recent survey of image registration methods used in medical applications.

I.2.2 Image-Guided, Incisionless, Transforamenal Hippocampotomy

The fact that the skull envelops the brain makes access to and visualization of therapeutic targets a fundamental challenge in neurosurgery. Furthermore, neurosurgical targets frequently lie near the brain's center, obscured from external access by large tracts of healthy, potentially eloquent brain tissue. This issue is particularly relevant to epilepsy cases, given that the hippocampi (the epileptogenic foci) are located deep within the medial temporal lobe, as illustrated in Fig. I.1 [17].

A desire to address these general challenges in neurosurgery led directly to the development of stereotactic neurosurgery—the early progenitor of modern surgical image guidance—more than 100 years ago [18, 19]. By rigidly affixing a stereotactic frame, such as the one pictured in Fig. I.2, to a patient's skull, clinicians could accurately direct the tip of a long,

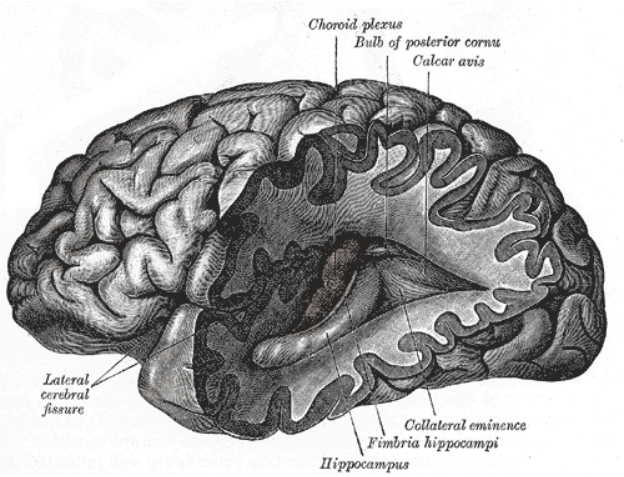

Figure I.1: Classical illustration showing the location of the hippocampus, deep inside the medial temporal lobe [17]. Note that this illustration shows the left hemisphere of brain; the second hippocampus is located symmetrically in the right cerebral hemisphere

thin, straight probe directly to areas in the center of the brain without directly visualizing the surgical target in order to perform a number of procedures, including biopsies and ablations. While early practitioners of stereotactic surgery relied solely on the (dubious) relative consistency of brain anatomy from patient-to-patient in order to locate internal anatomical features, current state-of-the-art navigation systems for stereotactic interventions enable image guidance by registration between surgical tools and preoperative, 3D volumetric images, namely computed tomography (CT) and magnetic resonance (MR) imaging.

In addition to anatomical visualization, MR technology can measure other volumetric data, such as tissue temperature. Advances in MR thermometry within the last decade have enabled new minimally invasive, image-guided, stereotactic treatments for temporal lobe epilepsy that use laser ablation to destroy the hippocampus [21, 22, 23, 24, 25, 26]. Fig. I.3 shows a commercially available example of a neurosurgical laser ablation system [27]. Current data show these laser ablation treatments to be curative in approximately 54% of cases [26]. Though not as effective at curing seizures as traditional, open-skull hippocampectomy, image-guided ablation has gained significant favor due to its minimally invasive nature. As with all stereotactic procedures, however, existing image-guided ablation

Figure I.2: A modern example of a stereotactic frame for neurosurgery: Leksell Stereotactic System (Elekta AB, Stockholm, Sweden) [20]

interventions share two fundamental limitations: (i) they require drilling access holes in the skull; and (ii) they can achieve only linear trajectories, limiting their ability both to reach targeted volumes and to avoid intervening critical structures.

Addressing these limitations motivated the research efforts of former Vanderbilt student David Comber, whose work is the direct predecessor of some work contained in this dissertation [28]. Comber proposed an incisionless, transforamenal hippocampotomy procedure enabled by helically curved, concentric-tube, steerable needles with MR-compatible robotic actuation. Fig. I.4 illustrates the transforamenal approach: using typical stereotactic methods, a straight outer cannula is percutaneously inserted into the center of the brain via the foramen ovale (a small natural orifice in the base of the skull), and then the helical needle (robotically actuated at its proximal end) is steered along the natural curvature of the hippocampus to more effectively deliver ablation therapy to the entire organ volume. Fig. I.5 shows Comber's pneumatically actuated prototype robot, which can be placed alongside a patient in the bore of an MR scanner. In addition to precisely controlling the nonlinear tra-

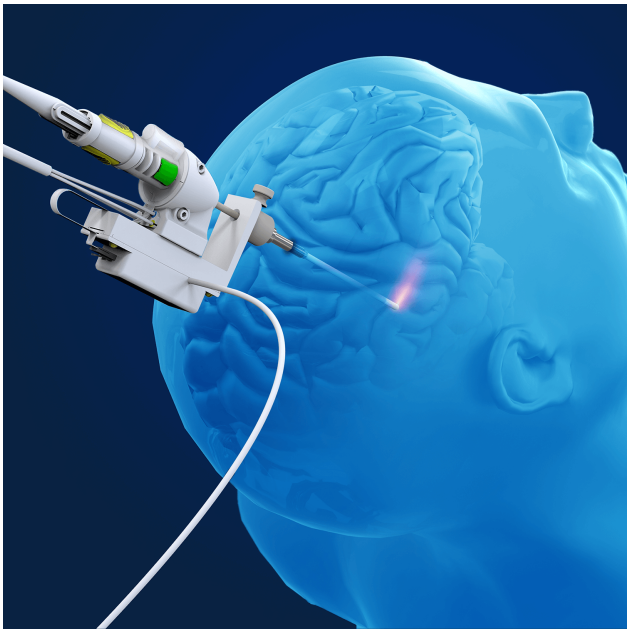

Figure I.3: An example of a stereotactic neurosurgical laser ablation system: the NeuroBlate System (Monteris Medical, Inc., Winnipeg, Manitoba, Canada) [27]

jectory of the helical needle, the MR-compatible actuation unit enables real-time MR-image feedback to correct the needle path in case of any misalignment in the initial stereotactic registration.

I.2.3 Robot-Assisted Urologic Surgery

When the United States Food and Drug Administration (FDA) first cleared the da Vinci Surgical System (Intuitive Surgical, Inc., Sunnyvale, California, USA) for clinical use in 2000, urologic surgery was among the short list of approved clinical disciplines. Figure I.6 shows the most recent generation of the da Vinci Surgical System. With multiple arms and highly dexterous, 7-degree-of-freedom manipulators, the da Vinci System rapidly gained popularity in urologic surgery, especially for prostatectomy, where the small surgical target and constricted access through the pelvis make localization particularly challenging [29]. Compared to traditional laparoscopic procedures, robot-assisted prostatectomy showed significant clinical advantages for patients (reduced blood loss, faster healing times, lower complication rates) and ergonomic improvements for clinicians [30]. Use of the da Vinci system quickly

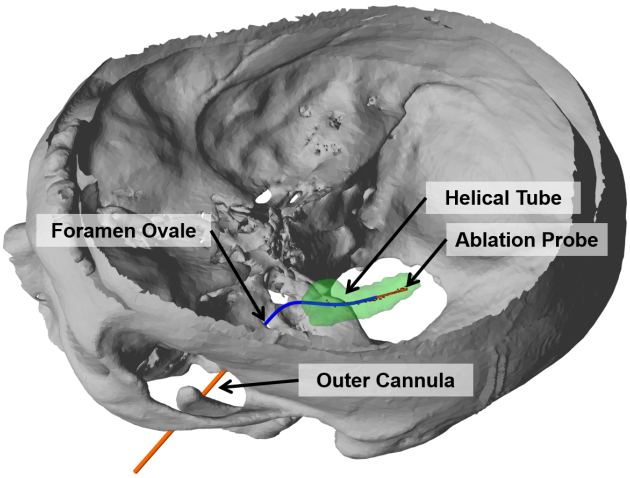

Figure I.4: The transforamenal hippocampotomy concept [28]

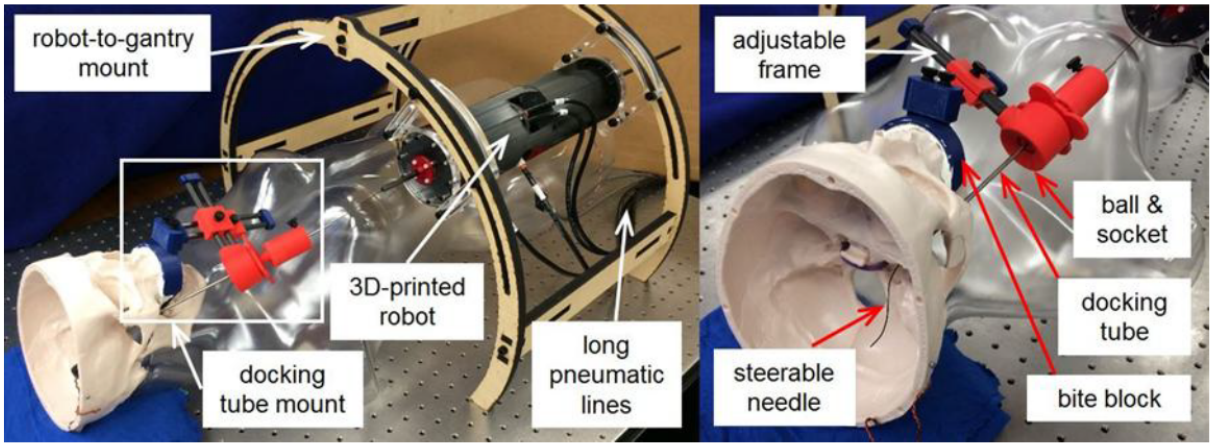

Figure I.5: An MR-compatible, pneumatically actuated robot for driving steerable needles [28]. This prototype also features a traditional stereotactic device (affixed to the patient by a bite block) for manual aiming and insertion of straight outer cannula

Figure I.6: Intuitive Surgical's da Vinci Xi, the latest generation of da Vinci Surgical System

spread to other urologic procedures, with the first robot-assisted nephrectomy being performed in 2001 [31].

Despite its significant dexterity benefits over traditional laparoscopic surgery, robot-assisted surgery has not yet overcome another significant challenge of laparoscopic surgery: minimally invasive surgery still relies primarily on direct visualization via an endoscopic camera for surgical navigation, as pictured in Fig. I.7 [32]. This results in a limited field of view that inhibits surgeons' ability to intuit the anatomical context of the surgical environment, *i.e.* the location of surgical tools relative to critical, frequently subsurface, anatomical features.

This challenge is particularly salient during two critical steps of a partial nephrectomy procedure: first, during the identification of the delicate renal vasculature (which must be dissected from encapsulating fat in order to be clamped prior to cutting the kidney); and again, when identifying the margins around the tumor (which is at least partially endophytic). In the former step, surgeons currently refer to visible anatomical landmarks to

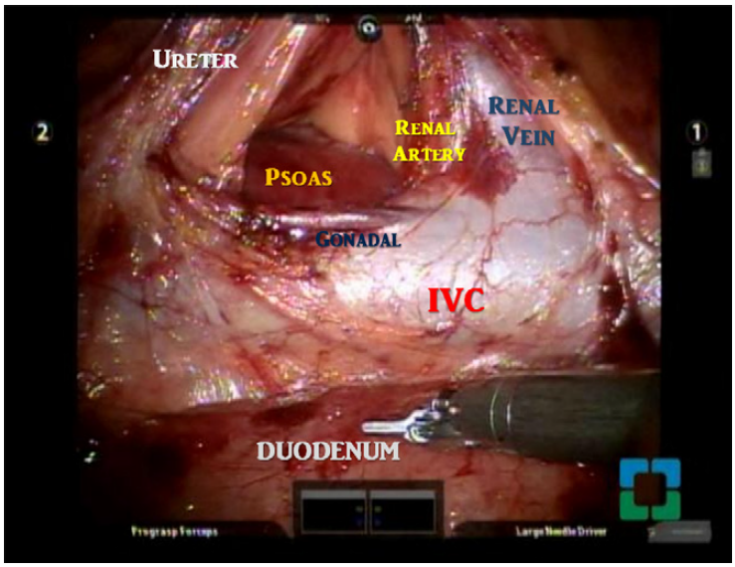

Figure I.7: Endoscopic camera view of a robot-assisted nephrectomy [32]. The limited field of view makes intuiting anatomical context challenging for surgeons

identify a safe area to begin dissection and slowly work toward the general direction of the vasculature—being extremely cautious to avoid accidentally impinging upon the vessels—until the vasculature becomes apparent [32, 33]. In the latter step, intraoperative ultrasound can assist surgeons in identifying tumor margins [32, 33]; however, tissue resection requires use of both hands, leaving surgeons without a hand to manipulate the ultrasound probe.

Preoperative tomographic imaging can provide surgeons with additional spatial and anatomical information to aid in identifying these hidden features; however, in current practice, surgeons must rely on their ability to recall previously viewed images and then mentally register their recollection to the surgical view. The difficulty of this mental registration process, coupled with the potentially disastrous results of inadvertent damage to kidney structures, dissuades many surgeons from attempting partial nephrectomy, despite its known long-term benefits. By translating information from preoperative 3D images directly into the surgical scene, however, an image guidance system for partial nephrectomy promises to aid surgeons' spatial understanding of subsurface anatomy, thereby making identification of critical features easier and more accurate. With more surgeons confidently able to perform

the surgery, partial nephrectomy should see wider utilization.

I.3 Dissertation Contributions

The work proposed for this dissertation touches on disparate clinical applications while pursuing unifying goals of design, implementation, and validation of technologies that enable image-guided interventions using minimally invasive surgical robots. The identified clinical needs inform the nature of this work in each area. In the neurosurgical domain, where image guidance is a mature clinical practice, this dissertation focuses on developing new robotic tools that could revolutionize existing image-guided procedures. In the urologic domain, where surgical robots are a key enabling technology, this dissertation seeks to endow these systems with image guidance capabilities that could give surgeons superhuman sight. The remainder of this dissertation proposal is organized into three content chapters, the key contributions of which are described below.

Chapter II first explores the feasibility of creating helical steerable needles whose geometric properties are tailored to conform to the brain anatomy of individual epilepsy patients during transforamenal hippocampotomy. Additional work in this chapter covers novel control methods and hardware designs that enable the smooth, robotic deployment of such helical needles in the brain. The key contributions of this chapter include:

- Demonstrating the feasibility of using a concentric tube robot to access the hippocampus through the foramen ovale to deliver thermal therapy,
- Validating control methods for accurate follow-the-leader (FTL) deployment of a helical, steerable needle using a pneumatically actuated, MRI-compatible robot,
- Validating a fail-safe method for deploying and retracting helical needles using manual actuation.

Chapter III presents the design and validation of an accurate, clinically practical image guidance system for partial nephrectomy that leverages the inherent capabilities of the

da Vinci robot to achieve image registration using only hardware commonly available in operating rooms. The key contributions of this chapter include:

- Creating a system to implement "touch-based" image-to-physical space registration by using the instruments of the da Vinci robot to digitize anatomical surfaces,
- Analyzing statistical distributions of registration error for this surface-based registration technique,
- Demonstrating the clinical utility of the new image guidance system for localizing subsurface anatomical features.

Chapter IV proposes a new method for implementing image guidance that uses intraoperative, tracked ultrasound to extract anatomical surfaces to enable image guidance registration during robot-assisted partial nephrectomy. The contributions of this work include:

- Determining the feasibility of image registration to a kidney surface reconstructed from ultrasound images acquired through perirenal fat,
- Demonstrating a method to segment sufficient surface information from intraoperative ultrasound to ensure accurate image correspondence in surface-based image registration using kidney and tumor surfaces,
- Evaluating clinical efficacy of ultrasound-based image guidance for robot-assisted partial nephrectomy in phantom studies involving surgeons of various skill levels.

CHAPTER II

Enabling Minimally Invasive, Image-Guided Transforamenal Hippocampotomy through Robotically Actuated Steerable Needles

II.1 Preface

Text sections of this chapter previously appeared in the publications below and have been reproduced here with the permission of co-authors and publishers:

D. B. Comber, **E. B. Pitt**, H. B. Gilbert, M. W. Powelson, E. Matijevich, J. S. Neimat, R. J. Webster, III, and E. J. Barth, "Optimization of Curvilinear Needle Trajectories for Transforamenal Hippocampotomy," Operative Neurosurgery, vol. 13, no. 1, pp. 15-22, 2017.

E. B. Pitt, D. B. Comber, Y. Chen, J. S. Neimat, R. J. Webster, III, and E. J. Barth, "Follow-the-Leader Deployment of Steerable Needles Using a Magnetic Resonance-Compatible Robot with Stepper Actuators," ASME Journal of Medical Devices, vol. 10, no. 2, 2016.

E. B. Pitt, P. J. Swaney, H. B. Gilbert, Y. Chen, R. J. Webster, III, and E. J. Barth, "Enabling Helical Needle Trajectories with Minimal Actuation: A Screw-Based Approach to Concentric Tube Needle Deployment," in Hamlyn Symposium on Medical Robotics, pp. 56-57, 2017.

II.2 Optimization of Curvilinear Needle Trajectories for Transforamenal Hippocampotomy

II.2.1 Introduction

Epilepsy has a point prevalence of about 0.6% globally and accounts for 1% of the global burden of disease in terms of disability-adjusted life years [34, 35]. Forty-seven percent of patients are seizure-free with their first anti-epileptic drug (AED), and an additional 13%

are seizure-free with their second AED [1]. Thus, about 40% of patients are refractory to medical therapy, and many of these are potential surgical candidates. Although epilepsy surgery outcomes reflect seizure-free rates of 70 to 80% [36, 37, 38], only a small fraction of potential surgical candidates are referred for treatment, due in part to physician bias against the highly invasive surgery [6, 5]. Furthermore, the invasiveness of current surgical procedures likely causes many otherwise eligible patients to forgo surgery, despite the high likelihood of a seizure-free outcome.

In recent years, needle-based thermal ablation has been investigated as a minimally-invasive alternative to selective amygdalohippocampectomy (SAH). An SAH resection is less aggressive than standard anterior temporal lobectomy (ATL) but has demonstrated equivalent or near-equivalent outcomes [37]. Parrent and Blume reported amygdalohippocampotomy by MRI-guided radiofrequency ablation (RFA); seizure outcomes were worse than ATL [39]. However, more recent clinical trials using MRI-guided laser ablation systems have more positively indicated the efficacy of percutaneous thermal ablation for epilepsy. Curry et al. reported seizure freedom at 3-month follow up for 5 pediatric patients treated using the Visualase Thermal Therapy System [23]. For a small series of procedures using the Visualase laser, Willie et al. reported 6-month seizure freedom for 7 of 13 patients and substantial improvement for an additional 3 patients [26]. Hawasli et al. effectively treated one case of medically-refractory epilepsy using the Monteris Neuroblate System [40]. Despite some promising results, these ablation procedures to date have not matched the success of SAH. One of the primary limitations of current laser-induced thermal therapy (LITT) procedures is that the laser probes used with currently available devices are restricted to linear trajectories, which cannot lesion the entire hippocampus, even with directionally-aiming probes. Additionally, these procedures still require full operating room preparation for twist-drilling the skull.

This paper investigates a novel approach for accessing the hippocampus through the foramen ovale using helical concentric tube needles. We address the question of whether

concentric tube needles with this geometry can, in principle, guide an ablator along the curved shape of the hippocampus when delivered through the foramen ovale. Through medical image analysis and computer simulation, we determine optimized, curvilinear needle trajectories specific to the anatomy of 20 patients. This is the first paper to consider optimal design of concentric tube needles for a transforamenal approach for accessing the hippocampus and the first paper to consider variations in patient anatomy when considering helical needle design.

II.2.2 Methods

II.2.2.1 The Transforamenal Ablation Concept

Our transforamenal approach is enabled by nonlinear probe trajectories that can also traverse the natural curvature of the hippocampus. These trajectories may offer more complete lesioning than linear trajectories, potentially improving seizure outcomes to equivalency with SAH. The proposed procedure accesses the mesial temporal lobe by cannulation of the foramen ovale. This would eliminate the need for twist-drilling the skull and allow for real-time course correction as the needle insertion is performed in the MRI.

The curvilinear trajectories required are realized using a concentric tube needle. This device consists of nested tubes of superelastic nitinol. Controllable, curvilinear motion is realized when axial translations and rotations are applied to the tube bases. For an overview of this technology, see [41, 42, 43, 44]. A photograph of the concentric tube needle as designed for transforamenal ablation is shown for Fig. II.1. The technique used for creating this prototype needle is discussed in [45]. Deploying this needle through a soft tissue media in a helical trajectory requires precise coordination of both insertion and axial rotation of the component tubes, as was recently described in [46], and is hence typically achieved by attaching motors to tube bases to enable computer control of tube motions. Several particular MRI-compatible robot designs have recently been proposed to accomplish this motion control [47, 48, 49]. Gilbert et al. also explored in simulation the potential benefits

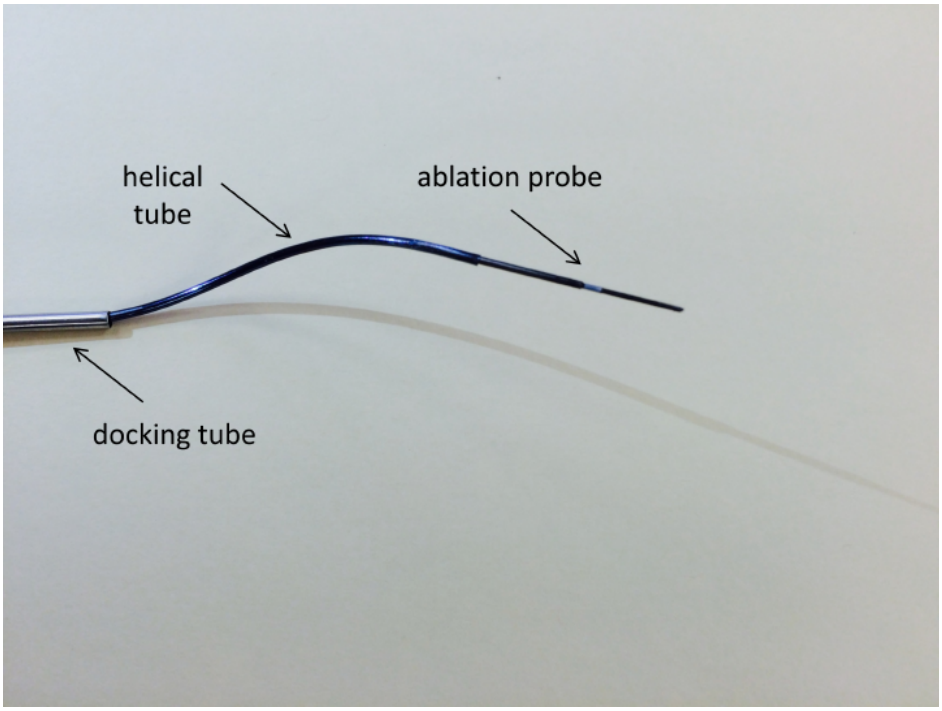

Figure II.1: Photograph of concentric tube needle concept for transforamenal ablation.

of using helical trajectories with a concentric tube needle to access the hippocampus from a burr hole in the rear of the skull [46], but did not consider transforamenal deployment or variation in patient anatomy, both of which we investigate in this paper.

Cannulation of the foramen ovale is often performed for placement of foramen ovale electrodes to monitor the mesial temporal structures [50, 51]. Several research groups have also performed frameless stereotactic cannulation of the foramen ovale for trigeminal rhizotomy [52, 53]. Similarly, for diagnosis and surgical treatment of drug-refractory epilepsy, Ortler et al. reported an optically-tracked aiming device and non-invasive maxillary fixation system called the Vogele-Bale-Hohner (VBH) head holder [54, 55]. This setup facilitates placement of foramen ovale depth electrodes and also mitigates the risk of entering no-go zones like the carotid artery during cannulation.

To enable the transforamenal ablation concept, we envision a robotic, MRI-guided system (see Fig. II.2). The system comprises an MR-compatible actuation unit, a concentric tube robot, an ablation probe, and MRI guidance. We anticipate the procedure could take place

from start to finish in a radiology suite and not require use of a surgical suite. In our envisioned procedure, a robot actuation unit is positioned within a standard MRI scanner with the patient under general anesthesia. The robot is suspended above the patient's torso using an arch-shaped frame affixed to the scanner gantry. The needle in the system is made up of two parts: a docking tube and a robotically actuated concentric tube needle, as shown in Fig. II.1. The docking tube (a 14-gauge needle——a size typically available in trigeminal rhizotomy kits) is an outer cannula manually placed by the neurosurgeon under fluoroscopic guidance to cannulate the foramen ovale prior to transferring the patient to the MRI scanner. The concentric tube needle—consisting of an ablation probe contained within a helically curved superelastic tube—is withdrawn inside the docking tube during cannulation of the foramen ovale. After cannulation of the foramen ovale, the concentric tube needle is deployed by the robot actuation unit (under surgeon control) and guided using real-time MRI for visualization. The helical tube (with the ablation probe retracted inside) passes as close as possible along the medial axis of the hippocampus towards its tail. The ablation probe is then extended a short distance beyond the tip of the helical tube to deliver thermal therapy. Spatial thermal energy deposition is monitored using MR thermal imaging. When sufficient thermal dose is reached at this first position, the ablator is retracted within the helical tube, the helical tube is retracted a short distance along its entry trajectory, and the ablator is re-deployed. This process can be repeated as many times as desired by the physician to achieve desired thermal dose to the hippocampus. The amygdala can also be lesioned if desired by fully retracting the concentric tube robot into the docking tube and then re-inserting along a second trajectory targeting the amygdala.

Previously, we have developed a fail-safe, pneumatic, MRI-compatible robot actuation unit [48]. Figure II.3 shows a photograph of our current prototype assembled for a benchtop simulation of the procedure using an anatomically accurate skull model. Insets in Fig. II.3 show the deployed helical tube inside the skull and the 3D printed bellows mechanism inside the actuation unit. This prototype fits inside a 60 cm MRI scanner bore. During needle

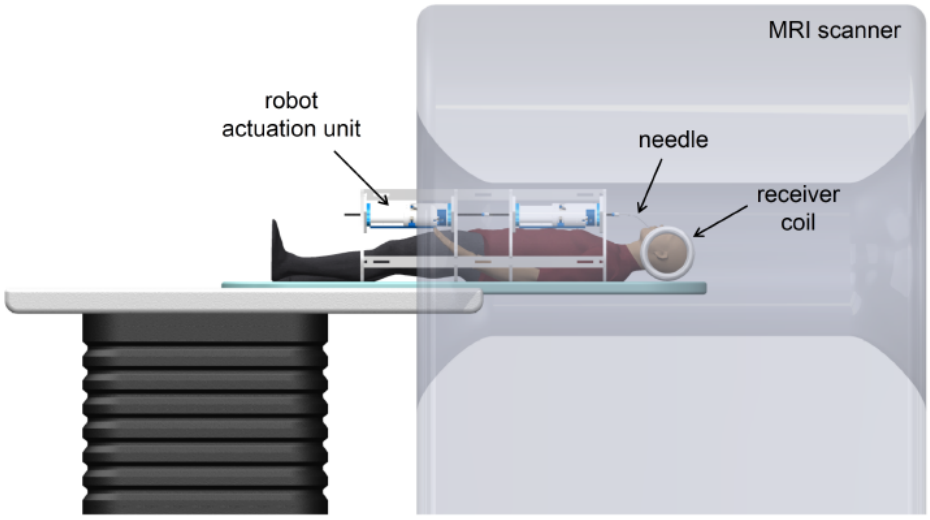

Figure II.2: Illustration of robotic transforamenal ablation system concept.

deployment, the pneumatic robot actuators grasp both the helical tube and the ablation probe at their proximal ends, and apply necessary insertion and axial rotation motions to deliver the helical tube and ablation probe along the desired trajectory. Detailed information on the design, control, and performance of the robot actuation unit can be found in [48].

We note that some aspects of this system concept are not yet fully integrated. In particular, we have developed the MRI compatible robotic hardware and the concentric tube device, and conducted initial experiments to verify MRI compatibility, but we have not yet integrated MRI thermometry or demonstrated use of MRI images to guide the needle to desired points. We also have not yet tested our envisioned procedure in cadaveric or animal models. These are elements of future work.

II.2.2.2 Medical Image Analysis

To characterize the required workspace and constraints for the concentric tube robot, a medical image analysis was conducted. As a retrospective study with exemption approval

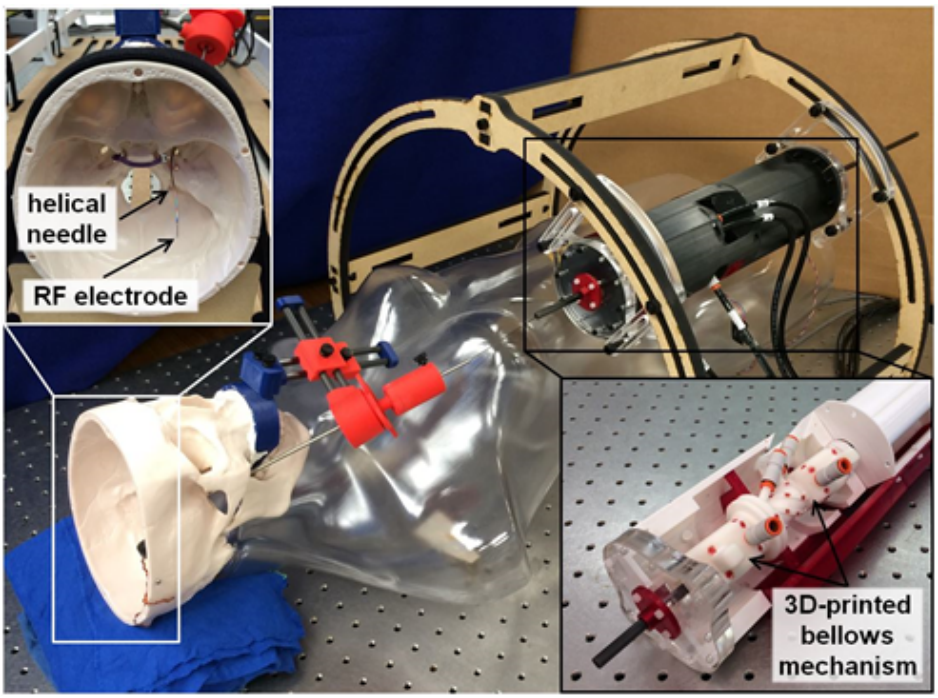

Figure II.3: MRI-compatible robot actuation unit prototype in benchtop mockup of transforamenal ablation procedure.

from the Vanderbilt University Institutional Review Board, dual CT/MR image volumes were obtained and de-identified. Image sets for 10 patients were selected based only on whether a sufficient amount of mandible and maxillary bone were included in the CT scan. This was to ensure adequate information to inform the design of cannula orientation angles for cannulation of the foramen ovale. No prior indication as to whether the hippocampus would be convenient to reach through the foramen ovale influenced patient selection.

Visualization and analysis of the image volumes were performed using the open source 3D Slicer software (www.slicer.org). The CT and MR image volumes were registered by a rigid transformation plus scaling using Slicer's BRAINSFit module [56]. The skull was segmented from the CT volume using an automated threshold. The hippocampi and amygdala were segmented manually from the MRI volume and reviewed and confirmed by an experienced neurosurgeon (Dr. Neimat, who is a co-author on this paper.

II.2.2.3 Concentric Tube Needle Design

The skull, hippocampus, and foramen ovale models were used to design a concentric tube needle trajectory for each patient. Our design objective was to cause the ablator to pass as close to the medial axis as possible. The medial axis is the locus of the centers of all maximal spheres inscribed within the object, where maximal spheres touch more than one point on the object boundary [57]. The rationale for this approach is that if the ablator radiates heat evenly in all directions, it will be most likely to achieve uniform coverage of the hippocampus if it travels along the medial axis. However, we note that the ablator need not travel perfectly along the axis, as there are examples of successful ablations being performed substantially away from the medial axis [23, 26, 40].

In this application, the concentric tube needle trajectory is fully defined by seven parameters: helix curvature, helix torsion, helix maximum insertion length, helix initial rotation, ablation probe maximum insertion length, and the two orientation angles of the docking tube. Note that the curvature and torsion define the geometry of the helical tube whereas the other five parameters describe the needle and ablator placement. To achieve our design objective, we performed a numerical optimization to determine the set of seven parameters that minimized the mean distance from each point on the medial axis of the hippocampus of each patient to the closest point on the concentric tube needle's backbone. The segmented anatomical models were imported to MATLAB so that they could be overlaid with possible trajectories of the concentric tube needle. The medial axis was computed using the skeletonizing method of [57]. To generate an initial set of parameters for the numerical optimization, a needle trajectory capable of closely following the medial axis was manually designed using the forward kinematic equations of the helical concentric tube robot. An example of this manual design is shown for Patient 4 in Fig. II.4. Numerical optimization of the trajectory parameters was then performed using the well-established Nelder-Mead simplex method, which was implemented with the MATLAB *fminsearch* function [58]. During optimization, a limitation was placed on the helix curvature to ensure that the needle would

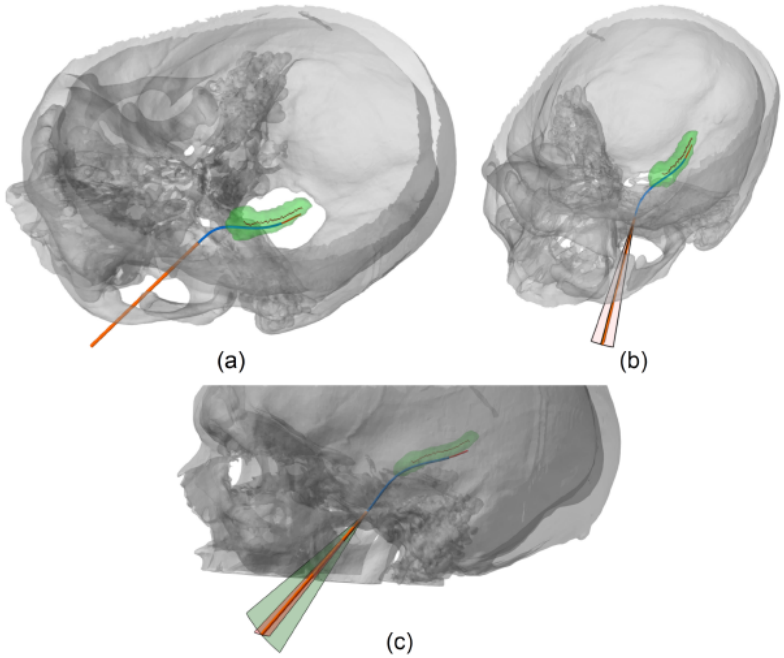

Figure II.4: (a) Initial transforamenal trajectory before numerical optimization. (b, c) Docking tube range of allowable motion.

not plastically deform when straightened inside the docking tube. A maximum of 8% strain was allowed for helical tube curvature; this is the often-quoted recoverable strain limit for nitinol in the literature. Additional constraints were placed on the orientation angles of the docking tube to ensure that the needle trajectory did not exceed the safe insertion region. Specifically, using the skull model, we defined a coordinate frame for the docking tube such that its central axis lies in a plane of maximum adjustability in the space between maxilla and mandible. This plane is approximately sagittal and the corresponding range of motion is illustrated by the larger circular sector in Fig. II.4(c). This range of allowable motion was constrained in the optimization to $\pm 10°$, and for the orthogonal plane shown in Fig. II.4(b), a constraint of $\pm 5°$ was imposed. All parameter limits were enforced via cost conditions in the numerical optimization.

II.2.3 Results

The optimized concentric tube robot design for Patient 4 is shown in Fig. II.5. A comparison of initial (Fig. II.4) to optimized designs shows a substantial improvement in the accuracy of the trajectory to traverse the medial axis of the hippocampus. A summary of all 20 optimized designs is provided in Fig. II.6 and Tbl. II.1. Figure 6 shows the medial axis of each hippocampus and each trajectory at its maximum path distance from the foramen ovale. Across all 20 cases, the mean distances (error) between hippocampus medial axis and backbone of the needle were 0.55, 1.11, and 1.66 mm for best, mean, and worst case, respectively. For each case, a helical curvature was found that resulted in strains less than the recoverable limit.

Considering the summary of the optimized design parameters given in Tbl. II.1, there are several reasons why patient-specific designs were required to achieve sufficient accuracy. First, the helical tube torsion is positive for the left hippocampus and negative for the right hippocampus, so at least two different needles are required. Second, optimized torsion varied by $\pm 25\%$ from the mean (89.1 $\mathrm{m}^{-1}\mathrm{rad}^{-1}$) for the set of right-handed helices and by $\pm 19\%$ from the mean (107.3 $\mathrm{m}^{-1}\mathrm{rad}^{-1}$) for the left-handed helices. If a generic shaped needle were used instead, this amount of variation from optimal torsion would result in additional trajectory error of 3 to 5 mm.

It is feasible to rapidly and accurately fabricate patient-specific needles using shape setting of superelastic nitinol. For this work, we used a laboratory-grade electric heating method developed by our lab [45] to rapidly prototype a concentric tube needle for Patient 1, using a superelastic nitinol tube of outer and inner diameters 1.14 and 0.97 mm, respectively. The fabricated prototype had a curvature of 41.2 m^{-1} and a torsion of 84.8 m^{-1}. The geometry of this prototype deviates slightly from the optimized geometry given in Table II.1; however, we note that this deviation results from current limitations of the rapid prototyping technique. Albeit more expensive, industrial methods for shape setting of nitinol would be able to achieve desired geometry with substantially greater accuracy on appropriate timescales

Table II.1: Concentric tube robot design parameters and corresponding error predictions

Patient	**Helically Pre-curved Tube**			**Ablation Probe**	
	Max. Length (mm)	Curvature (m^{-1})	Torsion (m^{-1})	Max. Length (mm)	Mean Error (mm)
2 Left	56.2	78.3	107.0	71.2	0.81
2 Right	56.0	83.9	-118	65.0	1.26
3 Left	52.8	49.7	94.9	60.6	0.74
3 Right	42.6	44.9	-112.9	51.9	1.14
4 Left	46.3	50.6	84.1	63.1	0.59
4 Right	50.0	55.1	-102.8	61.1	0.55
5 Left	33.8	43.6	92.5	57.4	0.86
5 Right	45.5	57.0	-111.3	58.9	1.26
6 Left	48.3	39.9	102.7	58.1	1.49
6 Right	47.2	29.9	-101.5	54.9	1.62
7 Left	58.7	32.4	72.2	64.8	1.43
7 Right	56.5	34.1	-84.7	62.0	0.90
8 Left	58.2	39.5	77.8	63.6	1.17
8 Right	48.5	48.9	-114.0	62.3	1.64
9 Left	58.4	62.3	102.1	64.9	1.59
9 Right	52.6	59.0	-125.8	62.4	1.66
10 Left	55.0	32.9	62.9	63.5	0.90
10 Right	55.2	36.8	-91.2	63.3	1.03

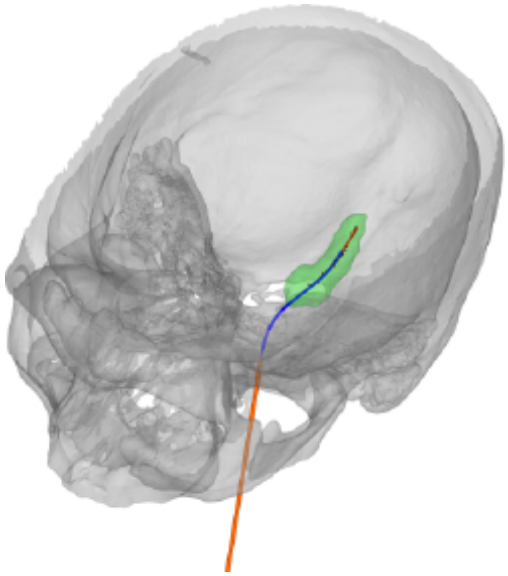

Figure II.5: Optimized concentric tube robot design for Patient 4.

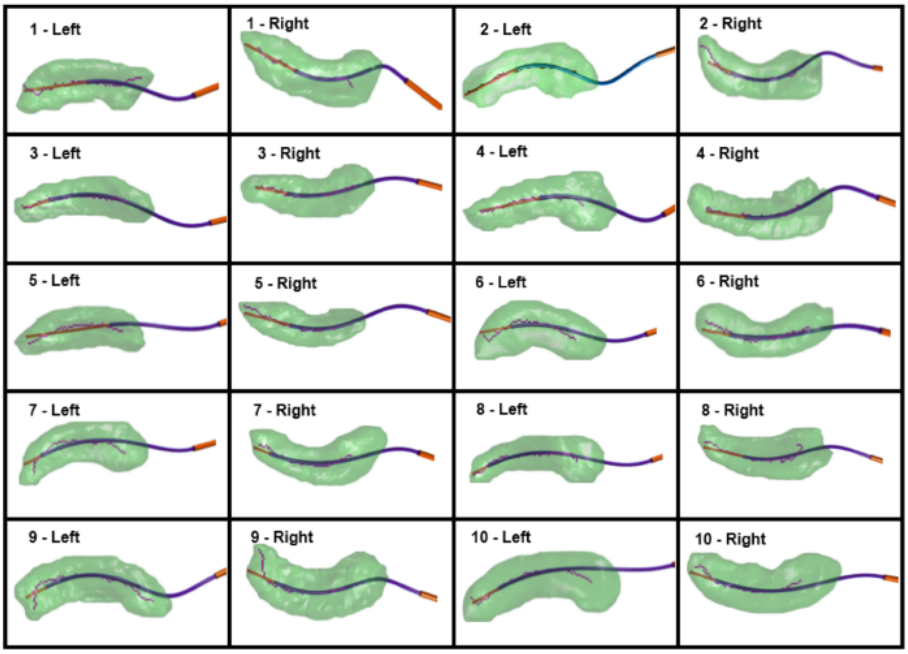

Figure II.6: Optimized concentric tube robot designs for 20 hippocampi, axial view.

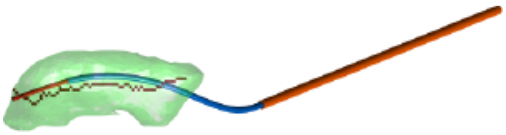

Figure II.7: Optimized trajectory using measured curvature and torsion of prototype.

for our envisioned procedure. Using the measured geometry of the prototype needle, we repeated the optimization to find an optimal set of five insertion parameters for the prototype needle. In simulation, this new trajectory follows the medial axis of the hippocampus at a mean error distance of 1.80 mm and is illustrated in Fig. II.7.

II.2.4 Discussion

This paper has described a novel approach to access the hippocampus through the foramen ovale using a concentric tube robot for the purpose of hippocampotomy by ablation. We have presented a computer simulation of optimized helical needle trajectories for accurate traversal of the curvilinear medial axis of 20 hippocampi. This is the first paper to consider optimal design of concentric tube needles for a transforamenal approach for accessing the

hippocampus. This is also the first paper to address variations in patient anatomy when considering helical tube optimization. A prototype needle with sufficiently accurate pre-curvature for this application was also manufactured. These trajectories potentially enable ablation of tissue—in particular, in the tail of the hippocampus—that cannot typically be reached by linear trajectories. In light of correlation between higher resection volume and better clinical outcomes [59], the potential to achieve more complete ablation could improve the efficacy of hippocampotomy by ablation for the treatment of epilepsy. Though significant additional testing is necessary to confirm the feasibility of this procedure, the results of this study preliminarily suggest that MRI-guided transforamenal ablation could be a less-invasive alternative to current ablation treatments for epilepsy and may ultimately provide a more complete ablation.

The eventual realization of our envisioned procedure will require much future work in both technical and clinical aspects. One area of work in concentric tube robots is to explore the effects of friction between tubes, especially in light of the relatively long transmission length required for our approach. One prior paper on this topic suggests modelling friction as an axial torque located at the end of the straight transmission section of the tubes [60]. This friction model can be integrated into the mechanics-based model of the tubes [42, 43], and we expect that it will be straightforward to compensate for friction with our actuators, or to mitigate it with stiffer straight transmissions [61] and/or with low-friction coatings. Further areas of technical work for our system include evaluating imaging protocols for MR thermometry and integrated of MRI guidance for our robot. A variety of ablation technologies are possible, and additional work will also be needed to choose the best technology for this application. An important clinical concern to be addressed in future design work is the ability to extract a concentric tube needle in the event of a failure of the robotic actuation system after insertion in the temporal lobe. Many other clinical aspects of our envisioned procedure will also need to be extensively evaluated in future cadaver and animal studies.

II.3 Follow-the-Leader Deployment of Steerable Needles Using a Magnetic Resonance-Compatible Robot with Stepper Actuators

II.3.1 Background

Epilepsy is a debilitating, potentially fatal, seizure-causing neurological disorder that will affect approximately 1% of people worldwide in their lifetimes [1]. Medication-based treatment is ineffective for an estimated 40% of epilepsy patients [1]. As an alternative to medication, surgical removal of the hippocampus (commonly the origin of epileptic seizures) successfully cures epileptic seizures in about 70% of cases [4]; however, 50-90% of eligible patients forgo surgery due to risks associated with highly-invasive brain surgery [4, 5].

Magnetic resonance image-guided (MRI-guided) laser ablation of the hippocampus is a promising avenue for minimally invasive surgical treatment of epilepsy. Recent clinical trials using various needle-based, MRI-guided laser ablation systems to treat epilepsy have reported positive results; however, seizure outcomes were worse than those of epilepsy surgery [26]. These ablation systems exhibit one major limitation: linear needle trajectories are unable to traverse the entire curved structure of the hippocampus.

Steerable needles——comprising concentric tubes of pre-curved superelastic nitinol——address this limitation by enabling curvilinear needle trajectories in soft tissue. The potential benefits of curvilinear trajectories are twofold: (1) they enable therapy delivery to a larger region of the hippocampus; and (2) they enable accurate needle placement while avoiding sensitive, untreated tissue that might otherwise obstruct a typical linear trajectory [46]. To achieve curvilinear trajectories without shearing tissue, however, steerable needles must be deployed in a "follow-the-leader" (FTL) fashion, whereby the needle backbone follows the path created by the needle tip [46]. Precise coordination of needle insertion and rotation required for FTL deployment necessitates robotic actuation.

Research on MRI-compatible robotic needle-actuation systems has focused primarily on straight needle placement (see, e.g., [62]; for a more general review of MRI-compatible robotics, see [63]). To enable use of steerable needles for MRI-guided epilepsy surgery,

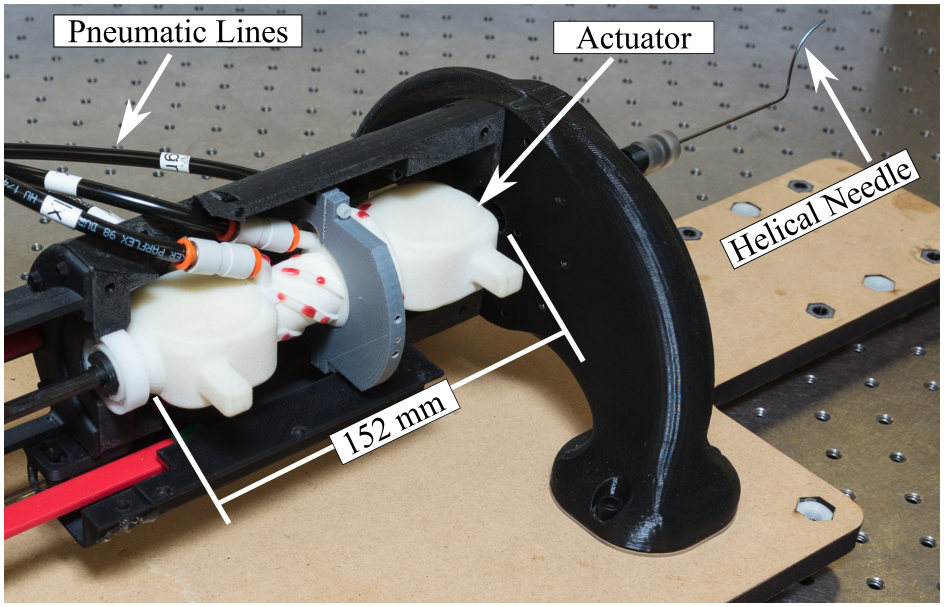

Figure II.8: Robot with Helical Steerable Needle

we previously developed a compact, pneumatically-actuated, additively manufactured, fail-safe, MR-compatible robotic needle-driving system [48]. This paper presents a joint-level trajectory coordinator for FTL deployment of a steerable needle using our MRI-compatible robot. FTL deployment is validated experimentally.

II.3.2 Methods

Our MRI-compatible robot system, pictured in Fig. II.8, uses a 2 degree-of-freedom pneumatic stepper actuator to drive a helical steerable needle. The actuator is an additively manufactured monolithic structure comprising both a linear and a rotary flexible fluidic actuator (FFA). Actuation is achieved by inflation of the FFAs, causing translational or rotational deformation, respectively. Flat diaphragm grippers are inflated around clamshell inserts to grasp a transmission tube at the needle base. Detailed design, operation, and low-level nonlinear position control are presented in [48].

During operation, the superelastic needle deploys from a fixed, straight outer cannula (not pictured in Fig. II.8), and the distal end of the needle returns to its helical shape as it exits the cannula. Since a portion of the needle remains straightened inside the cannula, the

displaced arc length and rotation of the deployed helix respectively equal the translation, x, and rotation, θ, of the needle base at the actuator. During FTL deployment, x and θ must be coordinated such that they follow the geometric relationship between helix arc length and rotation:

$$x = \theta\sqrt{r^2 + p^2}, \tag{II.1}$$

where r and p are the helix radius and pitch, respectively.

To achieve FTL deployment using the stepper actuator, a joint-level trajectory coordinator determines the desired translation and rotation of the actuator (denoted by subscript *des*) during each actuation step. The trajectory coordinator accepts final desired displacements as inputs. For each actuation step (denoted by superscript k), the coordinator increments the desired rotation by a fixed step size, θ_{step}, which may be any fraction of the maximum rotational step size,

$$\theta_{des}^{k} = \theta_{des}^{k-1} + \theta_{step}, \tag{II.2}$$

and the desired translation is incremented according to (II.1),

$$x_{des}^{k} = x_{des}^{k-1} + \theta_{step}\sqrt{r^2 + p^2}, \tag{II.3}$$

until the desired displacements are saturated at their respective final values. The updated desired displacements are sent as inputs to the low-level position controller during each actuation step. The present actuator design is not capable of simultaneous translation and rotation, so each actuation step consists of a rotational substep followed by a translational substep. Beyond enforcing FTL conditions, this technique differs from previous implementations in that trajectory tracking by the low-level controller occurs during each step of the desired trajectory (not just in the vicinity of the final desired displacement).

To validate this trajectory coordinator for FTL needle deployment, a helical needle of radius 3.65 mm and pitch 10.53 mm/rad was deployed through a straight outer cannula into a gelatin-based phantom. Actuation substeps were performed at a frequency of 0.5 Hz (0.25

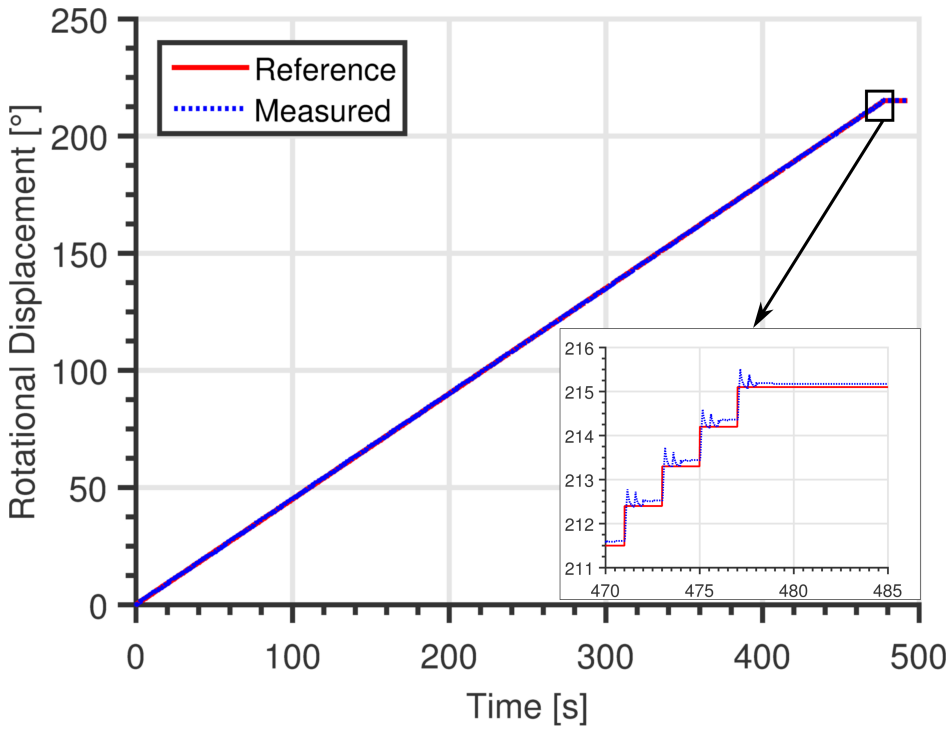

Figure II.9: Rotational Displacement Tracking

Hz full step frequency), and $\theta_{step} = 1°$. Needle position was measured using optical encoder hardware described in [48].

II.3.3 Results

Figures II.9 and 3 show successful tracking of both the desired translational and rotational trajectories. The measured final translation error was 0.046 mm, and the measured final rotational displacement error was 0.072°. The small overshoot (at most 0.41°) seen in each rotary substep is negligible for the intended application (see [48] for detailed performance specifications based on the intended clinical application). Furthermore, note that since the low-level position controller operates continuously during each actuation step, tracking errors do not accumulate from step-to-step, even as the desired displacement increments.

Figure II.11 demonstrates the adherence to FTL conditions. The "reference" signal was calculated according to (II.1), using the measured angular displacement and helix geometric parameters. Small deviation from the FTL trajectory is observed at each substep due to the

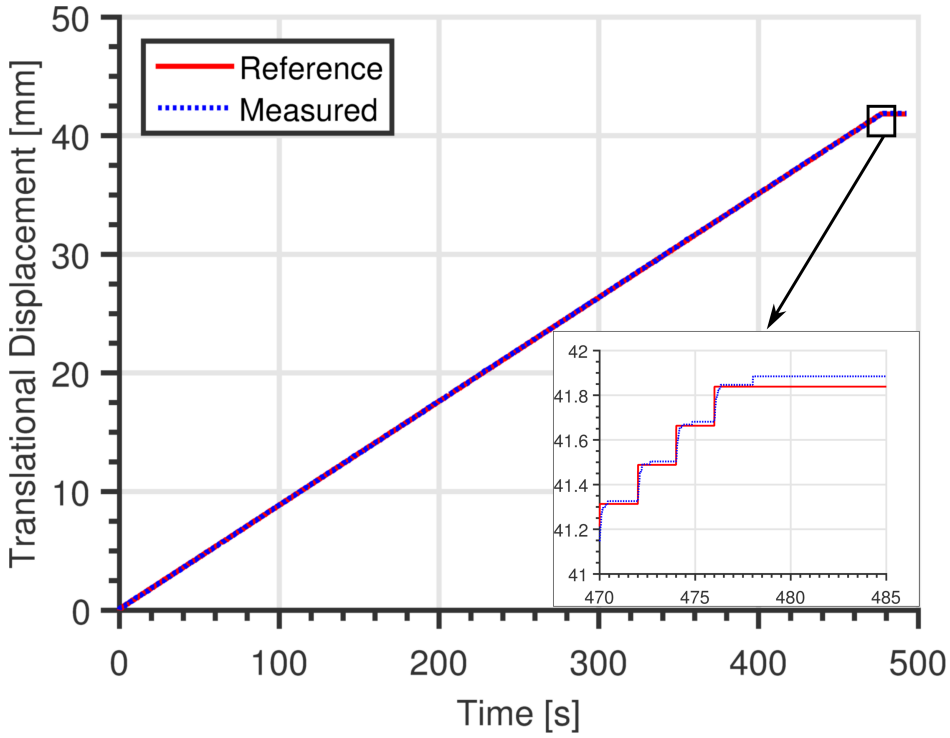

Figure II.10: Translational Displacement Tracking

discrete rotational and translational substeps. The maximum deviation of the translational displacement from the FTL value was 0.25 mm, which is likely sufficiently small for the intended application. The final deviation of the translational displacement from the FTL value is zero within the resolution of encoder hardware.

II.3.4 Interpretation

This technical brief presented a joint-level trajectory coordination technique for follow-the-leader deployment of a helical steerable needle using a previously developed MRI-compatible robotic system with stepper actuators. Experimental results using the proposed trajectory coordinator demonstrated follow-the-leader needle deployment that is sufficiently accurate for the intended clinical application of needle-based surgical treatment of epilepsy. Future work will include ex vivo targeting experiments with MRI guidance.

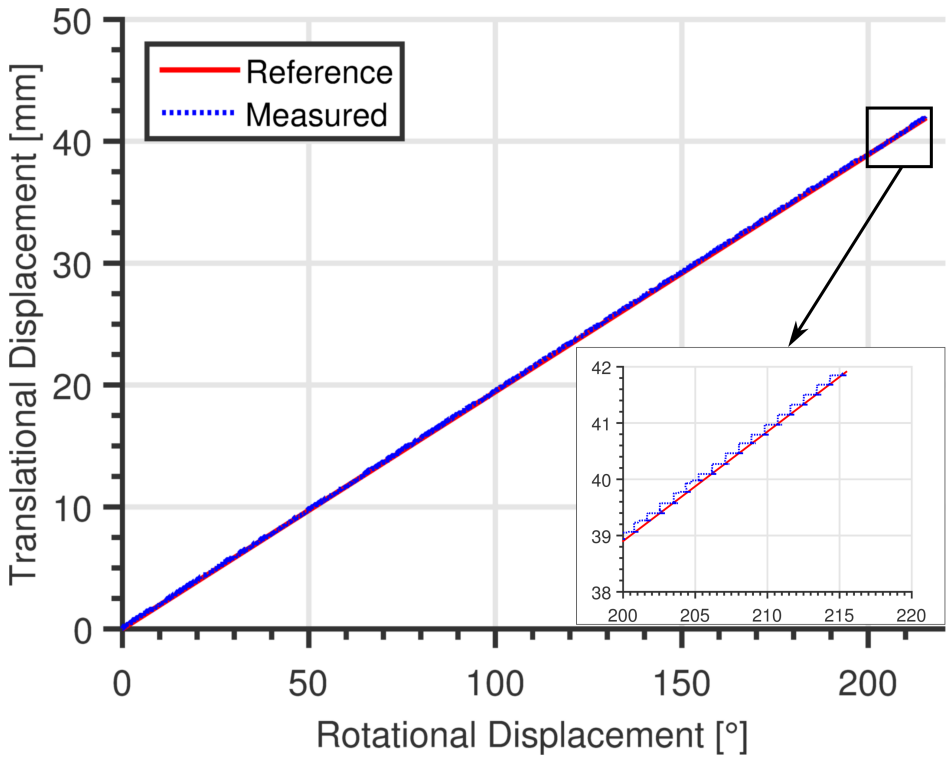

Figure II.11: FTL Deployment

II.4 Enabling Helical Needle Trajectories with Minimal Actuation: A Screw-Based Approach to Concentric Tube Needle Deployment

II.4.1 Introduction

The clinical need for needle-based therapies capable of accessing tissues unreachable by conventional needles has motivated substantial research into steerable needles (see [64] and [65] for a review of these technologies). In particular, it has been observed that curved paths can be useful in percutaneous procedures [66]. Gilbert, et al., showed that helically pre-curved concentric tube nitinol needles can be deployed in a follow-the-leader (FTL) fashion, such that the needle shaft follows the path traced out by the tip [46]. Further information on concentric tube robots and the mechanics-based models that govern their motion can be found in [42] and [43].

The motivating application for helical needles in [46] was minimally invasive treatment of epilepsy—a neurological disorder that causes debilitating seizures. We have been developing

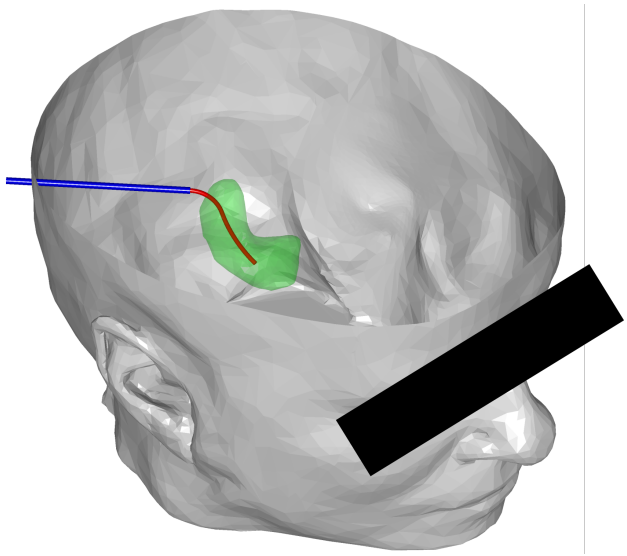

Figure II.12: Minimally invasive, helical needle-based treatment of epilepsy. A helical needle (red) deployed from an outer cannula (blue) delivers therapy to the hippocampus (green)

a needle-based procedure for this application that involves delivering thermal energy to the hippocampus with both guidance and thermometry from magnetic resonance imaging (MRI) [46, 48, 67]. Figure II.12 illustrates this application, in which a helical concentric tube needle is used to deliver therapy to the curved structure of the hippocampus through an occipital burr hole in the skull.

A principal challenge to executing FTL deployment of a helical concentric tube needle in soft tissue is the requirement for precise coordination of needle rotation and translation necessary to achieve a smooth "corkscrew-like" motion. To address this, Comber, et al., developed an MRI-compatible needle-driving robot for the aforementioned epilepsy application [48], and Pitt, *et al.*, demonstrated the same robot's ability to accurately achieve FTL deployment of a helical needle [67].

The motivation for our current paper comes from the observation that FTL deployment requires the two actuation degrees of freedom to move at a fixed rate relative to one another, meaning that deployment is actually a single degree-of-freedom operation. Thus, in this paper we mechanically couple the two traditional actuation degrees of freedom through a screw mechanism. The benefit of this approach is that one actuator can be eliminated from

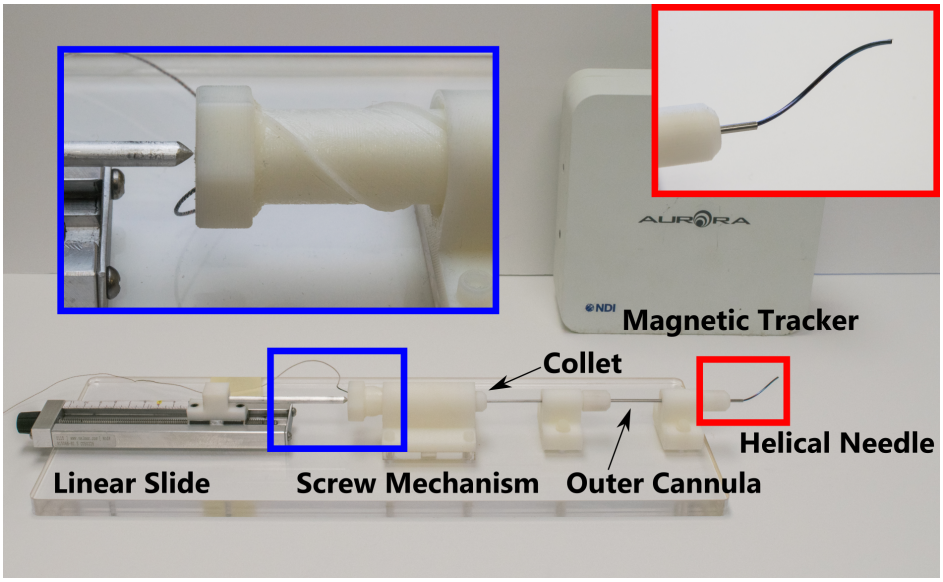

Figure II.13: Experimental setup for characterizing deployment of a helical needle using a screw mechanism

the robotic system, making it simpler and less expensive. A further benefit of the approach is that manual insertion of a helical concentric tube robot becomes straightforward, allowing a human operator to deploy the needle in a FTL path by pushing linearly on the back of the screw mechanism. This paper is the first to demonstrate FTL deployment of a helical concentric tube needle by manual actuation.

II.4.2 Materials and Methods

Figure II.13 shows the screw mechanism and helical needle, assembled in the experimental setup. The prototype screw was manufactured by fused deposition modeling of acrylonitrile butadiene styrene (ABS) using a Stratasys Dimension 768SST. The process of shape setting the helical needle is described in [45].

The superelastic nitinol helical needle is grasped at its base by a collet in the tip of the screw mechanism. The needle is deployed through a fixed, straight, rigid outer cannula. When retracted within the cannula, the needle straightens; however, as the needle deploys from the end of the cannula, the deployed portion of the needle returns to its pre-curved helical shape due to the superelastic properties of nitinol. Achieving FTL deployment requires

that the base of the needle be rotated (simultaneously with translation) at a rate equal to the needle's pre-curved torsion [46]. A simple screw mechanism is ideally suited to maintain the required constant relationship between translation and rotation. For the system presented here, the helical needle had radius 4.84 mm and pitch 62.38 mm, and the screw mechanism had pitch 69.39 mm.

To assess the quality of the FTL trajectory during insertion and retraction, the path of the needle tip through 3D space was compared to the helical pre-curved shape of the needle. A total of 20 experiments (10 insertions and 10 retractions) were performed in free space. Needle behavior in soft brain tissue should not be expected to differ significantly from behavior in free space, given the high relative stiffness of the needle compared to brain tissue. In all experiments, actuation of the screw mechanism was performed manually. Needle tip position was measured with a Northern Digital, Inc. Aurora magnetic tracking system; insertion distance (deployed arc length) was measured using digital calipers and an aluminium probe mounted to a linear slide (see Fig. II.13). During each experiment, needle tip position was measured at 5 mm increments of deployed arc length. To determine the position and orientation of the needle's known (i.e. pre-shaped) helical curve in the robot's base frame, a point based registration was carried out between all measured data points and the points at corresponding arc length locations on the needle curve.

II.4.3 Results

Figure II.14 shows the results of one insertion experiment and one retraction experiment. In an ideal FTL deployment, the position of the needle tip would lie exactly on the curve at all times. For a given arc length, the distance between the measured tip position and the point on the curve at the same arc length is a measure of FTL error. Figure II.15 shows the FTL error as a function of arc length.

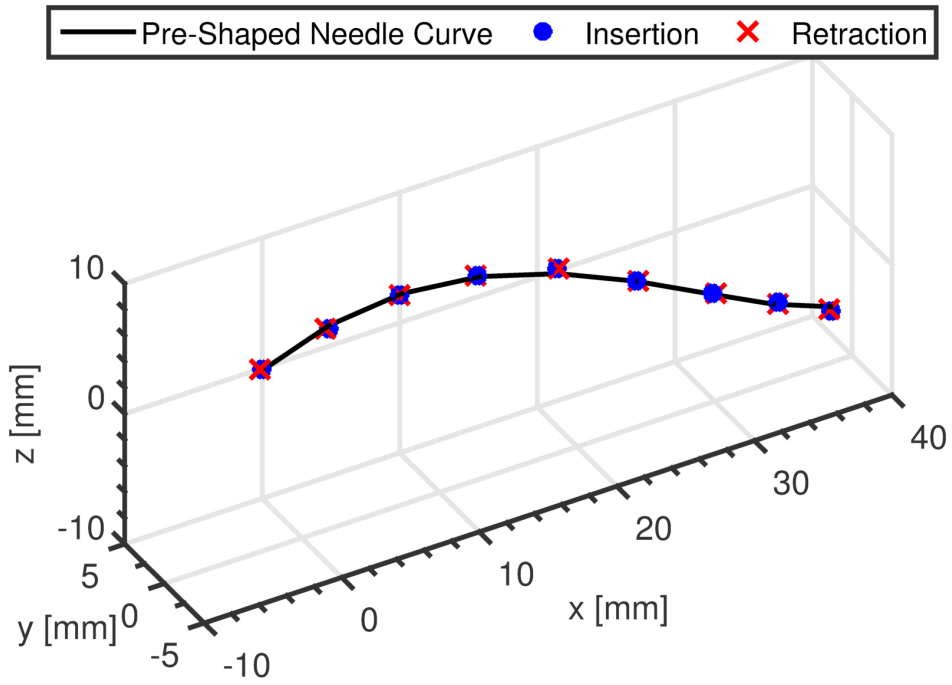

Figure II.14: Point-based registration between measured needle tip positions and the pre-shaped needle curve

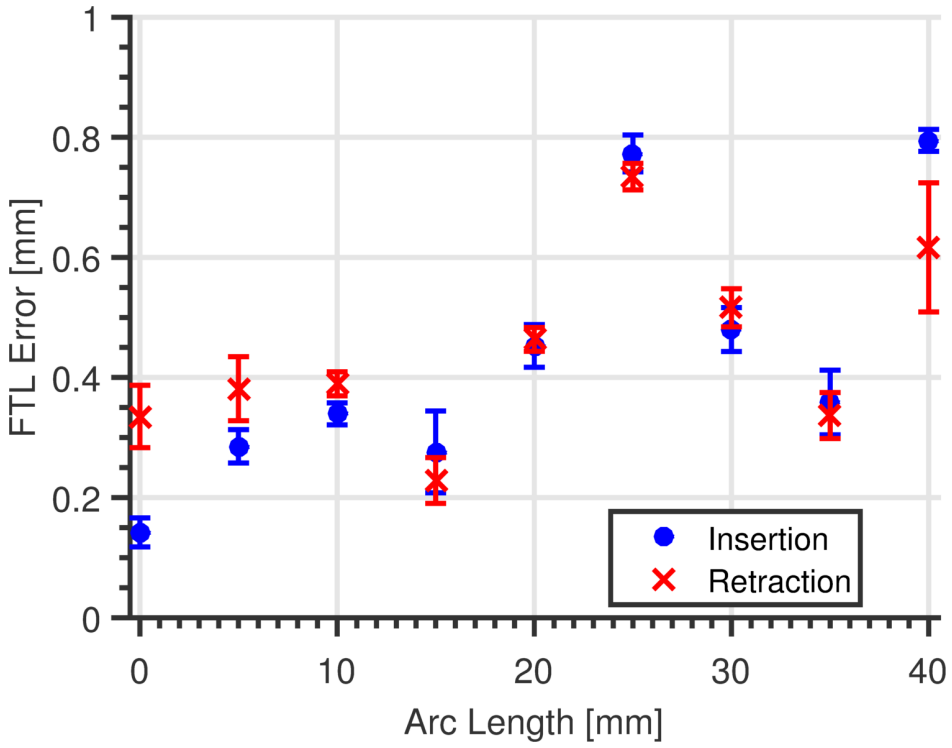

Figure II.15: FTL error versus arc length for insertion and retraction. Reported values represent mean FTL error for all experiments. Error bars represent average absolute deviation from the mean for all experiments.

II.4.4 Discussion

The results presented here demonstrate that follow the leader deployment of a helical concentric tube robot can be achieved manually using a screw mechanism to mechanically couple the translational and rotational degrees of freedom. These results provide for the first time a straightforward method to manually insert helical concentric tube needles through a FTL trajectory. Additionally, these results enable a reduction in the cost and complexity of a robot designed to achieve FTL deployment of a helical concentric tube needle by eliminating one actuator.

II.5 Postface

Following the initial design and characterization of the manual actuation mechanism, additional work investigated the feasibility of using a helical needle to deliver thermal therapy in tissue, along a desired path [68]. This work confirmed the hypothesis that the shape of ablation volume can be predicted from the needle geometry.

CHAPTER III

Toward Practical and Accurate Touch-Based Image Guidance for Partial Nephrectomy using the da Vinci Surgical System

III.1 Preface

Text sections of this chapter previously appeared in the publication below and have been reproduced here with the permission of co-authors and publishers:

> James. M. Ferguson*, **E. Bryn. Pitt***, Nicholas. L. Kavoussi, Andria. A. Remirez, Michael. A. Siebold, Alan Kuntz, Eric. J. Barth, S. Duke. Herrell, and Robert. J. Webster III, "Toward Practical and Accurate Touch-Based Image Guidance for Partial Nephrectomy using the da Vinci Surgical System," IEEE Transactions on Medical Robotics and Bionics, vol. 2, no. 2, pp. 196-205, May 2020. ***Co-first author**

III.2 Introduction

Treatment of renal cell carcinoma typically requires surgically removing the tumor and surrounding kidney tissue. Some cases require radical nephrectomy, in which the entire kidney is removed. However, for patients with localized tumors, the American Urological Association and the European Association of Urology recommend nephron-sparing partial nephrectomy, in which only part of the kidney is removed [9, 10]. Compared to radical nephrectomy, partial nephrectomy leads to improved long-term patient outcomes by allowing the patient to retain some kidney function and reducing the risk of chronic kidney disease [11, 12]. Partial nephrectomy remains underutilized, however, likely due to the extreme technical challenges associated with the procedure, especially when performed minimally invasively [14, 15].

Robot-assisted partial nephrectomy (RAPN) performed using the da Vinci Surgical System (Intuitive Surgical, Inc., Sunnyvale, CA, USA) can help mitigate many challenges of minimally invasive partial nephrectomy [13], but RAPN does not inherently address the challenge of relying primarily on direct visualization via an endoscopic camera for surgical

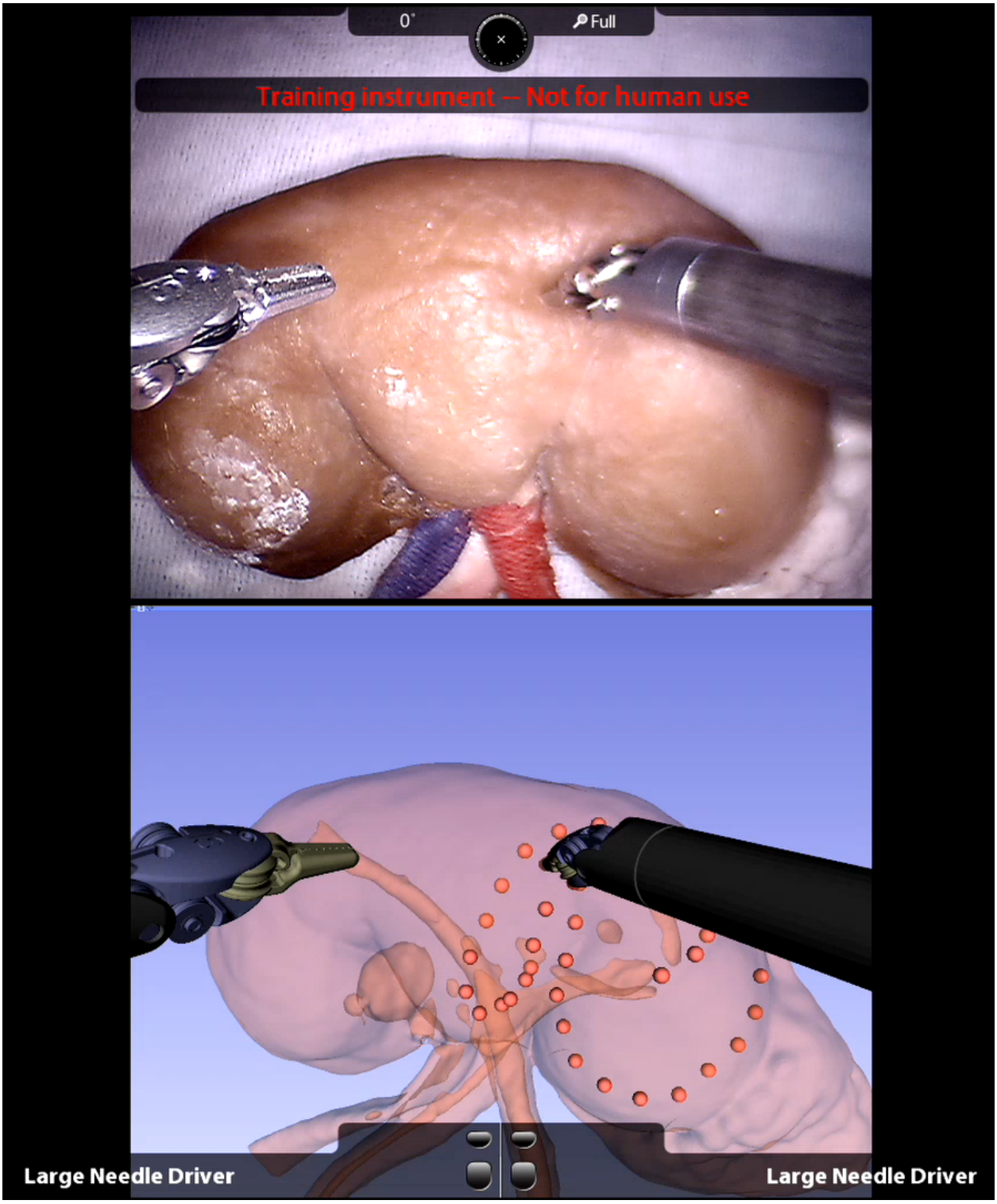

Figure III.1: Our image guidance display, as seen from the surgeon console of a clinical da Vinci *Si*. As the surgeon lightly traces the kidney surface with the robot instrument tip, our system collects surface data (red dots, downsampled for visualization) that can be used to register segmented preoperative image data to the organ surface. This provides the surgeon with the locations of critical subsurface anatomical structures.

navigation. This results in a limited field of view that inhibits surgeons' ability to intuit the anatomical context of the surgical environment, *i.e.* the location of surgical tools relative to critical, frequently subsurface, anatomical features. Locating these anatomical features, such as large blood vessels and the tumor itself, is critical to safely and successfully performing RAPN. Surgical image guidance can help surgeons locate these features, providing additional anatomical context by accurately registering 3D anatomical volumes (typically generated by segmentation of preoperative computed tomography (CT) or magnetic resonance (MR) images) to the surgical environment and displaying this information to the surgeon during the procedure (see Fig. III.1). Accurate image guidance has the potential to improve patient outcomes by making localization, dissection, and isolation of critical vascular and organ structures, as well as correct margin selection, easier for surgeons.

It has been suggested that the da Vinci robot's kinematics could be used to achieve accurate registration for image guidance [69, 70]. In this work, we create such a system, quantify its performance, and demonstrate its ability to improve an experienced surgeon's performance. Our image guidance system uses the instruments of the da Vinci robot itself as 3D localizers for digitizing anatomical surfaces. By lightly tracing an instrument tip over the surface of the target anatomy while recording the robot's joint values, our system generates a set of points on the surface of the anatomy. Our system computes a surface-based registration between the preoperative images and the patient's anatomy during the surgery. Using this registration, we then display a 3D model of the patient's anatomy segmented from the preoperative imaging to the surgeon in the da Vinci's surgeon console, enabling the surgeon to visualize the location of subsurface anatomy that is not visible via the endoscope (see Fig. III.1). By using the inherent capabilities of the da Vinci for registration, our system provides an image guidance approach that is well suited to the clinical workflow.

This paper presents our touch-based image guidance system and analyzes its accuracy. We also describe practical steps for deploying it in the operating room using a clinical da Vinci *Si* system. We present a series of phantom experiments to provide a thorough

accuracy analysis of a touch-based registration for image guidance. Finally, we present a phantom experiment demonstrating the utility of our image guidance system for improving an experienced surgeon's ability to localize subsurface anatomical features important in partial nephrectomy. By providing practical and accurate image guidance, our method has the potential to improve surgeons' ability to accurately accomplish partial nephrectomy. Success in achieving this has the potential to increase utilization of partial nephrectomy, thereby providing enhanced health outcomes to many more patients.

III.3 Related Work

Image guidance has previously been recognized as potentially useful in facilitating partial nephrectomy, and numerous research groups have sought to implement such image guidance systems. One approach to image guidance in laparoscopic partial nephrectomy involved inserting fiducial markers on barbed needles directly into the kidney [71, 72]. The kidneys and fiducials were then imaged and segmented intraoperatively to enable registration by direct point-to-point correspondence between the fiducials in the segmented images and those same fiducials in the endoscopic video. While providing highly accurate, real-time guidance, these fiducial-based methods increase the risk and complexity of surgery by requiring foreign objects to be manually inserted into the kidney by the surgeon. Furthermore, the need for intraoperative imaging and segmentation represents a time-intensive interruption of the surgical workflow. Indeed, the robotic system is not compatible with intraoperative CT, and thus one would have to fully remove the robot to register the image set.

A less invasive approach to registration is fiducial-free manual registration. In manual registration, the surgeon is tasked with visually aligning 3D images or models to the surgical field. In [73] and [74], preoperative MR and CT images and 3D anatomical models were displayed alongside endoscopic video in the da Vinci's surgeon console, and surgeons could manually adjust the orientation of the images to match the endoscopic view. Ukimura et. al. [75] and Nakamura et. al. [76] presented augmented reality systems in which surgeons

manually aligned translucent 3D anatomical models directly overlaying the image feed from a laparoscopic endoscope. These studies found that surgeons benefited from having preoperative imaging information more readily available with respect to the live camera images. However, this approach increases cognitive burden on surgeons and provides no accuracy guarantees. Indeed, relying on human hand-eye coordination and spatial reasoning to perform registration makes accuracy highly dependent on an individual user's skill, resulting in low registration precision, as evidenced by large variations in registration accuracy from trial-to-trial in these studies.

To enhance precision and facilitate objective accuracy, others have sought to employ stereo endoscopes for instrument tracking and registration to patient anatomy. Su et. al. [77] proposed a multi-step CT-to-endoscope registration method where the segmented kidney surface was first manually aligned with the stereoscopic video. Surface-based video tracking techniques were then used to refine and stabilize the registration during system operation. Pratt et. al. [78] utilized an augmented endoscope overlay by first identifying a matching feature in both of the stereo images and the preoperative scans to align the translational degrees of freedom and then using a rolling-ball interface to manually align the rotational degrees of freedom. We direct the reader to [79] for a thorough overview of research aimed at using computer vision algorithms to automatically detect and track the da Vinci instruments in the stereo endoscope video. These vision-based approaches are limited by a requirement for persistent, direct line of sight between the endoscope camera and either the anatomical surface or the surgical instruments. During surgery, line of sight is often obstructed by blood, smoke, and other surgical tools. Furthermore, endoscope-based methods typically require accurate tracking of the endoscope position itself to localize tracked objects in the surgical field. Accurate endoscope tracking usually requires an external tracking system and a calibration process to determine the rigid transformation from the tracked frame to the camera frame, such as the method presented in [80]. Some researchers have sought to augment camera-based tracking methods by combining them with either geometric or kinematic

information to improve accuracy [81, 82, 83]. These results show promise and warrant further investigation, but have yet to fully address the above limitations of endoscope-based methods.

The kinematic information inherently available in the da Vinci surgical system represents a means of 3D localization that relies neither on intraoperative use of external trackers nor on processing endoscopic video. Previous research found that the da Vinci's active joints (which control motion of the laparoscopic instruments during operation) can be localized with sufficient accuracy for image guidance; however, the accuracy of the passive setup joints (used for gross manipulator positioning) was not suitable [84, 85, 86]. Kwartowitz et. al. [86] proposed to address this shortcoming by using a "hybrid" tracking scheme that combines two tracking modalities (specifically kinematic tracking and optical tracking) to more accurately track the multiple manipulators of the da Vinci in a common coordinate system. In this hybrid tracking scheme, the base frames of the active kinematic chains are registered to external, optically tracked frames attached to the base of the da Vinci. Thus, all base frames can be localized within the coordinate system of the optical tracker and the manipulator tips can then be kinematically tracked relative to their respective base frames. Fiducial localization experiments in [87] later validated the accuracy of hybrid tracking with the da Vinci for image guidance applications. In this paper, we implement this hybrid tracking approach as part of a new calibration method that also simultaneously estimates kinematic parameters of the da Vinci system.

Kinematic tracking of the da Vinci instruments has also shown particular promise in combination with "drop-in" ultrasound probes. In [88], registering the image frame of the ultrasound to the kinematic frames of the robot enabled the ultrasound plane to be displayed in the live endoscopic video. Researchers also combined automatic detection of the robot instruments in ultrasound images [89] with kinematic tracking to produce semi-autonomous ultrasound guidance that tracked instrument motions [90]. Later work in [91] demonstrated registration between kinematically tracked ultrasound and preoperative CT images for appli-

cation to partial nephrectomy. The feasibility of this ultrasound-based registration technique in the context of the operating room is, however, inherently coupled to the accuracy of intra-operative segmentation of the ultrasound images, and represents a skill- and time-intensive addition to the surgical workflow. As an alternative, the touch-based method examined in this work uses the da Vinci's kinematically tracked instruments directly to digitize anatomical surfaces to enable registration.

The idea of a touch-based registration for image guidance with the da Vinci system was first introduced by Ong et. al. [69]. During a partial nephrectomy case, the instrument tool tip was lightly traced over the kidney surface while recording the robotic joint values; the data was processed postoperatively to generate a sparse set of surface points that were used for a standard surface-based registration. The concept showed qualitative merit; however, the authors noted they were unable to perform quantitative analysis of the touch-based method due to the unavailability of a ground truth comparison during the human trial. Building upon this concept, we have further assessed surface-based registration with the da Vinci using rigid phantoms [92]; however, thorough analysis of registration error for this touch-based method using anatomically accurate phantoms has thus far remained unstudied. In this paper we take essential steps toward practical and accurate deployment of this touch-based registration concept by presenting a system that is suitable for deployment in a real-world operating room and accomplishes registration in real time. We also rigorously evaluate the accuracy of touch-based registration on anatomically accurate soft-tissue phantom models, and demonstrate its ability to improve the localization accuracy of an experienced surgeon.

III.4 System Overview

III.4.1 Preoperative System Setup and Calibration

Preoperative calibration of the da Vinci *Si* system is necessary to achieve sufficient kinematic tracking accuracy to enable our touch-based registration. Figure III.2 shows a clinical da Vinci *Si* deployed for preoperative calibration, which takes place as the da Vinci system

is draped prior to surgery. Additively manufactured reference frames designed to interface with the da Vinci system are clamped rigidly to the distal ends of the setup arms (Fig. III.2, upper right). These reference frames are equipped with reflective optical tracking markers. To maintain the sterile field, the reference frames are first clamped without reflective spheres before deploying the sterile drapes. After draping the robot, sterile, disposable, commercially available spheres are attached to mounting posts through the sterile plastic drapes. This process ensures a sterile barrier between the clamping system and the sterile surgical environment.

As shown in Fig. III.2 (lower right), the da Vinci instruments grasp sterile, optically tracked calibration tools. Each calibration tool is previously pivot-calibrated so that the position of the interface with the instrument tip is accurately known relative to the optical markers. This enables measurement of the instrument position relative to the optically tracked reference frames at the base of each serial chain. Our system uses a Polaris Spectra (Northern Digital Inc., Waterloo, Ontario, Canada) optical tracking system, which is currently available for use in many operating rooms, including any operating room at our institution. The Polaris system has a reported tracking accuracy of 0.25 mm, and for this work, we consider measurements with the optical tracker to be ground truth [93].

To collect calibration data prior to surgery, a robot operator simply moves the calibration tools throughout the robot workspace while recording data. In our current implementation, the operator momentarily pauses at discrete locations to ensure synchronization of optical tracking and robot encoder data streams. This is necessary only because we did not have direct access into the robot software to enable synchronization between the data streams of the optical tracker and robot. In future clinical implementations, the markers can simply be waved in front of the optical tracking system to collect calibration data. This data collection process is repeated for each da Vinci manipulator and each instrument to be used during surgery.

Our system employs a hybrid tracking technique [86] for calibration that enables the

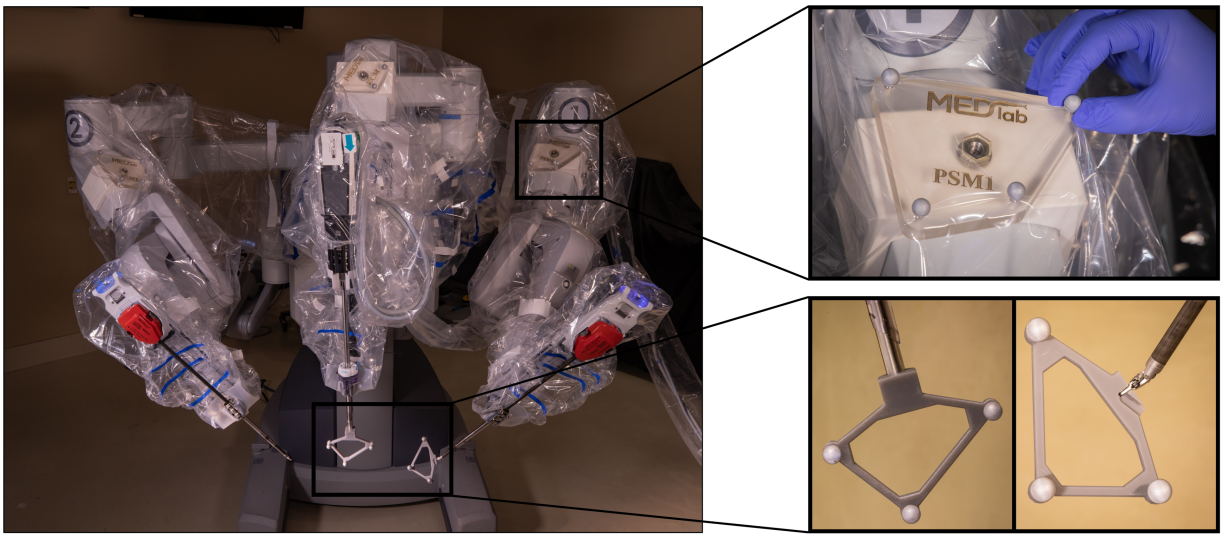

Figure III.2: Hybrid tracking implemented with the da Vinci *Si* in the operating room. Optically tracked markers (top right) are rigidly clamped to the base of each manipulator, and sterile tracking spheres are attached to the markers over the robot drapes ensuring sterility. Calibration is achieved by gripping sterile calibration objects (bottom right) in the manipulators (or pressing them onto the endoscope) and waving them in front of the tracker preoperatively.

da Vinci's manipulators to be kinematically tracked relative to external, optically tracked reference frames (rather than the internal base frames of the da Vinci system). Using hybrid tracking bypasses the comparatively inaccurate setup joints of the da Vinci system, shortening the effective kinematic chain and improving tracking accuracy beyond the inherent capabilities of the da Vinci system. Our calibration process also simultaneously calibrates the parameters of the kinematic model using standard techniques [94, 95, 96]. The result of calibration is that each robotic instrument can be accurately tracked with respect to the location of the reference frames attached at the base of the active serial chain.

III.4.2 Touch-Based Registration

Our touch-based registration method aligns two sets of data: a densely sampled point set describing the organ surface in image space and a sparsely sampled point set of surface data describing the organ surface in physical space. The dense image space point set is obtained preoperatively from volumetric imaging. For the experiments presented in this paper, the

kidney surface was manually segmented from CT images using 3D Slicer, an open-source medical image computing and visualization software platform [97]. In the future, however, when an image guidance system like ours is developed into a commercial product, it is likely that manual segmentation would be replaced by an automatic segmentation algorithm. Any existing or future segmentation algorithm would be straightforward to incorporate into the framework described in this paper, since our system assumes only the existence of a segmentation without regard for how the segmentation was accomplished.

The physical space point set is obtained intraoperatively by lightly tracing the surface of the patient's organ with the tip of the da Vinci's instrument. We track the instrument's tip position in physical space during this process using the previously calibrated kinematics. Surface tracing is quick and non-disruptive to surgical workflow: acquiring a sufficient number of surface points for accurate registration requires only about 30 seconds. After tracing, the data are automatically downsampled to exclude data points within 2 mm of neighboring points to eliminate variations in point cloud density caused by variable tracing speed. This results in a set of points in physical space that lie on the surface of the patient's kidney.

Previous work concluded that the physical-space data used for surface-based registration should include at least 28% of the anterior surface area of the kidney to ensure accurate registration [98]. Therefore, once surface tracing is complete, our system automatically analyzes the tracing data to verify that the tracing covers a sufficient area. Our system determines the surface area corresponding to a tracing by constructing a surface mesh from the tracing data using the ball-pivoting surface reconstruction algorithm [99] (illustrated in Fig. III.3). The area of the reconstructed surface is compared to the kidney's surface area, which is determined from the preoperative CT images.

Registration between the image space point set with the physical space point set is computed using the globally optimal iterative closest point (GoICP) algorithm [100]. GoICP does not require user initialization and as such is not subject to suboptimal initialization concerns associated with standard ICP algorithms. The resulting registration between the

image space and the physical space relates knowledge of the patient's anatomy present in the preoperative images to the current position of the robot with respect to the patient.

III.4.3 Real-Time Data Streaming and Visualization

Using the computed registration, we display the position of anatomical structures segmented from preoperative imaging to the surgeon in real time directly in the da Vinci surgeon console (see Fig. III.1).

We built our image guidance system as a submodule of 3D Slicer, an open-source medical image computing and visualization platform that enables patient image segmentation, preoperative planning, and real-time model rendering for image guidance [97]. Our system interfaces with the clinical da Vinci *Si* application programming interface (API) [101] through a data acquisition module built with the open-source Plus Toolkit [102] that streams kinematic data output by the API to 3D Slicer using the standardized OpenIGTLink messaging protocol [103]. This enables the endoscope camera view and graphical models of the da Vinci's manipulators in the image guidance display to track the movement of the physical instruments in real time. Our image guidance (see Fig. III.1) is displayed directly in the da Vinci surgeon console through the console's TilePro interface.

III.5 System Validation Experiments

We first evaluate the efficacy of our calibration method to improve the overall kinematic accuracy of the da Vinci robot. We then evaluate the accuracy of our touch-based registration method.

III.5.1 Calibration Accuracy

We wish to determine the number of measurements that must be collected during preoperative setup to ensure good calibration results. In the context of robot calibration, this number is generally difficult to predict, as it varies from system to system and also depends on the measurement method used [104]. We performed a series of trials to determine the

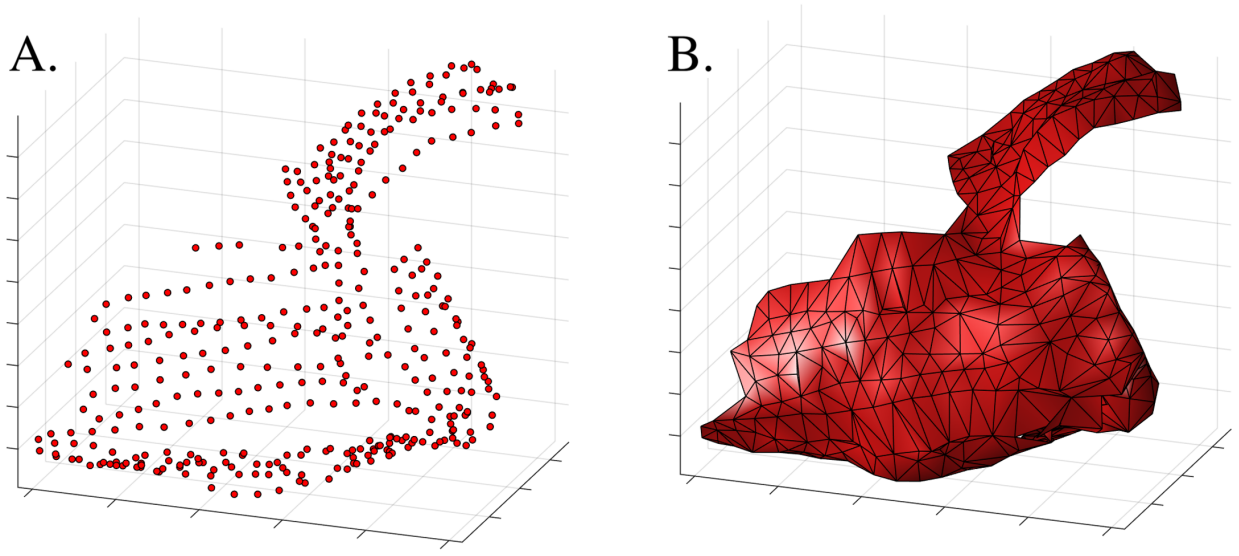

Figure III.3: Surface reconstruction from surface tracing data. A. Original point set from an example robotic instrument tracing. B. Reconstructed surface for surface area computation to ensure adequate model coverage.

relationship between tracking accuracy and the number of measurements used in calibration, as described below.

For our touch-based application, the da Vinci instrument tip serves as the localizer. Given that surface-based registration relies only on discrete points of position data, only the positional (not rotational) accuracy of the localizer needs to be considered. Therefore, the accuracy of our system can be quantified by the fiducial localization error (FLE) of the da Vinci instruments, *i.e.* the distance between the model-predicted tip location and the true tip location:

$$\text{FLE} = \left\| \boldsymbol{p}_{\text{model}}^{\text{robot}} - \boldsymbol{p}_{\text{true}}^{\text{robot}} \right\|. \tag{III.1}$$

In practice, the FLE cannot be directly measured because our model-predicted position is measured in a different coordinate frame from our "true" position (as measured by the optical tracker). However, it is possible to indirectly estimate the expected value of the FLE from these data, as described below. The transformation between the two coordinate frames (the robot and the optical tracker) can be estimated from a standard, rigid, point-based

registration between the model-predicted positions and the true measured positions [105]. The error associated with such a registration can be quantified by the fiducial registration error (FRE), which is the root-mean-square error in the alignment of the registered points. Performing numerous registrations using different sets of point samples provides a good estimate for the expected value of the FRE for registrations between the two frames. The expected value of the FRE can be used to estimate the expected value of the FLE, according to the following relationship derived in [105]:

$$\langle \mathrm{FLE}^2 \rangle = \frac{\langle \mathrm{FRE}^2 \rangle}{(1 - 2/N)}, \tag{III.2}$$

where N is the number of points used in the registration and the angle bracket operator denotes the expected value of a random variable. This formulation relies on standard assumptions that the components of FRE are independent, isotropic, 3D normal random variables.

Our evaluation data set comprised 130 calibration measurements, collected at distinct poses representing a sparse sampling of the entire da Vinci *Si* active workspace. Each calibration measurement consists of a set of robot joint values and a corresponding Cartesian position, measured in the optical tracker's workspace. All data was collected using the da Vinci's EndoWrist Large Needle Driver instrument.

To determine the relationship between the model-predicted position accuracy and the number of data points used in model calibration, we performed a Monte Carlo cross-validation analysis of the evaluation data set. Each iteration of the cross-validation was performed as follows:

- A number $M \in \{10, 15, 20, \ldots, 95, 100\}$ of "training points" were selected uniformly at random from the complete set of 130 points.
- The kinematic model was calibrated using the training points.
- $K = 30$ "validation points" were selected uniformly at random from the remaining

$130 - M$ points.

- A number $N \in \{5, 6, 7, \ldots, 19, 20\}$ of "registration points" were selected uniformly at random from the validation points. This process was repeated 1000 times for each value of N, resulting in a total of $16,000$ distinct sets of registration points per iteration.

- Using each set of registration points, a rigid point-based registration between the (calibrated) model-predicted positions and the measured "true" positions was performed.

- The mean value of FLE for the calibrated system was computed from the average FRE of each registration according to Eq. (III.2).

This process was repeated a total of 1000 times for each value of M. Figure III.4 shows the results of this analysis, which indicates that using more than 60 data points to compute the hybrid tracking calibration offers only marginal improvements to localization accuracy.

Figure III.5 shows the accuracy improvement of the calibrated da Vinci model compared to the nominal model from [86]. The mean and standard deviation of the calibrated system's FLE are 0.95 mm and 0.14 mm, respectively, representing a 34% reduction in mean localization error. While no well-defined localization accuracy threshold exists for image guidance applications, it is clear that increased accuracy is always desired. Our calibrated system accuracy is comparable to prior methods used to track the absolute position of the da Vinci's instrument tips (1.31 mm in [85] and 1.39/1.95 mm for PSM1/PSM2 in [86]).

We wish to emphasize that the accuracy values reported here reflect only the deviation between the model-predicted position of a robot manipulator and the measured position (i.e. where the robot "thinks" the manipulator is versus where it truly is). These accuracy results do not describe the accuracy with which a surgeon can direct the da Vinci manipulators during teleoperation (i.e. where the surgeon wants the manipulator to be versus where it truly is). While touch-based image guidance relies on a highly accurate model-predicted position, teleoperation with visual feedback and a human in the loop does not.

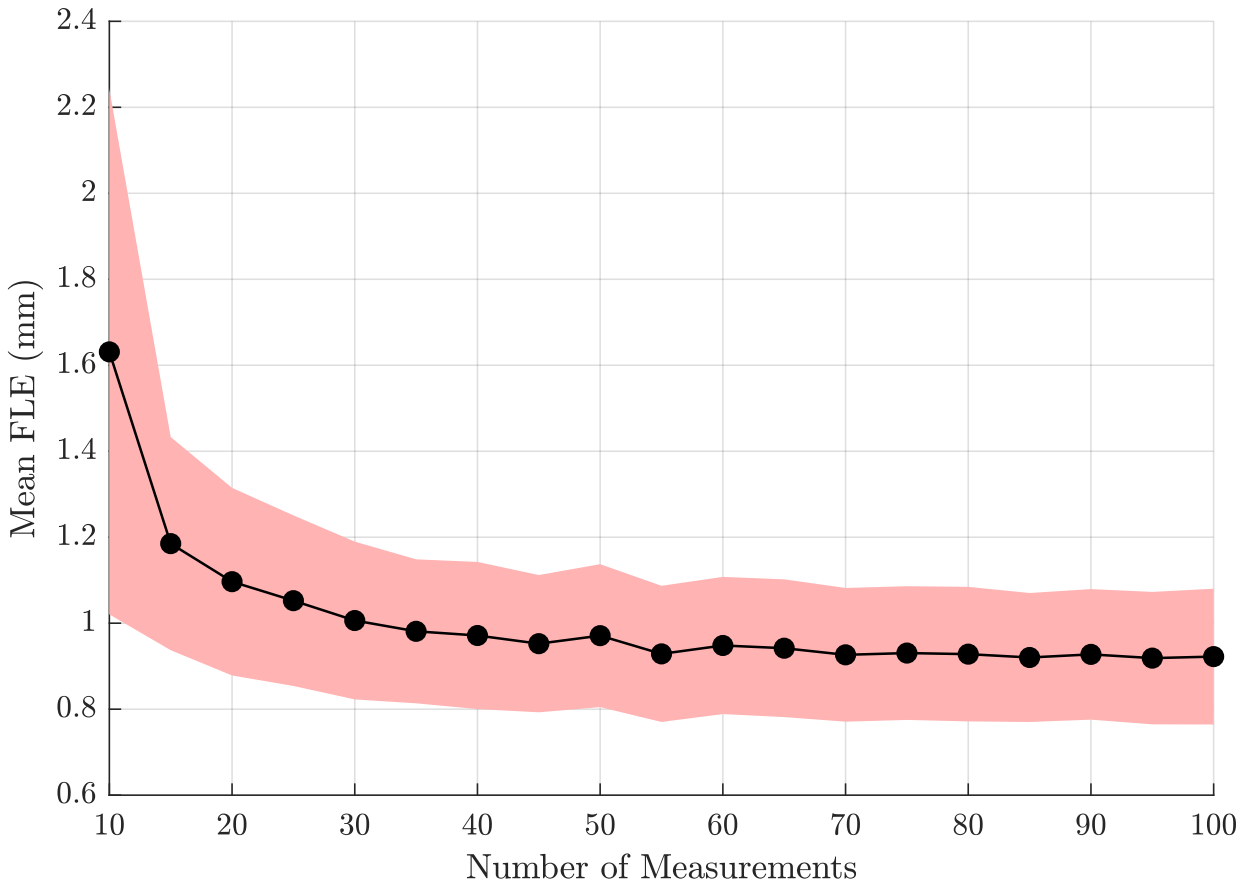

Figure III.4: Fiducial localization error (FLE) of the da Vinci *Si* vs. the number of measurements used for calibration of the hybrid tracking model. The red area indicates the standard deviation for each respective trial. Only marginal improvements to accuracy can be seen past $M = 60$.

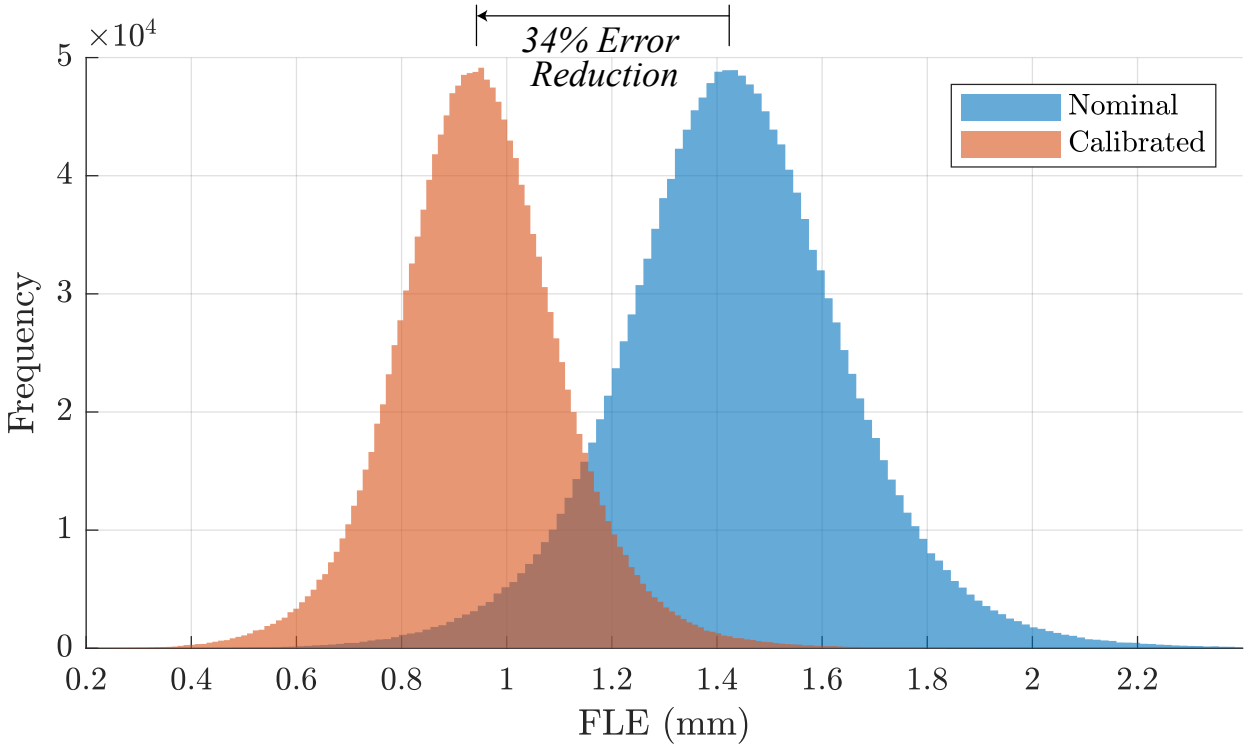

Figure III.5: Distribution of RMS errors between the model-predicted robot tip position using hybrid tracking and the ground truth, optically tracked tip position. A significant decrease in error is seen when using our calibration method (red) over using the nominal robot parameters (blue). Results are for 1000 calibration trials with $M = 60$ measurements per trial.

III.5.2 Registration Accuracy

We evaluated the accuracy of our touch-based registration method in a series of experiments using a commercially available synthetic kidney model (SynDaver Labs, Tampa, FL, USA) that accurately reflects the geometry and mechanical soft-tissue properties of a human kidney. For our experiments, the model was fixed to an optically tracked platform, as shown in Fig. III.6.

Prior to experiments, the entire platform was CT scanned using an xCAT ENT Scanner (Xoran Technologies LLC, Ann Arbor, MI, USA) using a section thickness of 0.3 mm. The kidney surface as well as the optical tracking markers were manually segmented from the CT images using 3D Slicer [97]. The kidney surface segmentation was used to produce the required image space point set for registration. The segmentation of the optical tracking markers was used to compute the ground truth pose of the kidney model relative to the makers, which were optically tracked in the operating room.

To acquire data in physical space, an experienced urologic surgeon thoroughly traced the entire anterior surface of the kidney phantom using a Large Needle Driver instrument in a calibrated da Vinci *Si* while our system recorded tool tip position data. The resulting data set comprised 1241 evenly spaced position measurements. From this large data set, we randomly generated 700 smaller continuous tracing intervals. The size of each sub-interval was randomly chosen from a discrete, uniform distribution to be between 200 and 400 position measurements. All of the 700 tracings met or exceeded the minimum surface area threshold.

For each of the 700 tracings, we performed registration using GoICP, mapping the segmented kidney model into the robot's workspace. We then compared the registration to the ground truth pose of the kidney phantom, as measured using the optically tracked experiment platform. To evaluate the quality of each computed registration, we compared the vertex positions of the registered kidney model to the corresponding vertex positions in the tracked, ground truth model. The target registration error (TRE) at each vertex of the registered model was computed as the distance between that vertex and the corresponding

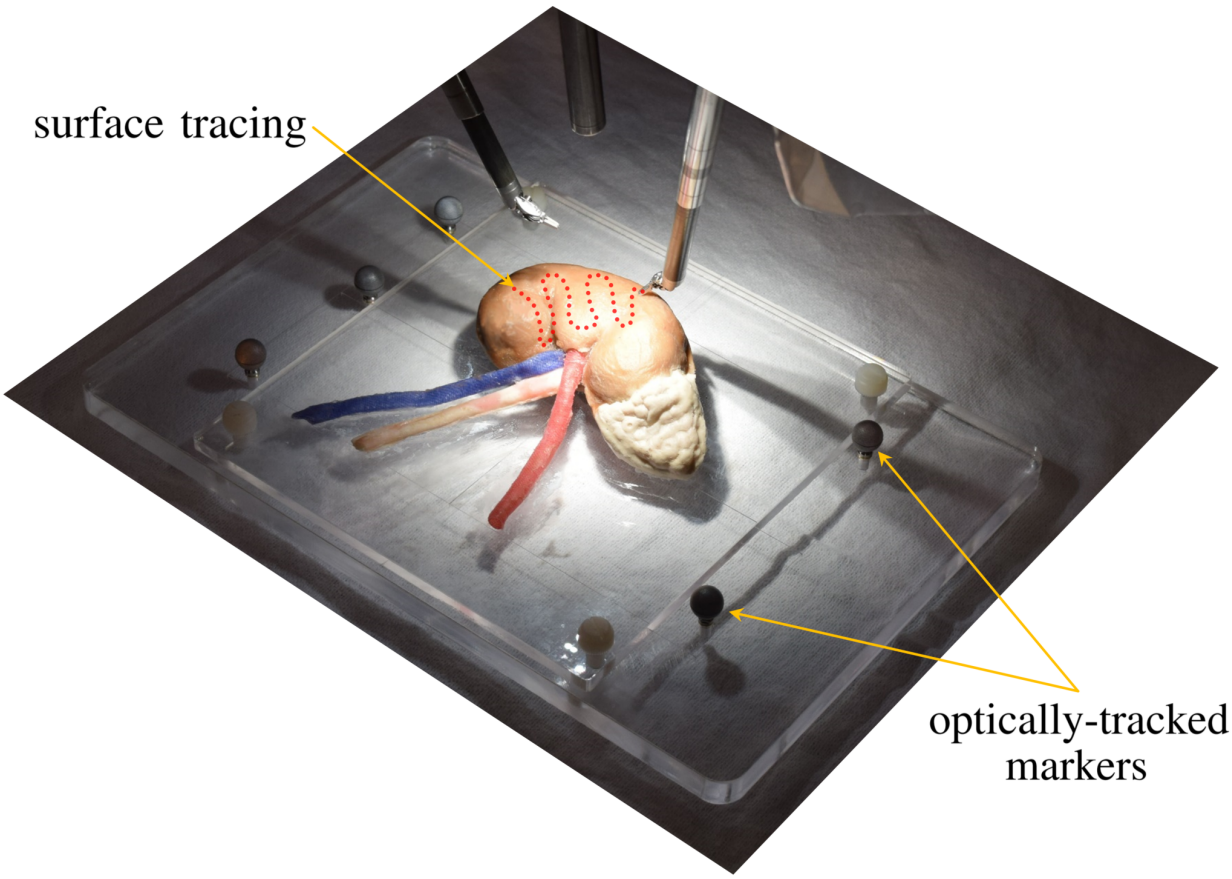

Figure III.6: Optically tracked phantom platform used for evaluating registration accuracy. Surface data for registration is acquired by tracing the phantom surface (illustrated as red dots). The location of the phantom relative to the tracked platform is known, enabling evaluation of our touch-based registration technique.

vertex of the ground truth model.

Figure III.7 shows an example registration with the TRE visualized as a heat map over the entire surface. The red lines shown in the figure represent the tracing (comprising 276 points in this example) of the physical kidney surface used for registration. In the region of the kidney where surface data was collected with the robotic instrument tip, TRE is approximately 2 mm while RMS TRE over the entire kidney surface is 2.75 mm. The TRE tends to increase as the distance from the data collection area increases, as should be expected.

To evaluate the overall consistency and reliability of our registration technique, we com-

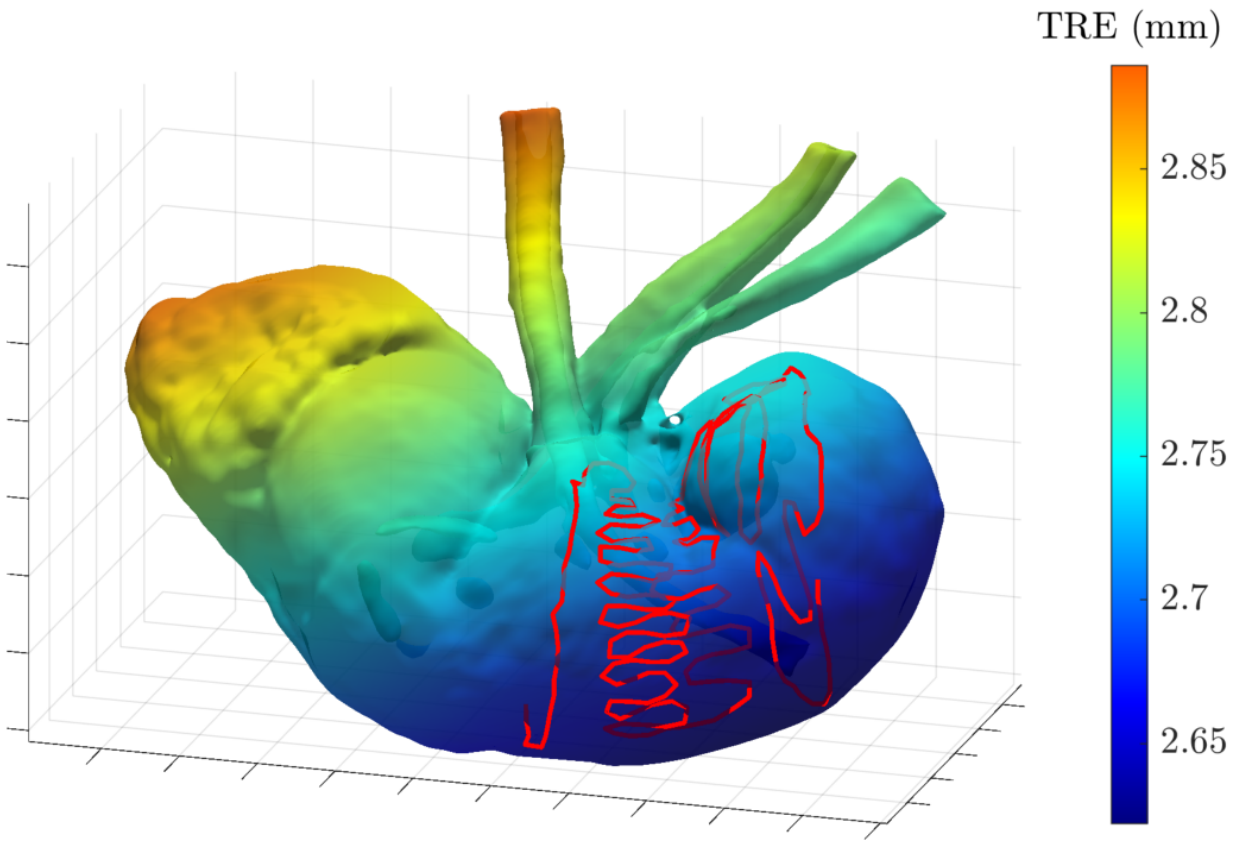

Figure III.7: An example registration result using our touch-based registration technique. The heat map shows the TRE over the entire model surface. Red points represent the surface tracing used for registration.

puted the RMS TRE over the entire kidney surface for all 700 tracings, as shown in Fig. III.8. The average RMS TRE over all of the 700 registrations was 3.69 mm with standard deviation 0.61 mm. Note that while we performed registration using only a small number (200–400) of data points collected on the anterior kidney surface, we have reported RMS TRE over the entire kidney surface (at ∼175,000 mesh vertices). As opposed to considering TRE at a few points in the vicinity of the surface tracings, these results more realistically depict errors that can be expected over the surgical work volume when using touch-based registration.

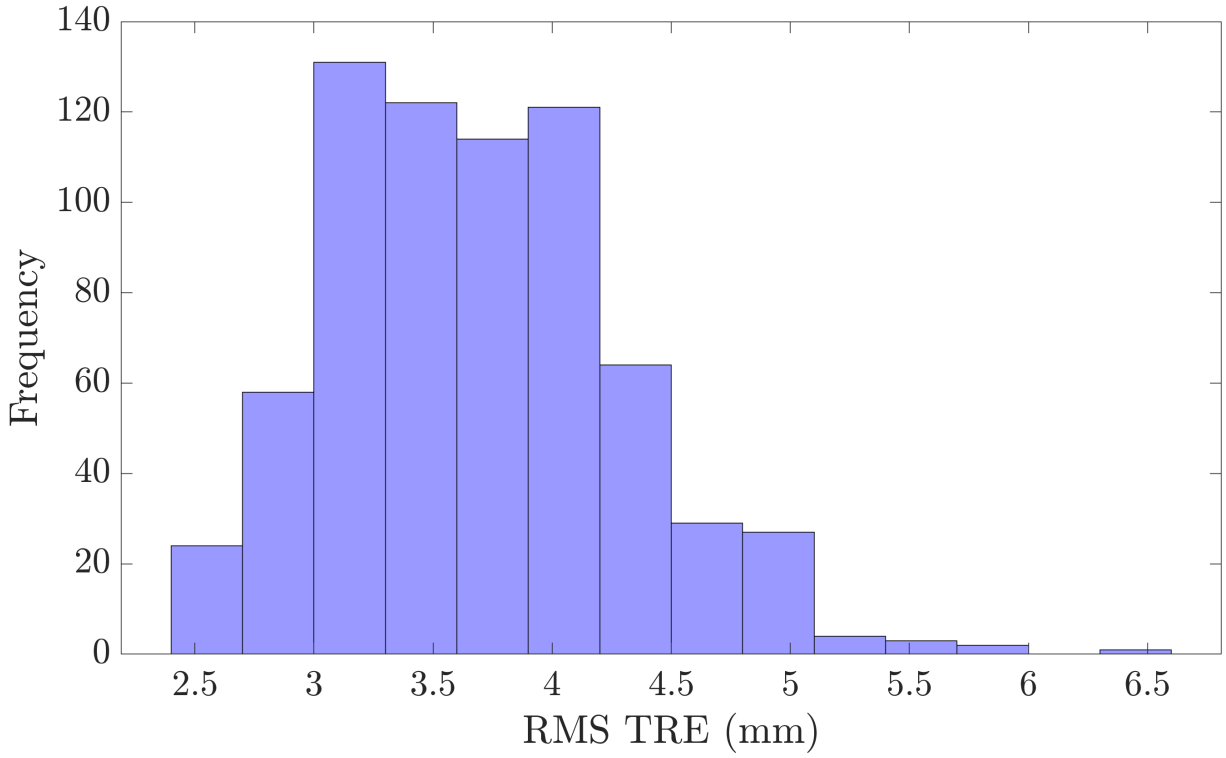

Figure III.8: Distribution of RMS TRE (computed over the entire kidney surface) for 700 trials of our touch-based registration method. In each trial, tracings covered at least 28% of the anterior kidney surface.

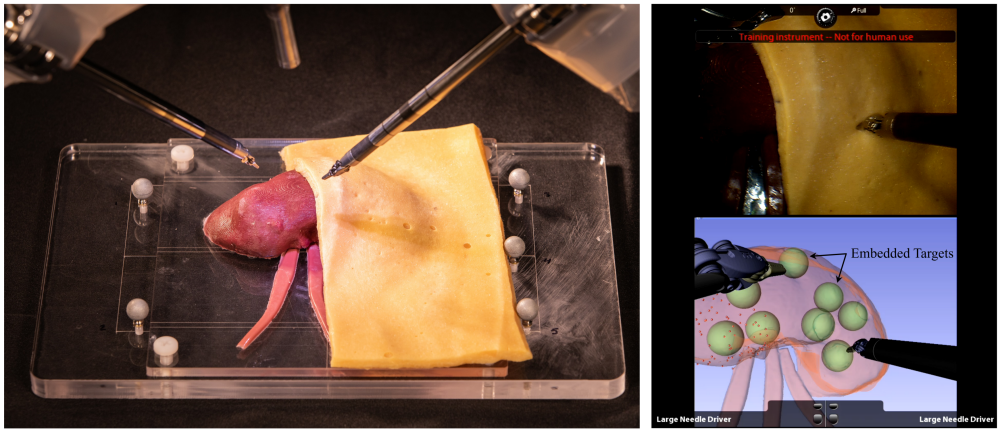

Figure III.9: Experimental setup to measure a surgeon's accuracy in localizing subsurface features with and without our image guidance system. Targets embedded in a phantom kidney model were localized using our system with a clinical da Vinci *Si*. The display presented to the surgeon during the procedure is shown in the right column.

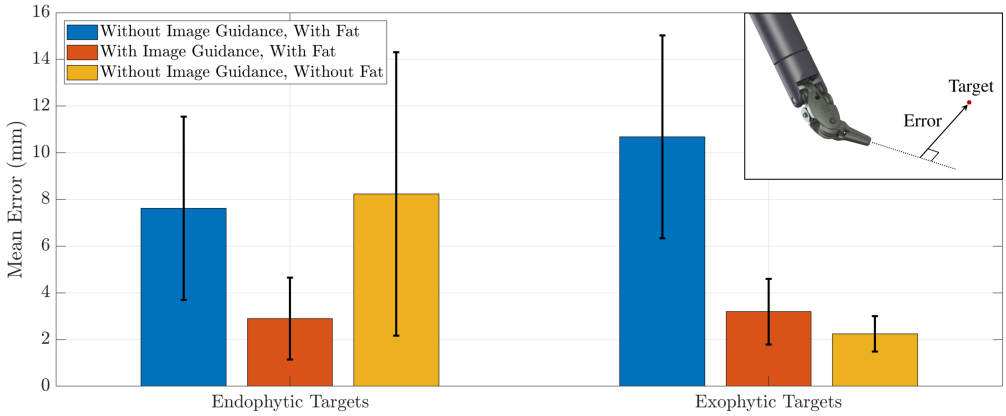

Figure III.10: Error in localizing embedded endophytic and exophytic targets in a phantom kidney model. Localization was performed with and without image guidance while fat partially obscured the kidney surface (including all exophytic targets). Localization was then performed without image guidance and without the fat layer (allowing direct visualization of the full kidney surface, including exophytic targets). Results indicate that our system increases surgeon accuracy in localizing subsurface features ($p \ll 0.001$).

III.6 Image Guidance Phantom Experiment

To demonstrate the utility of our system in the operating room, we performed a phantom experiment comparing the surgeon's accuracy in localizing subsurface features both with and without the image guidance provided by our system. Figure III.9 shows the setup for this experiment.

A challenge of many robotic surgical procedures is the localization of subsurface anatomy, making it difficult for the surgeon to know where to cut to remove lesions or avoid vessels. This is especially true in robot-assisted partial nephrectomy. During removal of perirenal fat surrounding the patient's kidney, the surgeon must identify the locations of the renal artery, the renal vein, the ureter, and the tumor. All of these features are hidden beneath the fat layer. The fat must be carefully dissected, and the anatomical features must be uncovered while avoiding unnecessary damage which could result in blood loss or positive tumor margins.

We manufactured a soft, realistic silicone kidney phantom based on patient CT imaging. Eight acrylic spheres approximately 12 mm in diameter were set in the silicone material as it cured to serve as localization targets for experiments. Four targets were completely endophytic while the remaining 4 targets were at least partially exophytic. The model was fixed to the same optically tracked platform used in our registration experiments. The entire platform was CT scanned and segmented as before in Sec. III.5.2. Optical tracking of the phantom platform was used solely to determine the ground truth positions of the embedded targets in the operating room to enable post hoc analysis of the surgeon's localization accuracy.

During the experiment, the phantom was partially covered in a 10 mm thick layer of SynDaver synthetic fat. The fat completely covered all exophytic targets such that none of the localization targets were directly visible to the participating surgeon. Approximately 40% of the anterior surface of the phantom was left uncovered to simulate the results of fat dissection required at the beginning of a partial nephrectomy procedure.

Prior to the experiment, the participating surgeon reviewed CT images of the phantom to develop a "mental map" of the locations of subsurface targets. The surgeon was allowed to reference the CT images throughout each phase of the experiment.

In the first phase of the experiment, the surgeon attempted to localize the subsurface targets based solely on his interpretation of the CT images. To localize a target, the surgeon

was instructed to point (using the calibrated da Vinci instrument) to the perceived location of the center of each of the 8 targets. Each time the surgeon pointed to a target, our system recorded the transformation from the instrument tip to the system's world coordinate frame to use for analysis. The surgeon repeated this pointing task 5 times for a total of 40 measurements.

In the next phase of the experiment, the surgeon repeated the subsurface localization task using our image guidance system. The surgeon first lightly traced the exposed portion of the kidney surface to collect surface data for our touch-based registration protocol. With the image guidance enabled by the registration, the surgeon repeated the above process of identifying target locations with the robotic instrument.

The final phase of the experiment served to establish a baseline accuracy for the target localization task. The image guidance was disabled, and the fat layer was completely removed from the phantom. With direct visualization of the entire kidney surface through the da Vinci's endoscope, the surgeon then repeated the target localization process as before. Note that with direct visualization of the kidney surface, 4 of the target spheres were at least partially visible while the remaining 4 targets were completely concealed beneath the surface.

For all phases of the experiment, localization accuracy was evaluated by comparing target locations identified by the surgeon to the corresponding optically tracked, ground truth locations. For a particular surgeon-identified location and ground truth pair, the localization error was taken as the minimum distance between the Z axis extracted from the end effector tip transform (the pointing direction of the instrument tip) and the ground truth target position (see the inset in Fig. III.10). Figure III.10 summarizes the localization accuracy results for each phase of the experiment.

Performing a pairwise t test on the set of all errors with image guidance and the set of all errors without image guidance showed a significant reduction in error. Mean error was reduced by 67% (from 9.2 mm to 3.0 mm) by using image guidance ($p \ll 0.001$).

For brevity, references to measurements made "with image guidance" or "without image

guidance" in this discussion will refer specifically to those measurements made with fat partially obscuring the kidney surface. The term "direct visualization" refers to measurements made with all fat removed from the kidney surface (and no image guidance).

The measurements made with direct visualization provide helpful context for interpreting the localization accuracy results with and without image guidance. Direct visualization did not improve the surgeon's localization accuracy of endophytic tumors when compared to the scenario without image guidance. This result indicates that increasing the visible surface area of the kidney did not help the surgeon form a more accurate mental registration between the CT images and the surgical scene. Using image guidance, on the other hand, enabled a substantial improvement of localization accuracy for endophytic targets when compared to both the scenario without image guidance and that with direct visualization. Taken together, these results demonstrate the utility of our image guidance system for enabling accurate localization of subsurface features, specifically indicating that image guidance improved the surgeon's localization ability beyond natural human ability.

With regards to the exophytic targets, direct visualization unsurprisingly resulted in substantially improved localization accuracy when compared to localization without image guidance (when the exophytic targets were completely obscured by fat cover), but direct visualization offered only slightly better accuracy than using image guidance. It is crucial to note, however, that direct visualization of exophytic tumors is very unlikely in a true clinical scenario. Surgeons rarely remove fat covering a tumor during partial nephrectomy for two reasons: (i) the fat provides a safe grasping point for manipulating and removing the tumor, and (ii) dissecting fat attached directly to the tumor dramatically increases the risk of unintentionally puncturing the tumor. Thus, image guidance was nearly as accurate as direct visualization while potentially being much safer.

While these results show great promise for our image guidance system, the current study was limited to one surgeon subject. Future work will be needed to explore whether the ability to accurately trace the kidney surface or to accurately identify subsurface features

varies from subject to subject. Anecdotally, we have not observed large differences in these skills among either engineer or physician co-authors of this paper, but quantification of this anecdotal observation will be necessary in the future.

III.7 Conclusion and Future Work

In this paper, we presented a practical and easily implemented image guidance system for the da Vinci family of robotic systems. Specifically, we proposed and tested a new method of accurately estimating required tracking parameters through calibration, achieving submillimetric absolute kinematic tracking accuracy for the first time with any da Vinci robot. We then presented the first quantitative accuracy evaluation of touch-based registration with the da Vinci, using an anatomically accurate SynDaver kidney model. We presented a system that incorporates these advancements to bring this concept toward real-world use. Finally, we demonstrated the utility of our system in the operating room in the first validation of touch-based image guidance to improve a surgeon's ability during a subsurface target localization experiment.

The results of this work indicate a promising application for robotic partial nephrectomy which may increase the adoption of this underutilized alternative to total kidney removal; however, several significant challenges remain to be addressed before touch-based image guidance with the da Vinci can be fully realized in the operating room. The *ex vivo* experiments in this work provide a valuable proof of concept, but moving forward, it is crucial to perform *in vivo* evaluation of our image guidance system. In particular, we believe it may be useful to examine the effect of external forces applied to the da Vinci manipulators by the patient body wall and the insufflation system on kinematic tracking accuracy. Additionally, as prior works have noted, factors including patient positioning [106, 107], peritoneal insufflation [108], arterial clamping [109], and kidney dissection [69], potentially cause organ deformation that can negatively affect registration accuracy when using preoperative images. Future work will be needed to address the effects of organ deformation that occurs throughout the

surgical procedure. Substantial progress on these topics has been made (*e.g.*, [69, 70, 110]) and can potentially be incorporated into our system in the future, particularly when accurate algorithms become computationally efficient enough for real-time use in a system like ours. Nonetheless, our results show that even rigid registration alone improves the ability of a surgeon to localize unseen subsurface objects in partial nephrectomy. Localizing these objects with confidence before cutting may, in the future, help to shift clinical decision making so that many more patients can receive the lifelong benefits of partial nephrectomy.

III.8 Postface

The Vanderbilt Institutional Review Board recently approved initial human studies for evaluating the image guidance system. These studies are organized as "bystander studies," involving two surgeons—an operating surgeon and a bystander surgeon—to enable evaluation of the image guidance system without influencing surgical decision-making. The operating surgeon will perform all surgical tasks without access to the image guidance. At specific points throughout the procedure, the bystander surgeon will briefly take control of the surgical robot in order to make evaluative measurements of the image guidance accuracy; however, the bystander surgeon will not attempt any surgical tasks.

CHAPTER IV

Intraoperative Ultrasound-Based Image Guidance for Robot-Assisted Partial Nephrectomy: A New Surface-Based Implementation and Initial Clinical Evaluation

IV.1 Introduction

As discussed in the previous chapter, image guidance is most needed during two critical steps of the partial nephrectomy procedure: first, during the identification of the delicate renal vasculature (which must be dissected from encapsulating fat in order to be clamped prior to cutting the kidney); and again, when identifying the margins around the tumor (which is at least partially endophytic). Given that tumor removal is the ultimate surgical goal of partial nephrectomy, the image guidance systems proposed by the literature for partial nephrectomy to date (including the touch-based system introduced in Chapter III) have focused almost exclusively on assisting in tumor resection. Despite this fact, however, vessel identification represents the most technically challenging and time-intensive aspect of a typical partial nephrectomy. Expanding image guidance capabilities to be able to aid initial vessel identification and dissection promises to significantly reduce the overall length and complexity of surgery.

Safety considerations dictate that dissection of perirenal fat to expose the kidney cannot begin until after the renal vasculature has been identified [32, 33]. The presence of perirenal fat visually obscures most of the critical anatomy around the surgical site, severely limiting the amount of anatomical information that can be discerned and used as a basis for registration prior to fat dissection. In particular, inability to directly visualize renal parenchyma precludes many of the previously discussed surface-based registration methods.

Intraoperative ultrasound imaging represents a potential means to acquire anatomical surface information *without* disturbing surrounding tissue or first removing perirenal fat.

Currently, intraoperative ultrasound sees widespread clinical use in numerous surgical specialties because it is inexpensive, safe (*i.e.* nonradiative), fast, and compact compared to using other imaging modalities, such as CT and MR, intraoperatively. In partial nephrectomy specifically, laparoscopic ultrasound is commonly used to assist in exploring anatomy around the surgical site and identifying tumor margins below the kidney surface [32, 33]. Unlike other imaging modalities, however, ultrasound is a reflective imaging modality, and as such, the image quality of an anatomical target will vary depending on factors such as the direction from which the beam approaches the target and the coupling between the ultrasound transducer and the tissue surface [111]. Controlling these factors in order to obtain clear and accurate images relies heavily on the the surgeon user's skill in manipulating ultrasound. Furthermore, the surgeon must be able to simultaneously interpret live 2D cross-sectional ultrasound video to discern useful 3D anatomical information.

Use of intraoperative ultrasound to acquire anatomical surface information could circumvent the obstacles posed by impeded access to target surfaces while the ability to register intraoperative ultrasound images to preoperative volumetric images also promises to alleviate the user burden of ultrasound imaging by decoupling the processes of image acquisition and image interpretation. Achieving 3D image registration with ultrasound requires some method of relating 2D image planes to a spatial reference frame containing the target anatomy. While some advanced ultrasound devices can generate 3D image volumes by electronically steering the direction of acoustic waves emitted by the ultrasound [112], a simpler and more common approach has been to track the 3D location of an ultrasound probe by external means. The method of generating volumetric image data from ultrasound is often referred to as "freehand 3D ultrasound." Numerous approaches to 3D image reconstruction from freehand 3D ultrasound have been examined in the literature; however, these approaches are often limited by various issues pertaining to computational intensity, image artifacts, low voxel resolution, or sensitivity to image acquisition orientation and trajectory (see References [113] and [114] for a review of these approaches). Furthermore, these approaches do not address the fundamental

problem of establishing a spatial relationship between the volumetric image and the surgical workspace. This work will focus instead on image registration between externally tracked, intraoperative ultrasound and preoperative volumetric images. Various approaches to this type of ultrasound-based image guidance have been widely demonstrated in the literature, including examples in orthopedic surgery [115, 116, 117], neurologic surgery [118], hepatic surgery [119, 120], and prostate surgery [121, 122]. In the case of robot-assisted surgery, the inherent kinematic tracking capabilities of the robot system provide a convenient means for tracking a robotically manipulated ultrasound probe, as several papers have demonstrated [88, 91, 122]. Reference [91] specifically suggested applying ultrasound-based image guidance to vessel identification in partial nephrectomy and then demonstrated registration between robotically tracked ultrasound and CT images in phantoms.

This dissertation addresses two meaningful gaps in the literature related to ultrasound-based image guidance. The first gap pertains to the method of extracting surface data for registration from ultrasound images. In order to achieve robust registration, existing literature has focused on identifying either rigid, geometrically distinct landmarks (*e.g.*, bones) or highly vascular structures (*e.g.*, the brain and the liver) to ensure accurate correspondence with preoperative images. For application to partial nephrectomy, the literature has suggested similarly using renal vessels as registration targets [91]; however, other research has shown that the renal vasculature is prone to significant deformation resulting from differences in patient positioning during preoperative imaging versus during surgery whereas the kidney parenchyma remains relatively rigid (though experiencing bulk translation and rotation) [106, 107]. This chapter introduces a new approach to ultrasound-based image registration that uses intraoperative points derived directly from the kidney surface while still capturing adequate feature variation to ensure image correspondence. The image-guidance system presented in Chapter III was extended to enable this new approach using freehand 3D ultrasound with a clinical da Vinci Xi surgical robot. This chapter presents an analysis of the accuracy of the ultrasound-based registration method. Using the extended image guidance

system, this chapter next addresses a second gap in the literature by evaluating for the first time the clinical utility of ultrasound-based image guidance in the context of robotic partial nephrectomy. This chapter presents a series of experiments that compares the performance of surgeons of various skill levels when using freehand ultrasound versus ultrasound-based image guidance to perform simulated surgical tasks related to partial nephrectomy. The results demonstrate the ability of image guidance to significantly improve several markers of surgical quality when used by less experienced surgeons.

IV.2 Ultrasound-Based Image Guidance System Overview

IV.2.1 Ultrasound Transducer Selection

Freehand 3D ultrasound is an attractive option for enabling ultrasound-based image guidance systems because the approach can be implemented using any standard ultrasound system. Commercially available "drop-in" ultrasound probes designed for robotic surgery can be passed through standard laparoscopic trocars and feature grasping interfaces that enable manipulation using standard robotic graspers. Such drop-in ultrasound probes have largely replaced traditional laparoscopic ultrasound units in robotic surgery because they enable the operating surgeon to directly handle the probe rather than requiring coordination with a surgical assistant. Figure IV.1(a) shows a BK X12C4 drop-in ultrasound transducer (BK Medical Holding Company, Inc., Herlev, Denmark), one such probe that is specifically marketed for use with the da Vinci Surgical System. Adapting one of these commercially available probes would be a natural starting point for developing a commercially viable ultrasound-based image guidance system; however, for the purposes of this initial investigation, the image guidance system was built around the much more budget- and research-friendly MicrUS LV8-4L65S-3 PC-based ultrasound transducer (Telemed Joint Stock Company, Ltd., Vilnius, Lithuania), shown in Fig. IV.1(b). The LV8-4L65S-3 transducer has an adequately similar overall form factor to drop-in transducers for the current work; however the probe is significantly larger (130 mm length, 18.3 mm diameter versus 72.75 mm length, 9.9 mm

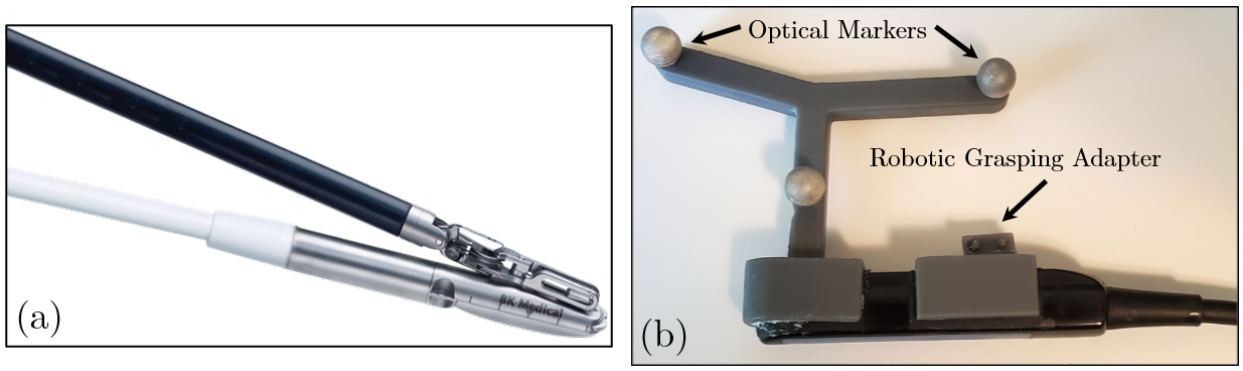

Figure IV.1: Ultrasound Probes for Robot-Assisted Surgery. (a) BK X12C4 drop-in ultrasound transducer, marketed for use with the da Vinci Surgical System [123]. (b) Telemed LV8-4L65S-3 veterinary ultrasound probe, as used in this work, with custom adapters for robotic grasping and optical tracking.

diameter) and heavier (220 g vs. 25 g) than the commercially available drop-in probe. As shown in Fig. IV.1(b), the probe was outfitted with an external grasping attachment to enable manipulation with the da Vinci EndoWrist ProGrasp instrument as well as optical tracking markers for external tracking.

IV.2.2 Ultrasound Calibration and Tracking

Implementing freehand 3D ultrasound requires determining the spatial relationship between the image plane of the ultrasound transducer and an external reference frame, a process commonly referred to in the literature as ultrasound calibration. The choice of external reference frame can be arbitrary as long as changes in the pose of the ultrasound plane can be tracked within that frame. For the purposes of ultrasound-based image guidance with the da Vinci robot, however, it is necessary to track the location of the ultrasound image plane with respect to an internal frame of the robot system in order to register preoperative images to the same frame. As previously mentioned, prior literature demonstrated accurate ultrasound tracking using a kinematic model to directly compute the pose of an ultrasound pose grasped by the robot [91]. Direct kinematic tracking proved infeasible for the current work due to the increased size and weight of the selected ultrasound probe. As such, ultrasound calibration and tracking were implemented in a two step process as described below.

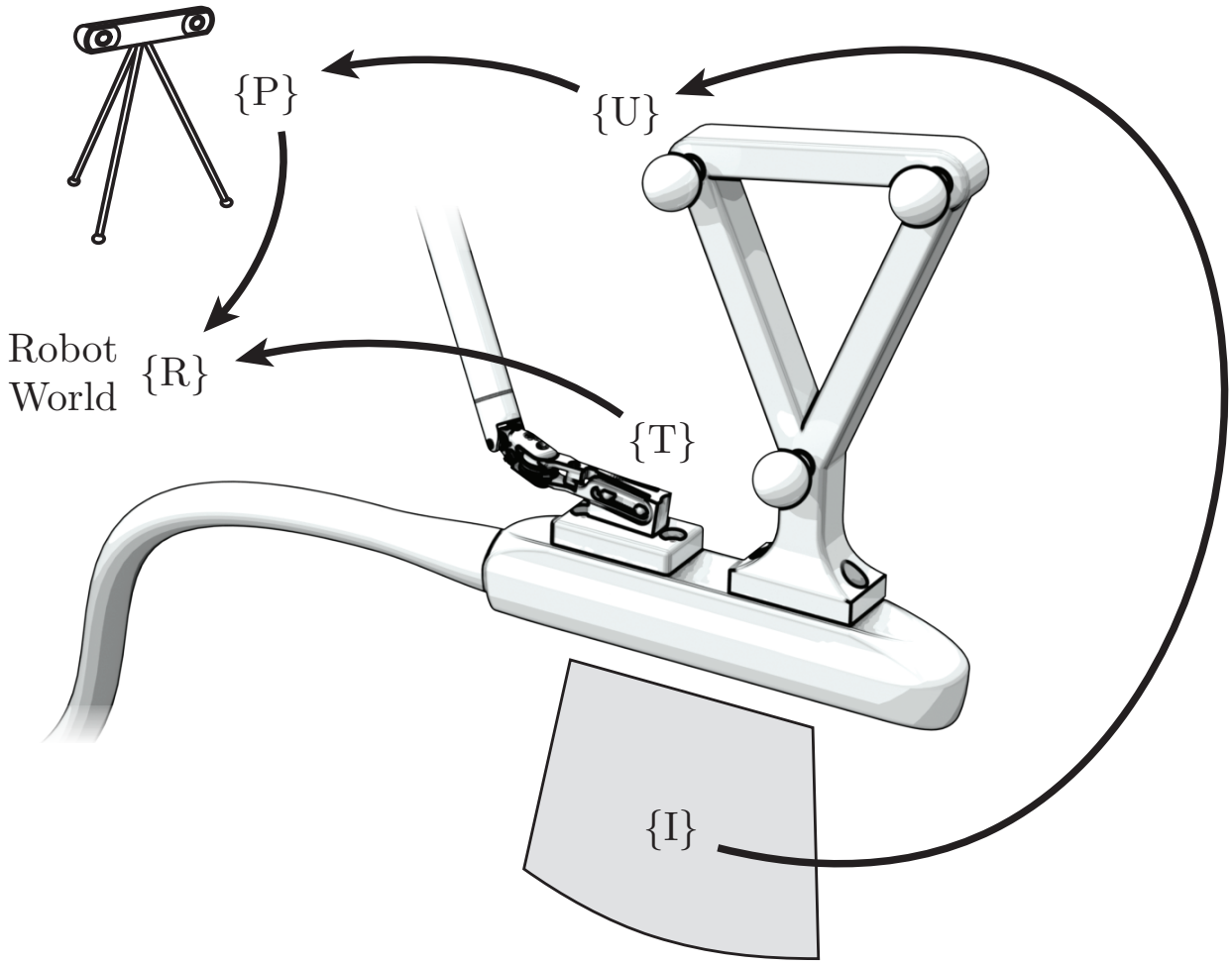

Figure IV.2: Intermediate coordinate frames used for ultrasound calibration and tracking. $\{I\}$ is the frame of the ultrasound image; $\{U\}$ is the local optically tracked frame attached to the ultrasound transducer body; $\{T\}$ is the frame of the robot manipulator; $\{P\}$ is the internal frame of the Polaris optical tracker; $\{R\}$ is the internal base frame of the robot, which is used as the "world" reference frame in this application.

Fig. IV.2 illustrates all of the intermediate coordinate frames involved in ultrasound calibration and tracking method implemented in this work. Standard ultrasound calibration was performed to determine the (constant) transform T_I^U from the image space of the ultrasound to an optically tracked frame attached to the case of the ultrasound probe (as shown in Fig. IV.1). A Polaris Vega (Northern Digital Inc., Waterloo, Ontario, Canada) optical tracking system was used throughout this work. The standard process of ultrasound calibration requires visualizing the tip of a tracked stylus (submerged in a suitable acoustic coupling medium, typically water) at various points throughout ultrasound image while simultaneously tracking both the ultrasound probe and the stylus. As a result, the location of identified points is known in both the image frame $\{I\}$ and the ultrasound frame $\{U\}$. A simple point-based registration can then compute an optimal value for the transformation T_I^U.

It is critical to note that any difference between the speed of sound in the acoustic coupling medium and the speed of sound value used by the ultrasound software will create displacement artifacts that distort spatial information inferred from ultrasound images. Subsequent images collected after calibration can be further distorted by variations in the coupling media compared to the coupling medium used during calibration. The problem of speed-based displacement artifacts poses a common challenge in clinical application of ultrasound given the variation of the speed of sound in different human tissues (*e.g.* 1440 m/s in fat and 1560 m/s in kidney parenchyma) versus the standard speed of sound assumed by clinical ultrasound machines (1540 m/s)[124]. As such, best practice dictates that ultrasound calibration be performed using a coupling medium with similar acoustic properties to the intended coupling media for later imaging. For this study, the stylus tip was submerged in a gelatin mixture matching the phantom fat material used in later experiments (see Sec. IV.3). Additionally, the transform T_I^U was also computed as a similarity transformation, rather than a rigid transformation, to compensate for errors in distance calculations caused by any difference between the speed of sound in the gelatin medium and the assumed

speed of sound used by the ultrasound software.

Once in the operating room, a standard hand-eye calibration procedure was preformed to register the internal coordinate frame of Polaris optical tracker, $\{P\}$, to the internal coordinate frame of the da Vinci robot, $\{R\}$ [125]. An optically tracked calibration object was grasped in the robot gripper and moved to numerous poses throughout the robot workspace. In each pose, the location of the calibration object was measured with the Polaris while the tip location of the robot end effector was kinematically tracked relative to the robot base frame. The resulting data allows for computation of the transformation T_P^R. Subsequently, the previously calibrated ultrasound probe was tracked directly by the optical tracker such that the image coordinate system could the be transformed into the robot's coordinate frame for generating image registration data.

IV.2.3 Ultrasound-Based Registration for Image Guidance

The most straightforward approach to obtain physical surface data from tracked ultrasound is to manually segment points on the target surface from individual ultrasound images. When trying to generate a sufficient quantity of data for surface based image registration, however, this approach is naturally limited by the planar, cross-sectional nature of ultrasound images, which makes inferring a meaningful surface topology from a reasonable number of images challenging. In the context of kidney surgery, this problem is further exacerbated by the fact that the smooth surface of the kidney generally exhibits only small changes in curvature over localized regions. On the whole, these factors present an impediment to ensure accurate correspondence in registration—*i.e.* that the registration transformation actually aligns image points to the same points in physical space.

Many previous implementations of ultrasound-based registration have addressed this challenge by focusing on obtaining physical space data corresponding to complex, branching venous structures. By focusing on features of distinct geometry, this approach adequately constrains registration calculations to ensure correspondence. Such an emphasis on vessel

structures is not favorable to application in the kidney, however, for two reasons in particular: (1) vessels around the kidney are known to deform significantly between preoperative imaging and surgery due to patient motion, and (2) the renal vessels are typically far from the region of surgical interest. In light of these facts, an approach to ultrasound-based registration that uses data from the surface of the kidney was developed for this work.

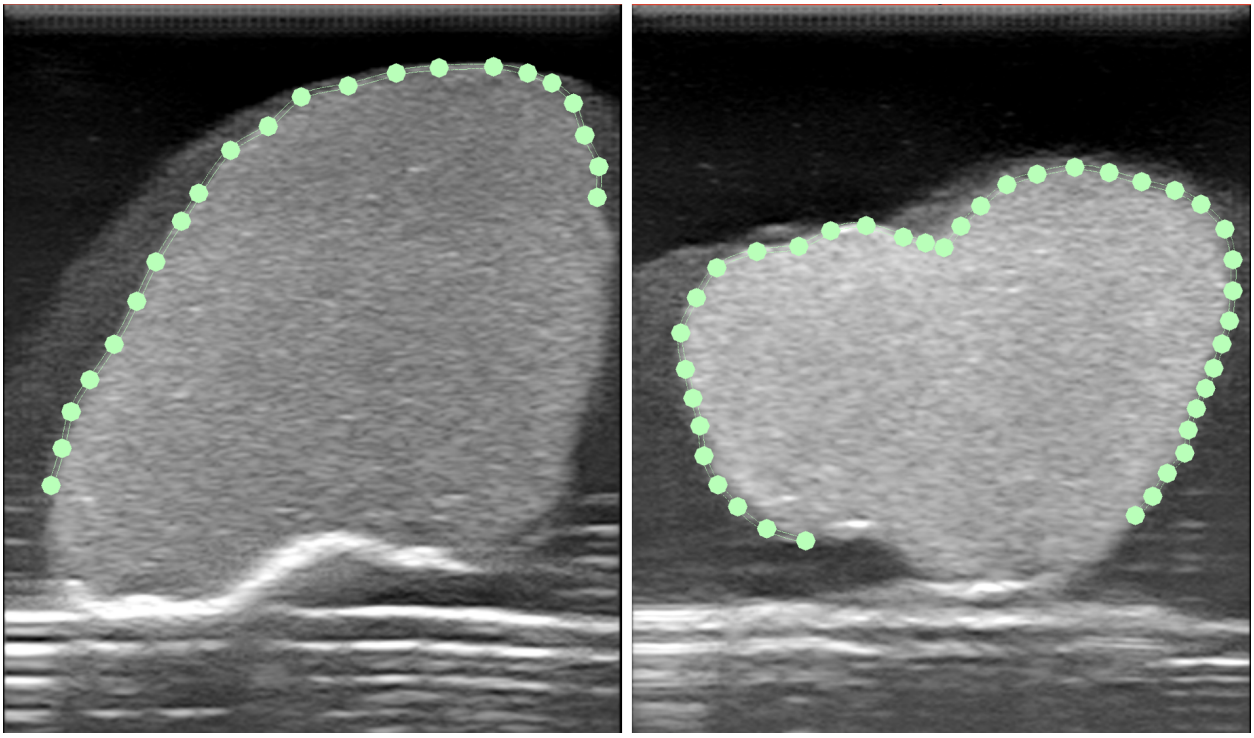

Figure IV.3: Examples of segmented ultrasound images used to acquire kidney surface data for image registration. In each image, several surface points were manually identified, then additional surface information was approximated by interpolating a spline between the anchor points.

The current approach was motivated by the conclusions of Ref. [98], which specifically studied surface registration with the kidney, and found that registration accuracy improved as more and more disparate "patches" of surface data were used for registration. Ultrasound is ideally suited to acquiring sparse, disconnected clusters of surface points spread over a large area. To acquire data of this character, the ultrasound image was swept along the length of the kidney. Qualitative analysis found that registration results were best when the plane was swept normal to the long axis of the kidney; however, this result was not rigorously

validated. From recorded ultrasound video, several points on the surface of the kidney were manually identified in several image slices taken along the entire length of the kidney, as shown in Fig. IV.3. Additional surface information was automatically approximated my interpolating a spline between the manually identified anchor points [126]. Registration was then calculated from the collected points using the globally optimal iterative closest point (GoICP) algorithm [100]. Figure IV.4 shows an example registration computed using this technique. Qualitative findings during this work suggest that segmenting 8 ultrasound image cross-sections distributed along the length of the kidney was adequate to ensure good correspondence. More detailed analysis of registration accuracy follows below.

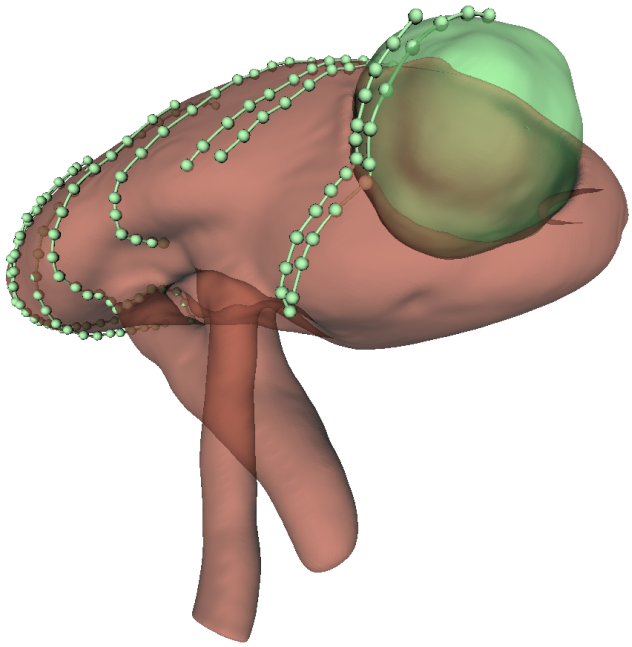

Figure IV.4: An example registration result from ultrasound-based registration. Green spheres indicate surface points manually segmented from ultrasound images; the kidney and tumor models were segmented from preoperative CT images.

IV.3 Dual Ultrasound- and CT-Compatible Phantoms

The experimental objectives of this work required creation of new anatomical phantoms that satisfy several competing criteria, namely: (i) mechanical semblance of live tissue, especially during dissection; (ii) CT imaging compatibility; and (iii) ultrasound imaging compatibility. Furthermore, the phantoms required that different tissue components (fat, renal parenchyma, and renal tumor) be mutually distinguishable in both imaging modalities.

All phantom components were gelatin based. Renal parenchyma was made from an aqueous solution of 10% m/m gelatin powder and 4% m/m psyllium husk powder. The inclusion of psyllium husk powder increased ultrasound scattering relative to other phantom components. Renal tumors were made from an aqueous solution of 15% m/m gelatin and 2% m/m barium sulfate. The increased concentration of gelatin made the renal masses stiffer than the renal parenchyma, mimicking the properties of corresponding human tissues; low concentration barium sulfate created adequate CT contrast between renal mass and parenchyma without distorting ultrasound imaging of the renal mass. Phantom fat tissue was made from an aqueous solution of 7% m/m gelatin and 6% m/m mineral oil. The inclusion of mineral oil helped simulate the slick and friable qualities of human fat while also improving CT contrast relative to other phantom materials. Water-based food dyes were added to each mixture to achieve desired coloring.

Phantom molds were additively manufactured based on 3D models of kidneys segmented from abdominal CT scans. In phantom construction, the renal mass was poured first and allowed to congeal completely. The renal mass was then registered inside the mold for renal parenchyma (which also contained a renal artery and a renal vein) and then the mold was filled with parenchyma phantom mixture. The temperature of the parenchyma mixture was controlled during pouring to achieve good adhesion between the renal mass and the parenchyma, ensuring that the mass would not naturally separate from the parenchyma during phantom dissection. The parenchyma mold was allowed to fully congeal before being covered in fat solution. The volume of fat solution was measured such that the closest point

of the kidney surface lay 8–10 mm below the surface of the fat after setting. Figure IV.5 shows a completed phantom, mounted to an optically tracked platform used in experiments throughout this work.

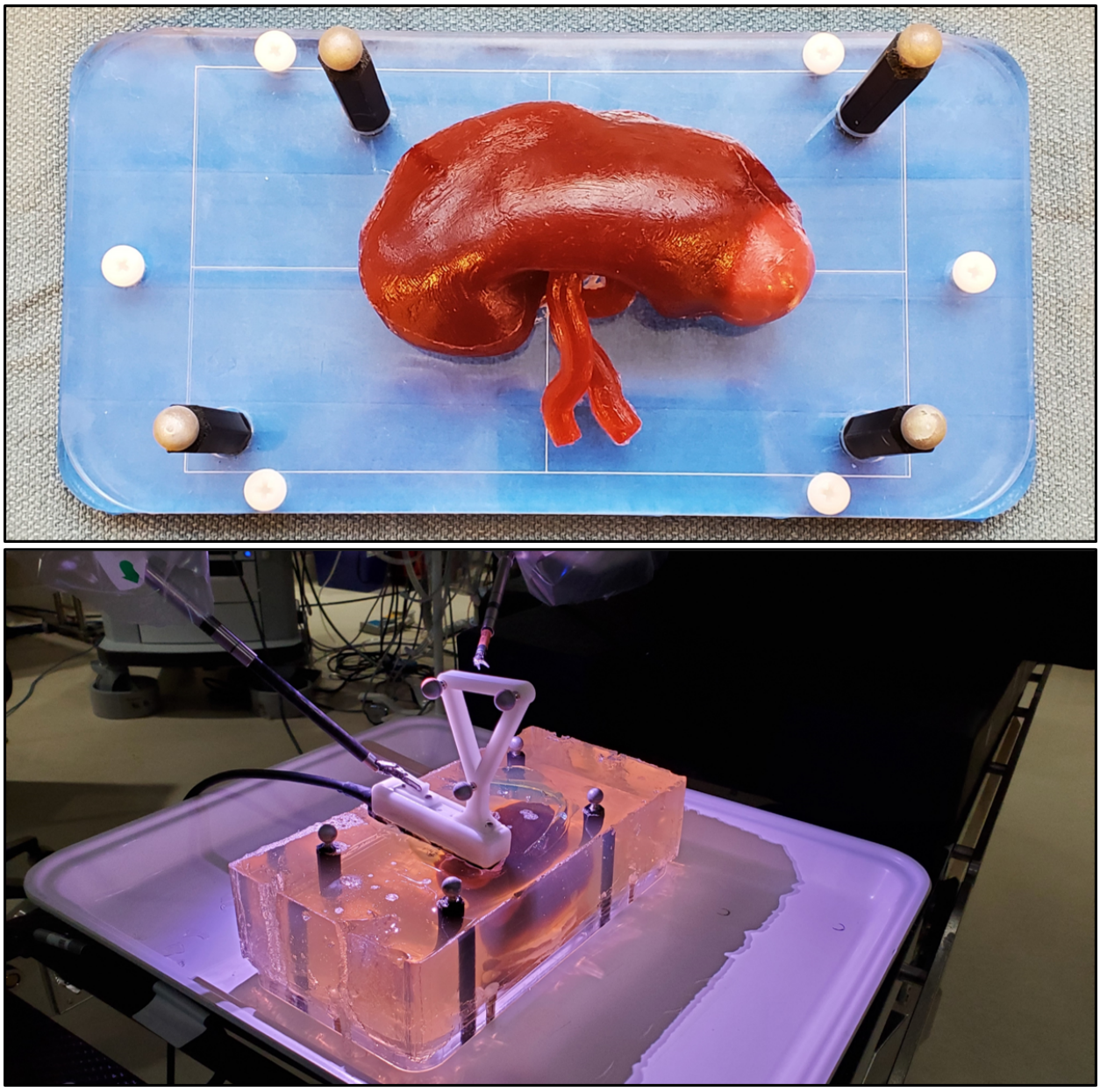

Figure IV.5: Anatomical phantoms for ultrasound experiments. (top) A kidney phantom with renal mass mounted to a rigid platform with optical tracking markers prior to encapsulation in fat. (bottom) Completed phantom in use in the operating room.

IV.4 Registration Accuracy

The accuracy of the ultrasound-based registration system was analyzed in a similar manner to the analysis of the touch-based registration system, described in Sec. III.5.2. Experiments to analyze the accuracy of the ultrasound-based registration system were conducted using a custom phantom, constructed as described above; the phantom used for these experiments did not contain models of renal vasculature. The phantom was fixed to an optically tracked platform, as shown in Fig. IV.5. Prior to experiments, the entire platform was CT scanned using an xCAT ENT Scanner (Xoran Technologies LLC, Ann Arbor, MI, USA) using a section thickness of 0.3 mm. The kidney surface as well as the optical tracking markers were manually segmented from the CT images using 3D Slicer [97]. The kidney surface segmentation was used to produce the required image space point set for registration. The segmentation of the optical tracking markers was used to compute the ground truth pose of the kidney model relative to the markers, which were optically tracked in the operating room.

To acquire physical space data, an experienced urologic surgeon used the tracked and calibrated ultrasound transducer, grasped by a ProGrasp Forceps instrument in a clinical da Vinci Xi system. Ultrasound video was recorded as the surgeon swept the image plane between the upper and lower poles of the kidney several times. Kidney surface points were extracted from individual frames of the ultrasound video according to the method described in Sec. IV.2.3. A total of 48 ultrasound images, spaced approximately evenly along the long axis of the kidney, were segmented for this experiment; each image contained 12–30 anchor points for spline interpolation. One hundred (100) smaller, 10-image sets were generated by randomly selecting images from the larger image set.

For each small image set, registration was computed using the GoICP algorithm to map the kidney model segmented from preoperative CT images to the robot's workspace. The pose of each registered kidney image was then compared to the ground truth pose, as measured using the optically tracked phantom platform. The quality of each computed registra-

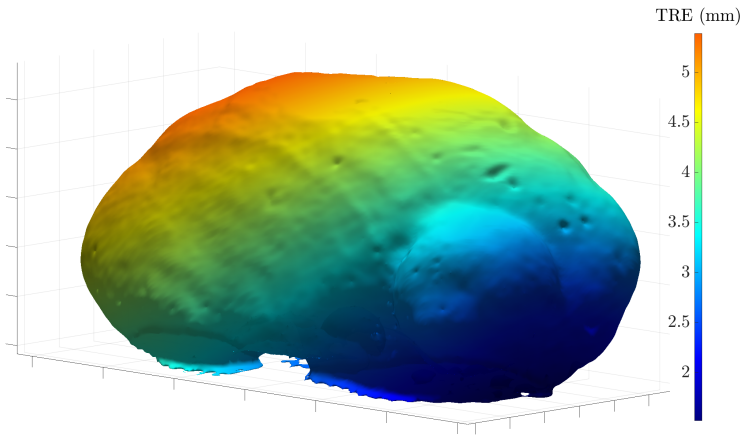

Figure IV.6: An example registration result using the ultrasound-based registration technique. The heat map shows the TRE over the entire model surface.

tion was evaluated by comparing the vertex positions of the registered kidney model to the corresponding vertex positions in the tracked, ground truth model. The target registration error (TRE) at each vertex of the registered model was computed as the distance between that vertex and the corresponding vertex of the ground truth model.

Figure IV.6 visualizes an example ultrasound-based registration as a heat map of the TRE over the entire kidney surface. Registration error is lowest in areas with high feature density and large variations of surface curvature, approximately 2–3.5 mm in the region immediately surrounding the tumor. Registration error is highest in areas of low curvature variation. This general trend was observed in many registrations performed throughout this work. Figure IV.7 shows the distribution of root-mean-square (RMS) TRE, computed over the entire kidney surface, for all 100 registrations included in this experiment. The average RMS TRE was 4.25 mm with a standard deviation of 1.12 mm.

IV.5 Phantom-Based Evaluation of Clinical Efficacy

For this work, the clinical motivation behind ultrasound-based image guidance is to enable image guidance at an early stage of the partial nephrectomy procedure, prior to fat dissection. Dissecting fat and locating underlying fragile renal vessels represent the most technically

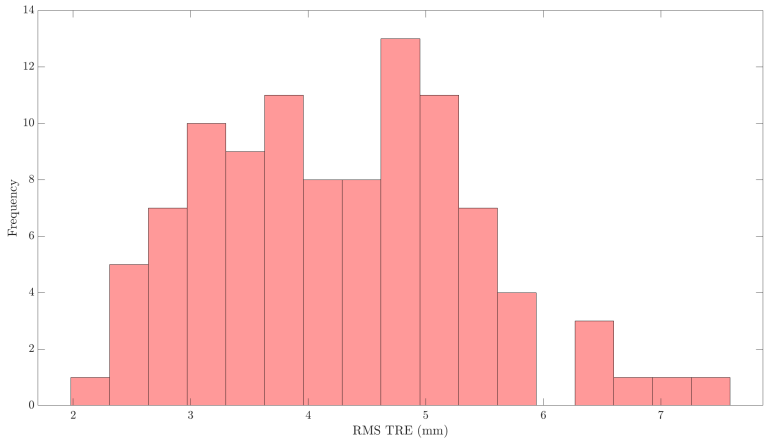

Figure IV.7: Distribution of RMS TRE (computed over the entire kidney surface) for 100 trials of the ultrasound-based registraion method.

challenging aspect of partial nephrectomy—especially for inexperienced surgeons. A series of phantom experiments were designed to evaluate the clinical utility of ultrasound-based image guidance when used by "surgeons" of three skill levels: novice (no medical training[1]), trainee (senior surgical resident), and expert (senior surgical fellow).

Each surgeon participated in two experiments in which they completed a set of simulated clinical tasks, using drop-in ultrasound in one experiment and ultrasound-based image registration in the other. The choice of whether to start with the image registration experiment or the drop-in ultrasound experiment was made at random for each surgeon. Two different kidney phantoms—created from different patient CT images—were prepared for each surgeon (one per experiment) according to the method described in Sec. IV.3. The choice of which phantom was used was also made at random at the beginning of each experiment. Using a different phantom in each experiment was intended to prevent potential bias caused by familiarity with the kidney anatomy gained after completing the first experiment. Each kidney phantom contained a partially endophytic renal mass approximately 45 mm in diameter. Each phantom also possessed a renal artery and a renal vein. Both phantoms had

[1]An engineer familiar with the da Vinci robot was chosen to act as the novice "surgeon" in these experiments. This selection was intended to minimize confounding effects caused by inexperience with the da Vinci interface.

the same RENAL score, which is a standardized scoring system for evaluating the surgical complexity of partial nephrectomy cases [127]. The renal score of the phantoms (7a) suggests that both represented an intermediate level of difficulty for performing partial nephrectomy.

To enable post hoc analysis of surgeon accuracy, the posterior surface of each kidney was fixed to an optically tracked phantom platform. In order to simulate effects of vessel motion and deformation, however, the renal vessels were not adhered to the rigid platform. Each kidney phantom (including the platform) was CT scanned prior to encapsulation in fat. These CT images were treated as preoperative scans and segmented to generate 3D models for image guidance. Kidney phantoms were then encapsulated in fat, which fixed the location of the renal vasculature (potentially in a different location than in the preoperative scans). The phantoms with fat were CT scanned again. These CT images were segmented to generate "ground truth" models for later accuracy evaluation. For these experiments, fat was colored deep black to ensure complete opacity.

For experiments using only drop-in ultrasound, surgeons had access to live ultrasound video displayed in the surgeon console through the da Vinci's TilePro display system while performing experimental tasks. For experiments with ultrasound-based image registration, surgeons used drop-in ultrasound to perform image registration according to the method described in Sec. IV.2.3 prior to starting assigned tasks; surgeons then had access to the image guidance display in TilePro (but not ultrasound video).

In each experiment, the surgeon completed three simulated clinical tasks. First, the surgeon attempted to place the tip of a tracked needle probe in the center of each renal vessel. This task was repeated a total of three times by each surgeon in each experiment. Next, the surgeon attempted to place the tip of the needle probe at the centroid of the renal mass. This task was also repeated a total of three times by each surgeon in each experiment. Finally, the surgeon was asked to resect the renal mass. Figure IV.8 shows the experimental setup in the operating room.

Surgeon performance in each experiment was evaluated on three criteria: (1) vessel local-

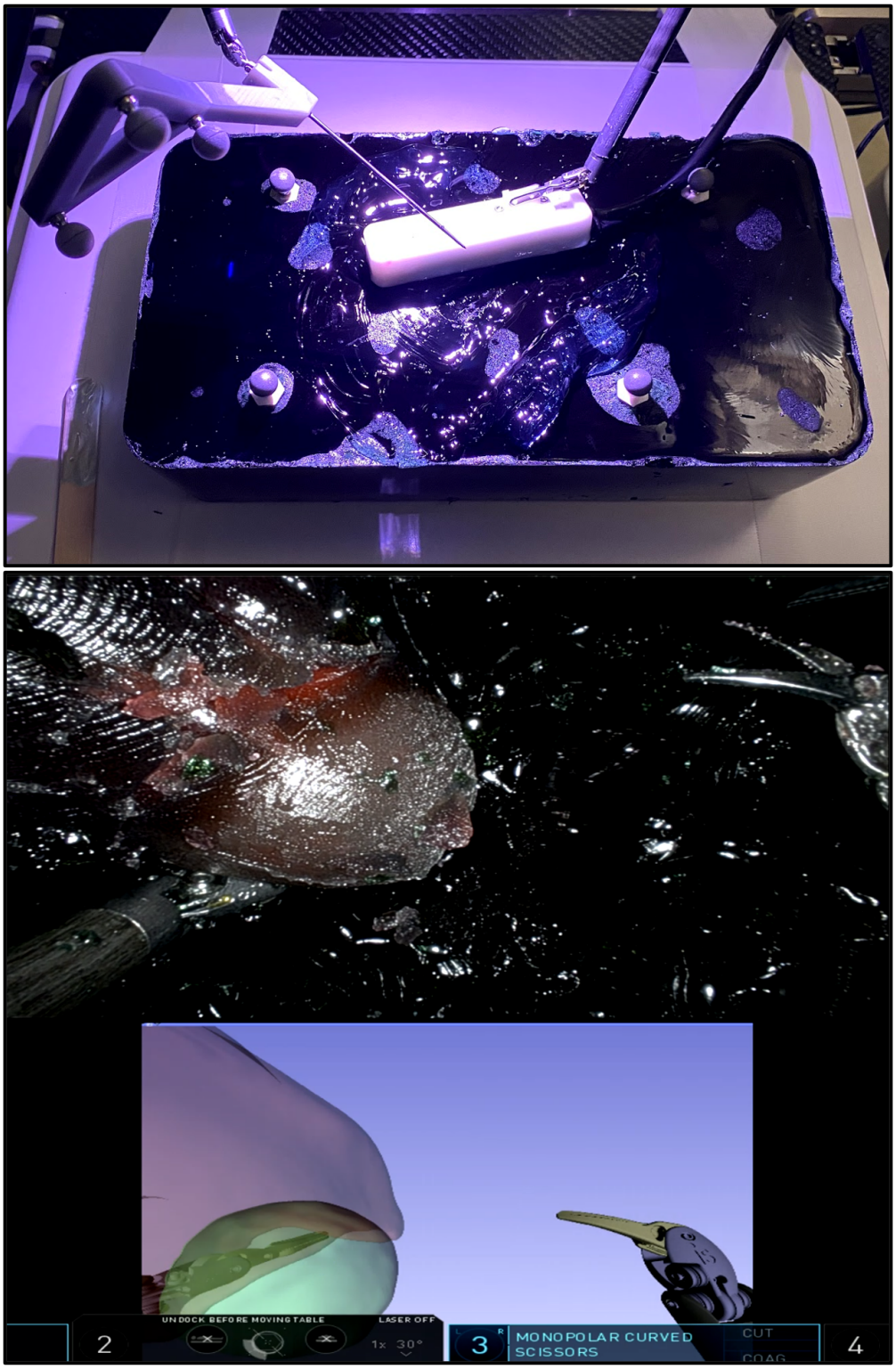

Figure IV.8: Experimental setup to evaluate clinical efficacy of ultrasound-based image guidance. (top) External view of needle placement activity using drop-in ultrasound. (bottom) Surgeon console view of tumor resection using image guidance.

ization accuracy, (2) tumor localization accuracy, and (3) volume of resection margin. Vessel localization error was calculated as the linear distance between the location of the needle tip and the closest point on the center line of the target vessel in the ground truth location (as measured by optically tracking the phantom platform). Similarly, tumor localization error was calculated as the linear distance between the measured location of needle tip and the ground truth location of the tumor centroid. All phantom material removed during tumor resection was collected and CT scanned postoperatively. The volume of kidney parenchyma removed from the phantom was calculated from the CT images and taken as the resection margin volume. Figures IV.9, IV.10, and IV.11 show the computed performance metrics for each surgeon during each experiment.

In both localization tasks, the ultrasound-based image guidance enabled a statistically significant decrease in localization error for both the novice and trainee surgeons but did not affect the expert surgeon's performance in a statistically significant way (though presented data might seem to imply that image guidance decreased vessel localization error and increased tumor localization error for the expert surgeon). In both cases the novice surgeon saw the largest decrease in error when comparing performance using ultrasound to that using image guidance; however the relative improvement of the novice surgeon's performance was only slightly greater than that of the trainee surgeon. These preliminary results support the dual hypotheses that (1) the clinical utility of intraoperative ultrasound depends heavily on user skill and (2) image guidance can improve the accuracy of inexperienced surgeons when attempting to locate subsurface anatomical features.

Image guidance significantly reduced the volume of healthy tissue removed by each surgeon during tumor resection. In contrast to the results from localization tasks, the expert surgeon saw the greatest improvement when using image guidance even though the expert surgeon achieved the lowest resection margin volume among all three surgeons using both feedback modalities. Understanding the manner in which surgeons use ultrasound to guide tumor resection is key to interpreting this result. In common practice, surgeons use the drop-

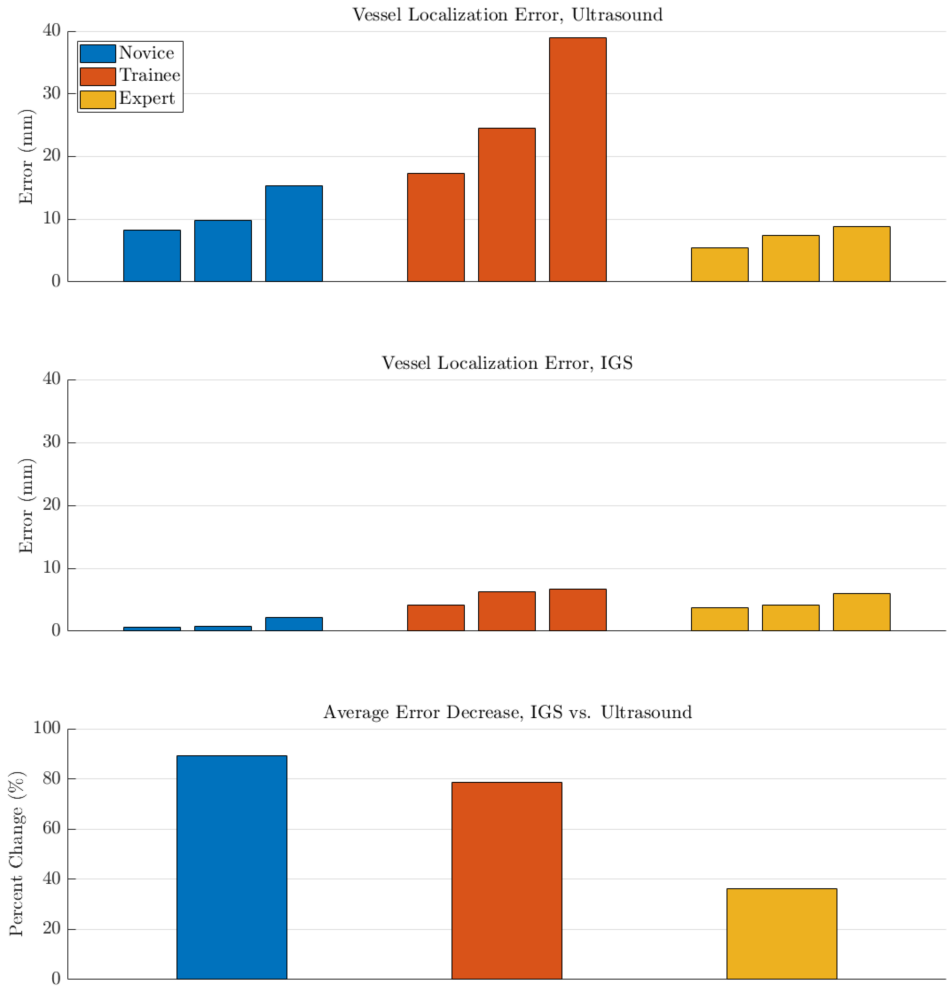

Figure IV.9: Vessel localization error for each surgeon when using drop-in ultrasound versus image guidance. (bottom) The percent reduction in localization error was computed from the average of all ultrasound-guided localization error and the average of all image-guided localization errors for each surgeon. Image guidance reduced localization error for the novice and trainee surgeons. The difference in localization errors was not statistically significant for the expert surgeon.

in ultrasound to help identify the (subsurface) endophytic boundary of the renal mass *before* beginning resection. The task of resection generally requires use of both manipulators, and as such, surgeons rarely use intraoperative ultrasound after resection has begun. In effect, the surgeon attempts to project a mental map of the tumor anatomy from memory onto the surgical scene during resection. Image guidance, on the other hand, provides real-time

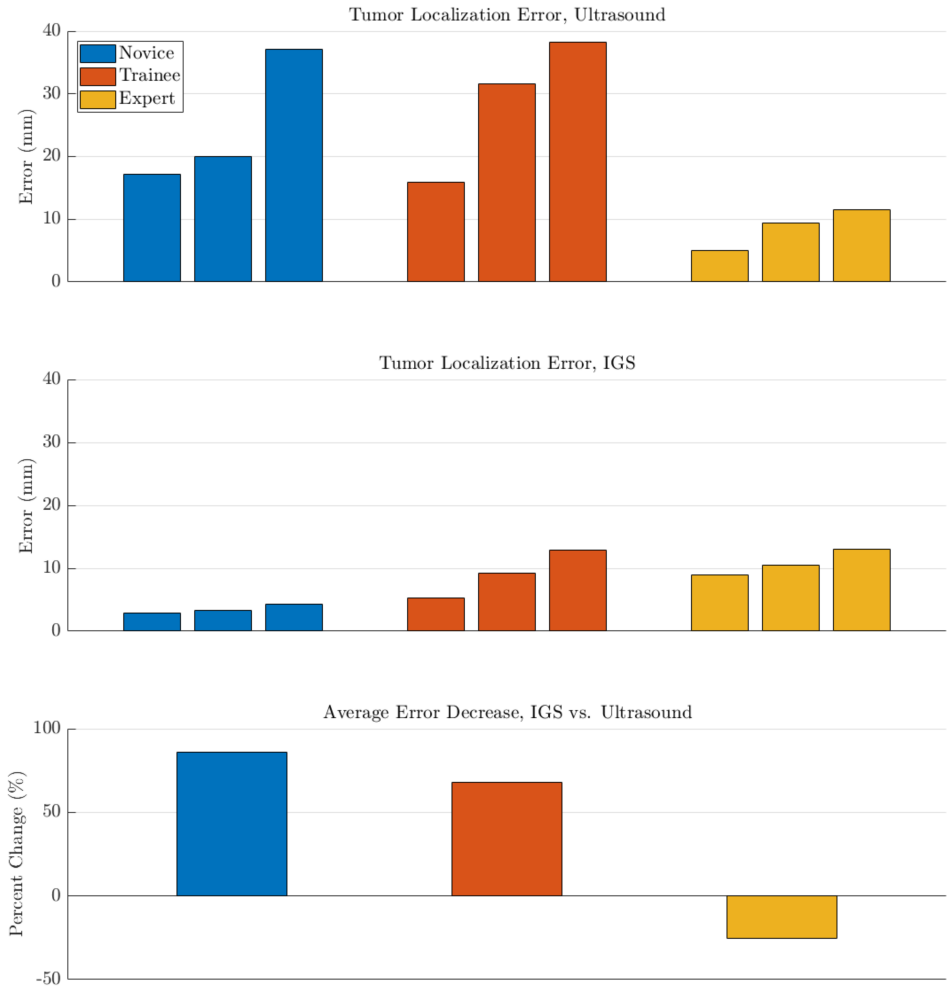

Figure IV.10: Tumor localization error for each surgeon when using drop-in ultrasound versus image guidance. (bottom) The percent reduction in localization error was computed from the average of all ultrasound-guided localization error and the average of all image-guided localization errors for each surgeon. Image guidance reduced localization error for the novice and trainee surgeons. The difference in localization errors was not statistically significant for the expert surgeon.

spatial information to the surgeon throughout resection. Thus, the benefit of image guidance during surgery is relative to the surgeon's intuitive spatial reasoning rather than the surgeon's ability to interpret ultrasound images. As such, image guidance has the potential to provide significant benefit to surgeon's during tumor resection, regardless of the surgeon's skill level.

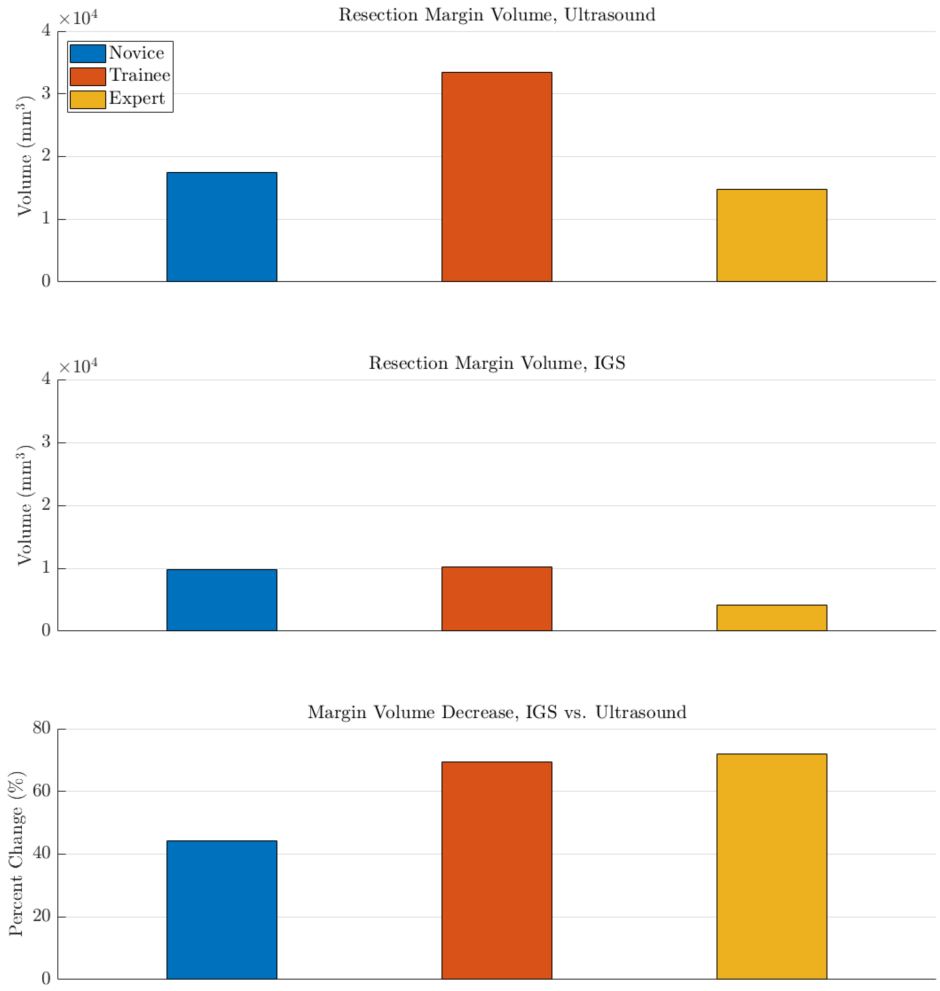

Figure IV.11: Volume of tumor resection margin when using drop-in ultrasound versus image guidance. Image guidance reduced resection volume for surgeons of all three skill levels.

IV.6 Conclusions and Future Work

This chapter presented an approach to ultrasound-based image registration that promises to make image guidance more feasible and more reliable during early stages of the partial nephrectomy procedure, specifically prior to dissection of perirenal fat and identification of renal vasculature. Using intraoperative ultrasound enables acquisition of kidney surface data through a layer of intervening fat. This work presented a method for extracting surface data from ultrasound images that uses spline interpolation to increase the amount of curvature information captured from the images. Analysis showed this approach to be on

par with other image registration results reported in the literature in terms of accuracy and repeatability. Finally, a series of studies with surgeons of varying skill levels demonstrated the potential of ultrasound-based image guidance to significantly improve surgeon's ability to localize subsurface anatomy compared to using intraoperative ultrasound. The results of this work indicate that incorporation of ultrasound-based image guidance has the potential to make robotic partial nephrectomy faster, safer, more accurate, and more accessible to inexperienced surgeons. By increasing the number of surgeons qualified and confident to perform robotic partial nephrectomy, ultrasound-based image guidance could increase patients' opportunity to receive underutilized nephron-sparing surgery.

Many open questions regarding surgical image guidance still remain, especially those related to organ movement and deformation, as discussed in Sec. III.7. Several opportunities also exist for improving the ultrasound segmentation method presented in this work, including automated surface detection, which would significantly increase the speed registration during ultrasound-based image guidance in the operating room. Furthermore, broader evaluation of the clinical efficacy of ultrasound-based image guidance will be necessary to develop a more nuanced and statistically powerful understanding of the advantages of ultrasound-based image guidance. Nonetheless, this preliminary work shows the promise of image guidance to empower surgeons to more accurately and confidently locate critical anatomy during delicate portions of the partial nephrectomy procedure, and ultimately, ultrasound-based image guidance promises to make the surgery more broadly accessible in the future.

CHAPTER V

Conclusions

Surgical robotics and medical image guidance are naturally complementary technologies. Together, they promise to act as the hands and the eyes of skilled surgeons and to extend the reach of their healing touch beyond their natural human limits. This dissertation has explored several innovative new approaches to surgical procedures that marry these technologies in the operating room to address major clinical needs.

Chapter II introduced a neurosurgical procedure enabled by a novel MRI-compatible robot and real-time MRI feedback that could cure temporal lobe epilepsy without ever requiring an incision in the skull. By designing concentric tube steerable needles tailored to the anatomy of individual patients and then demonstrating a "follow-the-leader" approach to atraumatically deploying curved needles in tissue, this work introduced a new means of safely and accurately accessing geometrically complex deep brain structures through the base of the skull, potentially enabling numerous therapies that previously would have been too invasive to attempt.

Chapters III and IV focused on bringing image guidance to the commercially successful da Vinci Surgical System, specifically to address existing clinical needs in robot-assisted partial nephrectomy. This work leveraged the inherent tracking accuracy of the da Vinci's kinematic chain to enable a touch-based method of acquisition of kidney surface data for image registration. This innovation enabled creation of a practical image guidance system that could be deployed in the operating room without requiring additional hardware and without compromising the accuracy of the image guidance. Initial experiments with an experienced urologic surgeon demonstrated the potential for image guidance to improve surgeon accuracy during partial nephrectomy. Next, this dissertation integrated intraoperative ultrasound with the image guidance system to enable image guidance during vessel dissec-

tion, one of the first steps of a partial nephrectomy procedure. Given that novice surgeons commonly encounter significant challenges with both interpreting intraoperative ultrasound and vessel dissection itself, a series of experiments examined the utility of ultrasound-based image guidance (in lieu of standard intraoperative ultrasound) in the hands of surgeons of various skill levels. Initial results showed significant improvements among less experienced surgeons using ultrasound-based image guidance, suggesting that this technology could serve to accelerate surgical training and improve safety in the future.

Appendix A

List of Publications

A.1 Journal Publications Relevant to Dissertation Work

1. N. L. Kavoussi, **E. B. Pitt**, J. M. Ferguson, J. Granna, N. Nimmagadda, R. Melnyk, A. Ghazi, R. J. Webster III, and S. D. Herrell III, "Accuracy of Touch-Based Registration During Robotic, Image-Guided Partial Nephrectomy Before and After Tumor Resection in Validated Phantoms," Journal of Endourology, in press.

2. J. M. Ferguson, **E. B. Pitt**, A. Kuntz, N. L. Kavoussi, E. J. Barth, S. D. Herrell III, and R. J. Webster III, "Comparing the Accuracy of the da Vinci Xi and da Vinci Si for Image Guidance and Automation," International Journal of Medical Robotics and Computer Assisted Surgery, in press.

3. **E. B. Pitt***, J. M. Ferguson*, N. L. Kavoussi, A. A. Remirez, M. A. Siebold, A. Kuntz, E. J. Barth, S. D. Herrell III, and R. J. Webster III, "Toward Practical and Accurate Touch-Based Image Guidance for Robotic Partial Nephrectomy," IEEE Transactions on Medical Robotics and Bionics, vol. 2, no. 2, pp. 196–205, 2020. ***Shared first authorship**

4. D. B. Comber, **E. B. Pitt**, H. B. Gilbert, M. W. Powelson, E. Matijevich, J. S. Neimat, R. J. Webster, III, and E. J. Barth, "Optimization of Curvilinear Needle Trajectories for Transforamenal Hippocampotomy," Operative Neurosurgery, vol. 13, no. 1, pp. 15–22, 2017.

5. **E. B. Pitt**, D. B. Comber, Y. Chen, J. S. Neimat, R. J. Webster, III, and E. J. Barth, "Follow-the-Leader Deployment of Steerable Needles Using a Magnetic Resonance-Compatible Robot with Stepper Actuators," ASME Journal of Medical Devices, vol. 10, no. 2, pp. 020945, 2016.

A.2 Conference Publications Relevant to Dissertation Work

1. **E. B. Pitt**, J. M. Ferguson, N. L. Kavoussi, E. J. Barth, R. J. Webster, III, and S. D. Herrell, "Intraoperative Guidance for Robotic Partial Nephrectomy Using Surface-Based Registration: Initial Model Assessment," in Proc. Engineering and Urology Society, 2019. **Best Paper Award**

2. Y. Chen, M. E. Poorman, D. B. Comber, **E. B. Pitt**, C. Liu, I. S. Godage, H. Yu, W. A. Grissom, E. J. Barth, and R. J. Webster, III, "Treating Epilepsy via Thermal Ablation: Initial Experiments with an MRI-Guided Concentric Tube Robot," in Design of Medical Devices Conference, 2017.

3. **E. B. Pitt**, P. J. Swaney, H. B. Gilbert, Y. Chen, R. J. Webster, III, and E. J. Barth, "Enabling Helical Needle Trajectories with Minimal Actuation: A Screw-Based Approach to Concentric Tube Needle Deployment," in Hamlyn Symposium on Medical Robotics, pp. 56-57, 2017.

4. D. B. Comber, **E. B. Pitt**, R. J. Webster III, and E. J. Barth, "Design and Control of a Pneumatic, Additively Manufactured Robot," in Fluid Power Innovation and Research Conference, 2015.

A.3 Other Publications

1. **E. B. Pitt**, E. J. Barth, Z. J. Diggins, et al. "Radiation Response and Adaptive Control-Based Degradation Mitigation of MEMS Accelerometers in Ionizing Dose Environments," IEEE Sensors Journal, vol. 17, no. 4, pp. 1132-1143, 2017.

2. **E. B. Pitt***, A. V. Pedchenko*, and E. J. Barth. "Analytical tools for investigating stability and power generation of electromagnetic vibration energy harvesters," IEEE/ASME Transactions on Mechatronics, vol. 21, no. 2, pp. 717–726, 2015. ***Shared first authorship**

3. **E. B. Pitt**, N. Simaan, and E. J. Barth "An Investigation of Stiffness Modulation Limits in a Pneumatically Actuated Parallel Robot With Actuation Redundancy," in ASME Fluid Power Systems Technology Conference, 2015.

4. Z. J. Diggins, N. Mahadevan, **E. B. Pitt**, et al. "Bayesian Inference Modeling of Total Ionizing Dose Effects on System Performance," IEEE Transactions on Nuclear Science, vol. 62, no. 6, pp. 2517–2524, 2015.

5. Z. J. Diggins, N. Mahadevan, **E. B. Pitt**, et al. "System Health Awareness in Total-Ionizing Dose Environments," IEEE Transactions on Nuclear Science, vol. 62, no. 4, pp. 1674–1681, 2015.

6. Z. J. Diggins, N. Mahadevan, ..., **E. B. Pitt**, et al., "Total-Ionizing-Dose Induced Timing Window Violations in CMOS Microcontrollers," IEEE Transactions on Nuclear Science, vol. 61, no. 6, pp. 2979–2984, 2014.

7. **E. B. Pitt**, G. Kumar, J. Schroers, "Temperature Dependence of the Thermoplastic Formability in Bulk Metallic Glasses," Journal of Applied Physics, vol. 110, no. 4, pp. 043518, 2011.

References

[1] Patrick Kwan and Martin J Brodie. Early identification of refractory epilepsy. *New England Journal of Medicine*, 342(5):314–319, 2000.

[2] Hyunmi Choi, Randall L Sell, Leslie Lenert, Peter Muennig, Robert R Goodman, Frank G Gilliam, and John B Wong. Epilepsy surgery for pharmacoresistant temporal lobe epilepsy: a decision analysis. *Jama*, 300(21):2497–2505, 2008.

[3] David M Ficker, EL So, WK Shen, JF Annegers, PC O'brien, Gregory D Cascino, and PG Belau. Population-based study of the incidence of sudden unexplained death in epilepsy. *Neurology*, 51(5):1270–1274, 1998.

[4] Samden D Lhatoo, Juliet K Solomon, Andrew W McEvoy, Neil D Kitchen, Simon D Shorvon, and Josemir W Sander. A prospective study of the requirement for and the provision of epilepsy surgery in the united kingdom. *Epilepsia*, 44(5):673–676, 2003.

[5] Pierre de Flon, Eva Kumlien, Christina Reuterwall, and Peter Mattsson. Empirical evidence of underutilization of referrals for epilepsy surgery evaluation. *European journal of neurology*, 17(4):619–625, 2010.

[6] Sabine G Uijl, Frans SS Leijten, Karel GM Moons, Ellen PHM Veltman, Cyrille H Ferrier, and Cees A van Donselaar. Epilepsy surgery can help many more adult patients with intractable seizures. *Epilepsy research*, 101(3):210–216, 2012.

[7] Ahmedin Jemal, Rebecca Siegel, Elizabeth Ward, Yongping Hao, Jiaquan Xu, and Michael J Thun. Cancer statistics, 2009. *CA: a cancer journal for clinicians*, 59(4):225–249, 2009.

[8] Paul Russo. Contemporary understanding and management of renal cortical tumors. *Urologic Clinics of North America*, 35(4):xiii–xvii, 2008.

[9] AC Novick, SC Campbell, A Belldegrun, ML Blute, GK Chow, IH Derweesh, Martha Faraday, Jihad Kaouk, Raymond Leveillee, Surena Matinlow, Paul Russo, and Robert Uzzo. Guideline for management of the clinical stage 1 renal mass. *Journal of Urology*, 182(4):1271–1279, 2009.

[10] Borje Ljungberga, Karim Bensalahb, Steven Canfieldc, Saeed Dabestanid, Fabian Hofmanne, Milan Horaf, Markus A. Kuczykg, Thomas Lamh, Lorenzo Marconii, Axel S. Merseburgerg, Peter Muldersj, Thomas Powlesk, Michael Staehlerl, Alessandro Volpem, and Axel Bex. EAU guidelines on renal cell carcinoma: 2014 update. *European Urology*, 67(5):913–924, 2015.

[11] R Houston Thompson, Stephen A Boorjian, Christine M Lohse, Bradley C Leibovich, Eugene D Kwon, John C Cheville, and Michael L Blute. Radical nephrectomy for pT1a renal masses may be associated with decreased overall survival compared with partial nephrectomy. *Journal of Urology*, 179(2):468–473, 2008.

[12] Hung-Jui Tan, Edward C Norton, Zaojun Ye, Khaled S Hafez, John L Gore, and David C Miller. Long-term survival following partial vs radical nephrectomy among older patients with early-stage kidney cancer. *JAMA*, 307(15):1629–1635, 2012.

[13] Hani J Marcus, Archie Hughes-Hallett, Christopher J Payne, Thomas P Cundy, Dipankar Nandi, Guang-Zhong Yang, and Ara Darzi. Trends in the diffusion of robotic surgery: A retrospective observational study. *International Journal of Medical Robotics and Computer Assisted Surgery*, 13(4):e1870, 2017.

[14] Brent K Hollenbeck, David A Taub, David C Miller, Rodney L Dunn, and John T Wei. National utilization trends of partial nephrectomy for renal cell carcinoma: a case of underutilization? *Journal of Urology*, 67(2):254–259, 2006.

[15] Sanjay G Patel, David F Penson, Baldeep Pabla, Peter E Clark, Michael S Cookson, Sam S Chang, S Duke Herrell, Joseph A Smith Jr, and Daniel A Barocas. National trends in the use of partial nephrectomy: a rising tide that has not lifted all boats. *Journal of Urology*, 187(3):816–821, 2012.

[16] Max A. Viergever, J.B. Antoine Maintz, Stefan Klein, Keelin Murphy, Marius Staring, and Josien P.W. Pluim. A survey of medical image registration—under review. *Medical Image Analysis*, 33:140 – 144, 2016.

[17] Henry Gray. *Anatomy of the human body*. Lea & Febiger, Philadelphia, 20 edition, 1918.

[18] Robert Clarke. On a method of investigating the deep ganglia and tracts of the central nervous system (cerebellum). *Br Med J*, 2:1799–1800, 1906.

[19] Robert Clarke and Victor Horsley. The structure and functions of the cerebellum examined by a new method. *Brain*, 30(6):45–124, 1908.

[20] Elekta AB. Leksell stereotactic system. https://www.elekta.com/neurosurgery/leksell-stereotactic-system/. Accessed: October 2019.

[21] Alexandre Carpentier, Roger J McNichols, R Jason Stafford, Julian Itzcovitz, Jean-Pierre Guichard, Daniel Reizine, Suzette Delaloge, Eric Vicaut, Didier Payen, Ashok Gowda, et al. Real-time magnetic resonance-guided laser thermal therapy for focal metastatic brain tumors. *Operative Neurosurgery*, 63(suppl_1):ONS21–ONS29, 2008.

[22] Gazanfar Rahmathulla, Pablo F Recinos, Jose E Valerio, Sam Chao, and Gene H Barnett. Laser interstitial thermal therapy for focal cerebral radiation necrosis: a case report and literature review. *Stereotactic and functional neurosurgery*, 90(3):192–200, 2012.

[23] Daniel J Curry, Ashok Gowda, Roger J McNichols, and Angus A Wilfong. Mr-guided stereotactic laser ablation of epileptogenic foci in children. *Epilepsy & Behavior*, 24(4):408–414, 2012.

[24] Paul S Larson, Philip A Starr, Geoffrey Bates, Lisa Tansey, R Mark Richardson, and Alastair J Martin. An optimized system for interventional magnetic resonance imaging-guided stereotactic surgery: preliminary evaluation of targeting accuracy. *Operative Neurosurgery*, 70(suppl_1):ons95–ons103, 2011.

[25] Ammar H Hawasli, Swapnil Bagade, Joshua S Shimony, Michelle Miller-Thomas, and Eric C Leuthardt. Magnetic resonance imaging-guided focused laser interstitial thermal therapy for intracranial lesions: single-institution series. *Neurosurgery*, 73(6):1007–1017, 2013.

[26] Jon T Willie, Nealen G Laxpati, Daniel L Drane, Ashok Gowda, Christina Appin, Chunhai Hao, Daniel J Brat, Sandra L Helmers, Amit Saindane, Sherif G Nour, et al. Real-time magnetic resonance-guided stereotactic laser amygdalohippocampotomy for mesial temporal lobe epilepsy. *Neurosurgery*, 74(6):569–585, 2014.

[27] Monteris Medical Inc. Neuroblate system: The minimally invasive surgical choice. https://www.monteris.com/healthcare-professionals/neuroblate-system/. Accessed: October 2019.

[28] David Benjamin Comber. *Design and Control of Magnetic Resonance-Compatible, Pneumatic Actuators and Robotic Platforms for Steerable Needle Interventions*. PhD thesis, Vanderbilt University, 2015.

[29] Hua-yin Yu, Nathanael D Hevelone, Stuart R Lipsitz, Keith J Kowalczyk, and Jim C Hu. Use, costs and comparative effectiveness of robotic assisted, laparoscopic and open urological surgery. *The Journal of urology*, 187(4):1392–1399, 2012.

[30] Jay Shah, Arpita Vyas, and Dinesh Vyas. The history of robotics in surgical specialties. *American journal of robotic surgery*, 1(1):12–20, 2014.

[31] Bertrand Guillonneau, Christian Jayet, Ashutosh Tewari, and Guy Vallancien. Robot assisted laparoscopic nephrectomy. *The Journal of urology*, 166(1):200–201, 2001.

[32] Jihad H Kaouk, Ali Khalifeh, Shahab Hillyer, Georges-Pascal Haber, Robert J Stein, and Riccardo Autorino. Robot-assisted laparoscopic partial nephrectomy: step-by-step contemporary technique and surgical outcomes at a single high-volume institution. *European urology*, 62(3):553–561, 2012.

[33] Jonathan Mobley and Brian M Benway. Robot-assisted partial nephrectomy. In *Minimally Invasive Urology*, pages 79–88. Springer, 2015.

[34] Samuel Wiebe, Michael Eliasziw, David R Bellhouse, and Christine Fallahay. Burden of epilepsy: the ontario health survey. *Canadian Journal of Neurological Sciences*, 26(4):263–270, 1999.

[35] Jerome Engel Jr, Samuel Wiebe, Jacqueline French, Michael Sperling, Peter Williamson, Dennis Spencer, Robert Gumnit, Catherine Zahn, Edward Westbrook, and Bruce Enos. Practice parameter: temporal lobe and localized neocortical resections for epilepsy: report of the quality standards subcommittee of the american

academy of neurology, in association with the american epilepsy society and the american association of neurological surgeons. *Epilepsia*, 44(6):741–751, 2003.

[36] Tomokatsu Hori, Fumitaka Yamane, Taku Ochiai, Motohiro Hayashi, and Takaomi Taira. Subtemporal amygdalohippocampectomy prevents verbal memory impairment in the language-dominant hemisphere. *Stereotactic and functional neurosurgery*, 80(1-4):18–21, 2003.

[37] Martin T Lutz, Hans Clusmann, Christian E Elger, Johannes Schramm, and Christoph Helmstaedter. Neuropsychological outcome after selective amygdalohippocampectomy with transsylvian versus transcortical approach: a randomized prospective clinical trial of surgery for temporal lobe epilepsy. *Epilepsia*, 45(7):809–816, 2004.

[38] H Gregor Wieser, Marcos Ortega, Alon Friedman, and Yasuhiro Yonekawa. Long-term seizure outcomes following amygdalohippocampectomy. *Journal of neurosurgery*, 98(4):751–763, 2003.

[39] Andrew G Parrent and Warren T Blume. Stereotactic amygdalohippocampotomy for the treatment of medial temporal lobe epilepsy. *Epilepsia*, 40(10):1408–1416, 1999.

[40] Ammar H Hawasli, S Kathleen Bandt, R Edward Hogan, Nicole Werner, and Eric C Leuthardt. Laser ablation as treatment strategy for medically refractory dominant insular epilepsy: therapeutic and functional considerations. *Stereotactic and functional neurosurgery*, 92(6):397–404, 2014.

[41] Robert J Webster III, Joseph M Romano, and Noah J Cowan. Mechanics of precurved-tube continuum robots. *IEEE Transactions on Robotics*, 25(1):67–78, 2008.

[42] D Caleb Rucker, Bryan A Jones, and Robert J Webster III. A geometrically exact model for externally loaded concentric-tube continuum robots. *IEEE transactions on robotics: a publication of the IEEE Robotics and Automation Society*, 26(5):769, 2010.

[43] Pierre E Dupont, Jesse Lock, Brandon Itkowitz, and Evan Butler. Design and control of concentric-tube robots. *IEEE Transactions on Robotics*, 26(2):209–225, 2009.

[44] Hunter B Gilbert, D Caleb Rucker, and Robert J Webster III. Concentric tube robots: The state of the art and future directions. In *Robotics Research*, pages 253–269. Springer, 2016.

[45] Hunter B Gilbert and Robert J Webster III. Rapid, reliable shape setting of superelastic nitinol for prototyping robots. *IEEE robotics and automation letters*, 1(1):98–105, 2015.

[46] Hunter B Gilbert, Joseph Neimat, and Robert J Webster. Concentric tube robots as steerable needles: Achieving follow-the-leader deployment. *IEEE Transactions on Robotics*, 31(2):246–258, 2015.

[47] David B Comber, Eric J Barth, and Robert J Webster. Design and control of an magnetic resonance compatible precision pneumatic active cannula robot. *Journal of Medical Devices*, 8(1):011003, 2014.

[48] David B Comber, Jonathon E Slightam, Vito R Gervasi, Joseph S Neimat, and Eric J Barth. Design, additive manufacture, and control of a pneumatic mr-compatible needle driver. *IEEE Transactions on Robotics*, 32(1):138–149, 2016.

[49] Hao Su, Diana C Cardona, Weijian Shang, Alexander Camilo, Gregory A Cole, D Caleb Rucker, Robert J Webster, and Gregory S Fischer. A mri-guided concentric tube continuum robot with piezoelectric actuation: a feasibility study. In *2012 IEEE International Conference on Robotics and Automation*, pages 1939–1945. IEEE, 2012.

[50] HG Wieser, CE Elger, and SRG Stodieck. The 'foramen ovale electrode': a new recording method for the preoperative evaluation of patients suffering from mesio-basal temporal lobe epilepsy. *Electroencephalography and clinical neurophysiology*, 61(4):314–322, 1985.

[51] Sameer A Sheth, Joshua P Aronson, Mouhsin M Shafi, H Wesley Phillips, Naymee Velez-Ruiz, Brian P Walcott, Churl-Su Kwon, Matthew K Mian, Andrew R Dykstra, Andrew Cole, et al. Utility of foramen ovale electrodes in mesial temporal lobe epilepsy. *Epilepsia*, 55(5):713–724, 2014.

[52] Reto J Bale, Ilse Laimer, Arno Martin, Andreas Schlager, Christoph Mayr, Michael Rieger, Benedikt V Czermak, Peter Kovacs, and Gerlig Widmann. Frameless stereotactic cannulation of the foramen ovale for ablative treatment of trigeminal neuralgia. *Operative Neurosurgery*, 59(suppl_4):ONS–394, 2006.

[53] Martin Hsiu-Chu Lin, Ming-Hsueh Lee, Ting-Chung Wang, Yu-Kai Cheng, Chen-Hsing Su, Chia-Mao Chang, and Jen-Tsung Yang. Foramen ovale cannulation guided by intraoperative computed tomography with integrated neuronavigation for the treatment of trigeminal neuralgia. *Acta neurochirurgica*, 153(8):1593–1599, 2011.

[54] Martin Ortler, Gerlig Widmann, Eugen Trinka, Thomas Fiegele, Wilhelm Eisner, Klaus Twerdy, Gerald Walser, Judith Dobesberger, Iris Unterberger, and Reto Bale. Frameless stereotactic placement of foramen ovale electrodes in patients with drug-refractory temporal lobe epilepsy. *Operative Neurosurgery*, 62(suppl_5):ONS481–ONS489, 2008.

[55] M Ortler, E Trinka, J Dobesberger, R Bauer, C Unterhofer, K Twerdy, G Walser, I Unterberger, E Donnemiller, T Gotwald, et al. Integration of multimodality imaging and surgical navigation in the management of patients with refractory epilepsy. a pilot study using a new minimally invasive reference and head-fixation system. *Acta neurochirurgica*, 152(2):365–378, 2010.

[56] Hans Johnson, Greg Harris, Kent Williams, et al. Brainsfit: mutual information rigid registrations of whole-brain 3d images, using the insight toolkit. *Insight J*, 57(1):1–10, 2007.

[57] Ta-Chih Lee, Rangasami L Kashyap, and Chong-Nam Chu. Building skeleton models via 3-d medial surface axis thinning algorithms. *CVGIP: Graphical Models and Image Processing*, 56(6):462–478, 1994.

[58] Jeffrey C Lagarias, James A Reeds, Margaret H Wright, and Paul E Wright. Convergence properties of the nelder–mead simplex method in low dimensions. *SIAM Journal on optimization*, 9(1):112–147, 1998.

[59] Allen R Wyler and Bruce P Hermann. Extent of medial temporal resection on outcome from anterior temporal lobectomy: A randomized prospective study. *Neurosurgery*, 41(1):327–328, 1997.

[60] Jesse Lock and Pierre E Dupont. Friction modeling in concentric tube robots. In *2011 IEEE International Conference on Robotics and Automation*, pages 1139–1146. IEEE, 2011.

[61] Fang-Yu Lin, Christos Bergeles, and Guang-Zhong Yang. Biometry-based concentric tubes robot for vitreoretinal surgery. In *2015 37th annual international conference of the IEEE engineering in medicine and biology society (EMBC)*, pages 5280–5284. IEEE, 2015.

[62] Gang Li, Hao Su, Gregory A Cole, Weijian Shang, Kevin Harrington, Alex Camilo, Julie G Pilitsis, and Gregory S Fischer. Robotic system for mri-guided stereotactic neurosurgery. *IEEE transactions on biomedical engineering*, 62(4):1077–1088, 2014.

[63] Taylor Fisher, Abbi Hamed, Panagiotis Vartholomeos, Ken Masamune, Guoyi Tang, Hongliang Ren, and Zion TH Tse. Intraoperative magnetic resonance imaging–conditional robotic devices for therapy and diagnosis. *Proceedings of the Institution of Mechanical Engineers, Part H: Journal of Engineering in Medicine*, 228(3):303–318, 2014.

[64] Niki Abolhassani, Rajni Patel, and Mehrdad Moallem. Needle insertion into soft tissue: A survey. *Medical engineering & physics*, 29(4):413–431, 2007.

[65] Kyle B Reed, Ann Majewicz, Vinutha Kallem, Ron Alterovitz, Ken Goldberg, Noah J Cowan, and Allison M Okamura. Robot-assisted needle steering. *IEEE robotics & automation magazine*, 18(4):35–46, 2011.

[66] Daniel Y Sze. Use of curved needles to perform biopsies and drainages of inaccessible targets. *Journal of vascular and interventional radiology*, 12(12):1441–1444, 2001.

[67] E Bryn Pitt, David B Comber, Yue Chen, Joseph S Neimat, Robert J Webster, and Eric J Barth. Follow-the-leader deployment of steerable needles using a magnetic resonance-compatible robot with stepper actuators. *Journal of Medical Devices*, 10(2), 2016.

[68] Yue Chen, Megan E Poorman, David B Comber, E Bryn Pitt, Cindy Liu, Isuru S Godage, Hong Yu, William A Grissom, Eric J Barth, and Robert J Webster. Treating epilepsy via thermal ablation: initial experiments with an mri-guided concentric tube robot. In *2017 Design of Medical Devices Conference*. American Society of Mechanical Engineers Digital Collection, 2017.

[69] Rowena E Ong, Courtenay Glisson, Hernan Altamar, Davis Viprakasit, Peter Clark, S Duke Herrell, and Robert L Galloway. Intraprocedural registration for image-guided kidney surgery. *Transactions on Mechatronics*, 15(6):847–852, 2010.

[70] Hernan O Altamar, Rowena E Ong, Courtenay L Glisson, Davis P Viprakasit, Michael I Miga, Stanley Duke Herrell, and Robert L Galloway. Kidney deformation and intraprocedural registration: a study of elements of image-guided kidney surgery. *Journal of Endourology*, 25(3):511–517, 2011.

[71] Matthias Baumhauer, Tobias Simpfendörfer, Beat P Müller-Stich, Dogu Teber, Carsten N Gutt, Jens Rassweiler, H-P Meinzer, and Ivo Wolf. Soft tissue navigation for laparoscopic partial nephrectomy. *International Journal of Computer Assisted Radiology and Surgery*, 3(3-4):307, 2008.

[72] Dogu Teber, Selcuk Guven, Tobias Simpfendörfer, Mathias Baumhauer, Esref Oguz Güven, Faruk Yencilek, Ali Serdar Gözen, and Jens Rassweiler. Augmented reality: a new tool to improve surgical accuracy during laparoscopic partial nephrectomy? Preliminary in vitro and in vivo results. *European Urology*, 56(2):332–338, 2009.

[73] Sam B Bhayani and Devon C Snow. Novel dynamic information integration during da Vinci robotic partial nephrectomy and radical nephrectomy. *Journal of Robotic Surgery*, 2(2):67–69, 2008.

[74] Francesco Volonté, Nicolas C Buchs, François Pugin, Joël Spaltenstein, Boris Schiltz, Minoa Jung, Monika Hagen, Osman Ratib, and Philippe Morel. Augmented reality to the rescue of the minimally invasive surgeon. The usefulness of the interposition of stereoscopic images in the da Vinci™ robotic console. *International Journal of Medical Robotics and Computer Assisted Surgery*, 9(3):e34–e38, 2013.

[75] Osamu Ukimura and Inderbir S Gill. Imaging-assisted endoscopic surgery: Cleveland clinic experience. *Journal of endourology*, 22(4):803–810, 2008.

[76] Kazuhiro Nakamura, Yukio Naya, Satoki Zenbutsu, Kazuhiro Araki, Shuko Cho, Sho Ohta, Naoki Nihei, Hiroyoshi Suzuki, Tomohiko Ichikawa, and Tatsuo Igarashi. Surgical navigation using three-dimensional computed tomography images fused intraoperatively with live video. *Journal of endourology*, 24(4):521–524, 2010.

[77] Li-Ming Su, Balazs P Vagvolgyi, Rahul Agarwal, Carol E Reiley, Russell H Taylor, and Gregory D Hager. Augmented reality during robot-assisted laparoscopic partial nephrectomy: toward real-time 3D-CT to stereoscopic video registration. *Journal of Urology*, 73(4):896–900, 2009.

[78] Philip Pratt, Erik Mayer, Justin Vale, Daniel Cohen, Eddie Edwards, Ara Darzi, and Guang-Zhong Yang. An effective visualisation and registration system for image-guided robotic partial nephrectomy. *Journal of Robotic Surgery*, 6(1):23–31, 2012.

[79] David Bouget, Max Allan, Danail Stoyanov, and Pierre Jannin. Vision-based and marker-less surgical tool detection and tracking: a review of the literature. *Medical image analysis*, 35:633–654, 2017.

[80] Mario Aricò and Guillaume Morel. Pns: a perspective-n-spheres algorithm for laparoscope calibration in minimally invasive surgery. In *2019 IEEE/RSJ International Conference on Intelligent Robots and Systems (IROS)*, pages 6276–6281. IEEE, 2019.

[81] Rémi Wolf, Josselin Duchateau, Philippe Cinquin, and Sandrine Voros. 3d tracking of laparoscopic instruments using statistical and geometric modeling. In *International Conference on Medical Image Computing and Computer-Assisted Intervention*, pages 203–210. Springer, 2011.

[82] Austin Reiter, Peter K Allen, and Tao Zhao. Articulated surgical tool detection using virtually-rendered templates. In *Computer Assisted Radiology and Surgery (CARS)*, pages 1–8, 2012.

[83] Zerui Wang, Ziwei Liu, Qianli Ma, Alexis Cheng, Yun-hui Liu, Sungmin Kim, Anton Deguet, Austin Reiter, Peter Kazanzides, and Russell H Taylor. Vision-based calibration of dual rcm-based robot arms in human-robot collaborative minimally invasive surgery. *IEEE Robotics and Automation Letters*, 3(2):672–679, 2018.

[84] David M Kwartowitz, S Duke Herrell, and Robert L Galloway. Toward image-guided robotic surgery: determining intrinsic accuracy of the da Vinci robot. *International Journal of Computer Assisted Radiology and Surgery*, 1(3):157–165, 2006.

[85] David M Kwartowitz, S Duke Herrell, and Robert L Galloway. Update: Toward image-guided robotic surgery: determining the intrinsic accuracy of the daVinci-s robot. *International Journal of Computer Assisted Radiology and Surgery*, 1(5):301–304, 2007.

[86] David Morgan Kwartowitz, Michael I Miga, S Duke Herrell, and Robert L Galloway. Towards image guided robotic surgery: multi-arm tracking through hybrid localization. *International Journal of Computer Assisted Radiology and Surgery*, 4(3):281–286, 2009.

[87] Stanley D Herrell, David Morgan Kwartowitz, Paul M Milhoua, and Robert L Galloway. Toward image guided robotic surgery: system validation. *Journal of Urology*, 181(2):783–790, 2009.

[88] Joshua Leven, Darius Burschka, Rajesh Kumar, Gary Zhang, Steve Blumenkranz, Xiangtian Donald Dai, Mike Awad, Gregory D Hager, Mike Marohn, Mike Choti, et al. Davinci canvas: a telerobotic surgical system with integrated, robot-assisted, laparoscopic ultrasound capability. In *International Conference on Medical Image Computing and Computer-Assisted Intervention*, pages 811–818. Springer, 2005.

[89] Omid Mohareri, Caitlin Schneider, Troy K Adebar, Mike C Yip, Peter Black, Christopher Y Nguan, Dale Bergman, Jonathan Seroger, Simon DiMaio, and Septimiu E Salcudean. Ultrasound-based image guidance for robot-assisted laparoscopic radical prostatectomy: initial in-vivo results. In *International Conference on Information Processing in Computer-Assisted Interventions*, pages 40–50. Springer, 2013.

[90] O Mohareri and S Salcudean. da vinci® auxiliary arm as a robotic surgical assistant for semi-autonomous ultrasound guidance during robot-assisted laparoscopic surgery. In *Proceedings of the 7th Hamlyn Symposium on Medical Robotics*, pages 45–46, 2014.

[91] Caitlin Schneider, Christopher Nguan, Robert Rohling, and Septimiu Salcudean. Tracked "pick-up" ultrasound for robot-assisted minimally invasive surgery. *IEEE Transactions on Biomedical Engineering*, 63(2):260–268, 2015.

[92] James M Ferguson, Leon Y Cai, Alexander Reed, Michael Siebold, Smita De, S Duke Herrell, and Robert J Webster. Toward image-guided partial nephrectomy with the da Vinci robot: exploring surface acquisition methods for intraoperative re-registration. In *SPIE Medical Imaging*, volume 10576. International Society for Optics and Photonics, 2018.

[93] Andrew D Wiles, David G Thompson, and Donald D Frantz. Accuracy assessment and interpretation for optical tracking systems. In *Medical Imaging 2004: Visualization, Image-Guided Procedures, and Display*, volume 5367, pages 421–433. International Society for Optics and Photonics, 2004.

[94] Samad Hayati and M Mirmirani. Improving the absolute positioning accuracy of robot manipulators. *Journal of Robotic Systems*, 2(4):397–413, 1985.

[95] Samad Hayati, Kam Tso, and Gerald Roston. Robot geometry calibration. In *Proceedings. 1988 IEEE International Conference on Robotics and Automation*, pages 947–951. IEEE, 1988.

[96] Marco A Meggiolaro and Steven Dubowsky. An analytical method to eliminate the redundant parameters in robot calibration. In *Proceedings 2000 ICRA. Millennium Conference. IEEE International Conference on Robotics and Automation. Symposia Proceedings (Cat. No. 00CH37065)*, volume 4, pages 3609–3615. IEEE, 2000.

[97] Steve Pieper, Michael Halle, and Ron Kikinis. 3D slicer. In *International Symposium on Biomedical Imaging*, pages 632–635, 2004.

[98] Anne B Benincasa, Logan W Clements, S Duke Herrell, and Robert L Galloway. Feasibility study for image-guided kidney surgery: Assessment of required intraoperative surface for accurate physical to image space registrations. *Medical Physics*, 35(9):4251–4261, 2008.

[99] Fausto Bernardini, Joshua Mittleman, Holly Rushmeier, Cláudio Silva, and Gabriel Taubin. The ball-pivoting algorithm for surface reconstruction. *Transactions on Visualization and Computer Graphics*, 5(4):349–359, 1999.

[100] Jiaolong Yang, Hongdong Li, Dylan Campbell, and Yunde Jia. Go-ICP: a globally optimal solution to 3D ICP point-set registration. *Transactions on Pattern Analysis and Machine Intelligence*, 38(11):2241–2254, 2016.

[101] Simon DiMaio and Chris Hasser. The da Vinci research interface. In *MICCAI Workshop on Systems and Architecture for Computer Assisted Interventions*, 2008.

[102] Andras Lasso, Tamas Heffter, Adam Rankin, Csaba Pinter, Tamas Ungi, and Gabor Fichtinger. Plus: open-source toolkit for ultrasound-guided intervention systems. *Transactions on Biomedical Engineering*, 61(10):2527–2537, 2014.

[103] Junichi Tokuda, Gregory S Fischer, Xenophon Papademetris, Ziv Yaniv, Luis Ibanez, Patrick Cheng, Haiying Liu, Jack Blevins, Jumpei Arata, Alexandra J Golby, et al. OpenIGTLink: an open network protocol for image-guided therapy environment. *International Journal of Medical Robotics and Computer Assisted Surgery*, 5(4):423–434, 2009.

[104] ZVIS Roth, B Mooring, and Bahram Ravani. An overview of robot calibration. *IEEE Journal on Robotics and Automation*, 3(5):377–385, 1987.

[105] J Michael Fitzpatrick, Jay B West, and Calvin R Maurer. Predicting error in rigid-body point-based registration. *Transactions on Medical Imaging*, 17(5):694–702, 1998.

[106] Caitlin Schneider, Christopher Nguan, Michelle Longpre, Robert Rohling, and Septimiu Salcudean. Motion of the kidney between preoperative and intraoperative positioning. *Transactions on Biomedical Engineering*, 60(6):1619–1627, 2013.

[107] Tobias Simpfendörfer, Claudia Gasch, Gencay Hatiboglu, Michael Müller, Lena Maier-Hein, Markus Hohenfellner, and Dogu Teber. Intraoperative computed tomography imaging for navigated laparoscopic renal surgery: first clinical experience. *Journal of endourology*, 30(10):1105–1111, 2016.

[108] Ivan Figueroa-Garcia, Jean-Marc Peyrat, Ghassan Hamarneh, and Rafeef Abugharbieh. Biomechanical kidney model for predicting tumor displacement in the presence of external pressure load. In *2014 IEEE 11th International Symposium on Biomedical Imaging (ISBI)*, pages 810–813. IEEE, 2014.

[109] Rowena E Ong, Courtenay L Glisson, S Duke Herrell, Michael I Miga, and Robert Galloway. A deformation model for non-rigid registration of the kidney. In *Medical Imaging 2009: Visualization, Image-Guided Procedures, and Modeling*, volume 7261, page 72613A. International Society for Optics and Photonics, 2009.

[110] Robert L Galloway and Michael I Miga. Organ deformation and navigation. In *Imaging and Visualization in The Modern Operating Room*, pages 121–132. Springer, 2015.

[111] Nicholas J Nickl, Manoop S Bhutani, Marc Catalano, Brenda Hoffman, Robert Hawes, Amitabh Chak, Leor D Roubein, Michael Kimmey, Milton Johnson, John Affronti, et al. Clinical implications of endoscopic ultrasound: the american endosonography club study. *Gastrointestinal endoscopy*, 44(4):371–377, 1996.

[112] SW Smith, GE Trahey, and OT Von Ramm. Two-dimensional arrays for medical ultrasound. *Ultrasonic Imaging*, 14(3):213–233, 1992.

[113] Ole Vegard Solberg, Frank Lindseth, Hans Torp, Richard E Blake, and Toril A Nagelhus Hernes. Freehand 3d ultrasound reconstruction algorithms—a review. *Ultrasound in medicine & biology*, 33(7):991–1009, 2007.

[114] Mohammad Hamed Mozaffari and Won-Sook Lee. Freehand 3-d ultrasound imaging: a systematic review. *Ultrasound in medicine & biology*, 43(10):2099–2124, 2017.

[115] Thomas Kuiran Chen, Purang Abolmaesumi, David R Pichora, and Randy E Ellis. A system for ultrasound-guided computer-assisted orthopaedic surgery. *Computer Aided Surgery*, 10(5-6):281–292, 2005.

[116] Seth Billings, Hyun Jae Kang, Alexis Cheng, Emad Boctor, Peter Kazanzides, and Russell Taylor. Minimally invasive registration for computer-assisted orthopedic surgery: combining tracked ultrasound and bone surface points via the p-imlop algorithm. *International journal of computer assisted radiology and surgery*, 10(6):761–771, 2015.

[117] Steffen Schumann. State of the art of ultrasound-based registration in computer assisted orthopedic interventions. In *Computational radiology for orthopaedic interventions*, pages 271–297. Springer, 2016.

[118] Ingerid Reinertsen, Maxime Descoteaux, Kaleem Siddiqi, and D Louis Collins. Validation of vessel-based registration for correction of brain shift. *Medical image analysis*, 11(4):374–388, 2007.

[119] Graeme P Penney, Jane M Blackall, MS Hamady, T Sabharwal, A Adam, and David J Hawkes. Registration of freehand 3d ultrasound and magnetic resonance liver images. *Medical image analysis*, 8(1):81–91, 2004.

[120] Thomas Lange, Nils Papenberg, Stefan Heldmann, Jan Modersitzki, Bernd Fischer, Hans Lamecker, and Peter M Schlag. 3d ultrasound-ct registration of the liver using combined landmark-intensity information. *International journal of computer assisted radiology and surgery*, 4(1):79–88, 2009.

[121] Jennifer K Logan, Soroush Rais-Bahrami, Baris Turkbey, Andrew Gomella, Hayet Amalou, Peter L Choyke, Bradford J Wood, and Peter A Pinto. Current status of mri and ultrasound fusion software platforms for guidance of prostate biopsies. *BJU international*, 114(5):641, 2014.

[122] Omid Mohareri, Guy Nir, Julio Lobo, Richard Savdie, Peter Black, and Septimiu Salcudean. A system for mr-ultrasound guidance during robot-assisted laparoscopic radical prostatectomy. In *International Conference on Medical Image Computing and Computer-Assisted Intervention*, pages 497–504. Springer, 2015.

[123] BK Medical Holding Company Inc. Bk medical ultrasound for robotic-assisted surgery. https://www.bkmedical.com/applications/clear-real-time-visual-ultrasound-guidance-for-confident-robotic-assisted-procedures/. Accessed: March 2021.

[124] Carol M Rumack and Deborah Levine. *Diagnostic ultrasound E-book*. Elsevier Health Sciences, 2017.

[125] Roger Y Tsai and Reimar K Lenz. A new technique for fully autonomous and efficient 3d robotics hand/eye calibration. *IEEE Transactions on robotics and automation*, 5(3):345–358, 1989.

[126] Larry L Schumaker. *Spline functions: computational methods*. SIAM, 2015.

[127] Alexander Kutikov and Robert G Uzzo. The renal nephrometry score: a comprehensive standardized system for quantitating renal tumor size, location and depth. *The Journal of urology*, 182(3):844–853, 2009.